bioRxiv preprint doi: https://doi.org/10.1101/508549; this version posted December 30, 2018. The copyright holder for this preprint (which was not certified by peer review) is the author/funder. All rights reserved. No reuse allowed without permission.

**Title:**

# Proteasome inhibitor-induced modulation reveals the spliceosome as a specific therapeutic vulnerability in multiple myeloma

**Authors:**

Hector H. Huang[1], Ian D. Ferguson[1], Alexis M. Thornton[2], Christine Lam[1], Yu-Hsiu T. Lin[1], Prabhakar Bastola[1], Margarette C. Mariano[1], Makeba Marcoulis[1], Julia Malato[3], Paul Phojanakong[3], Byron C. Hann[3], Angela N. Brooks[2], Arun P. Wiita[1,3,*]

**Affiliations:**

[1]Dept. of Laboratory Medicine, University of California, San Francisco, CA [2]Dept. of Biomolecular Engineering, University of California, Santa Cruz, CA, [3]Helen Diller Family Comprehensive Cancer Center, University of California, San Francisco, CA

***Lead contact, to whom correspondence should be addressed:**

Arun P. Wiita, MD, PhD

Arun.wiita@ucsf.edu

UCSF Dept. of Laboratory Medicine

185 Berry St., Ste. 290

San Francisco, CA 94107

bioRxiv preprint doi: https://doi.org/10.1101/508549; this version posted December 30, 2018. The copyright holder for this preprint (which was not certified by peer review) is the author/funder. All rights reserved. No reuse allowed without permission.

**Summary:**

Resistance to proteasome inhibitors (PIs) is a ubiquitous clinical concern in multiple myeloma. We proposed that signaling-level responses after PI would reveal new means to enhance efficacy. Unbiased phosphoproteomics after the PI carfilzomib surprisingly demonstrated the most prominent phosphorylation changes on spliceosome components. Spliceosome modulation was invisible to RNA or protein abundance alone. Transcriptome analysis demonstrated broad-scale intron retention suggestive of PI-specific splicing interference. Direct spliceosome inhibition synergized with carfilzomib and showed potent anti-myeloma activity. Functional genomics and exome sequencing further supported the spliceosome as a specific vulnerability in myeloma. Our results propose splicing interference as an unrecognized modality of PI mechanism, reveal additional modes of spliceosome modulation, and suggest spliceosome targeting as a promising therapeutic strategy in myeloma.

**Significance:**

PIs are a first-line therapy in multiple myeloma but are not curative. Discovering new modes of PI action may suggest new ways to overcome resistance, a major clinical challenge, or define rational combination therapies. Here we combine phosphoproteomics and transcriptional analysis to discover that PIs specifically interfere with normal splicing. We further use pharmacologic and genetic data to suggest that myeloma plasma cells are selectively vulnerable to direct inhibition of the spliceosome, which has recently become a promising therapeutic strategy in other hematologic malignancies. Our results reveal a new approach to enhance the efficacy of a ubiquitous first-line myeloma treatment as well as uncover broader roles of splicing modulation during cancer therapy.

**Keywords:**

Mass Spectrometry, Proteomics, Splicing, Alternative Splicing, Phosphoproteomics, Myeloma, Spliceosome, SF3B1, SRSF1

bioRxiv preprint doi: https://doi.org/10.1101/508549; this version posted December 30, 2018. The copyright holder for this preprint (which was not certified by peer review) is the author/funder. All rights reserved. No reuse allowed without permission.

## INTRODUCTION

Multiple myeloma is a clonal malignancy of plasma cells with no known cure. Like normal plasma cells, myeloma plasma cells produce and secrete incredible amounts of immunoglobulin. In the clinic, this unique biological function may be exploited by therapeutically inhibiting the proteasome using the FDA-approved proteasome inhibitors (PIs) bortezomib, carfilzomib, and ixazomib. Proteotoxic stress caused by these first-line therapeutic agents has been proposed to induce the apoptotic function of the unfolded protein response (UPR) (Walter and Ron, 2011), leading to plasma cell death while largely sparing normal tissues (Lee et al., 2003; Obeng et al., 2006). However, despite the appealing simplicity of this mechanism, the canonical UPR is not always strongly induced in myeloma cells by PIs (Le Moigne et al., 2017) and is unlikely to be the sole mode of PI cytotoxicity in MM. Indeed, many additional mechanisms of action of PIs have also been proposed, ranging from NF-kB inhibition to immune microenvironment effects to aberrant recycling of cytosolic amino acids (Gandolfi et al., 2017; Suraweera et al., 2012).

Identifying the full range of PI mechanisms of action remains relevant given that acquired PI resistance is clinically widespread but its origins remain unclear (Wallington-Beddoe et al., 2018; Mitra et al., 2017). Identifying new methods by which to specifically target PI-resistant disease, or molecules to synergize with PIs to avoid resistance by driving deeper remissions, remains a long-standing goal. As one approach to achieving this goal, we and others have studied the response of malignant plasma cells to PIs using both gene expression and proteomic methods (Liu et al., 2017; Mitsiades et al., 2002; Wiita et al., 2013). Notably, one of the most prominent features of the cellular response to PIs is the activation of the heat shock response (Shah et al., 2015). This mechanism leads to significant induction of cytosolic protein-folding chaperones, possibly to assist in protein refolding and decrease in unfolded protein stress. We and others (Li et al., 2015; Shah et al., 2015; Wiita et al., 2013) have therefore proposed targeting mediators of the heat shock response as potential combination therapies with PIs.

However, one unresolved question is whether proteasome inhibition may carry additional effects on plasma cells that are not revealed by mRNA or protein abundance analysis alone. We hypothesized that additional modalities of response, and thereby new myeloma-relevant therapeutic targets, may be revealed by studying the signaling-level response to PIs with unbiased mass spectrometry-based phosphoproteomics. The large majority of therapy-relevant investigations using this technique have focused on elucidating the effects of kinase inhibitors (Casado et al., 2017). However, we reasoned that a significant cellular perturbation such as proteasome inhibition would likely also indirectly perturb kinase and phosphatase signaling in a broad fashion.

bioRxiv preprint doi: https://doi.org/10.1101/508549; this version posted December 30, 2018. The copyright holder for this preprint (which was not certified by peer review) is the author/funder. All rights reserved. No reuse allowed without permission.

Here, we used unbiased phosphoproteomics to quantify >5000 phosphopeptides in myeloma cells exposed to the irreversible PI carfilzomib (Cfz). Surprisingly, we found the greatest increases in phosphorylation in proteins associated with the spliceosome machinery. A link between these processes was invisible at the level of gene expression alone. We further evaluated this link from a mechanistic and therapeutic perspective, finding that PIs lead to specific disruption of normal splicing. We suggest abrogation of splicing as an additional mechanism of action of PIs not previously explored. Inhibition of splicing has recently become a promising therapeutic strategy in other hematologic malignancies (Lee and Abdel-Wahab, 2016). Our results reveal an intersection of cellular stress and the splicing machinery, which may have broad relevance in splicing biology. Furthermore, we propose the spliceosome as a new and potentially selective therapeutic target in myeloma.

## RESULTS

### Proteasome inhibition results in sustained phosphorylation of splicing factors in myeloma plasma cells

We first used unbiased phosphoproteomics to examine the signaling-level response of MM.1S multiple myeloma cells to Cfz. We chose time points for analysis based on our prior results, demonstrating that the transcriptional and proteomic response to proteasome inhibition evolves over many hours (Wiita et al., 2013). This timeframe is in contrast with the vast majority of prior perturbation phosphoproteomic studies, which have typically directly examined effects on kinase activation or inhibition on a timescale of minutes (Casado et al., 2017). Here, we instead anticipate all effects on phosphorylation to be indirect. Indeed, using label-free quantification of immobilized metal affinity chromatography (IMAC)-isolated phosphopeptides, we found that altered phosphorylation signatures were most prominent 24 hours after treatment (**Fig. 1 and Fig. S1**). In total, we quantified 5791 phosphosites in at least one technical replicate of the time course, with >98% of phosphosites representing Ser or Thr phosphorylation events, as expected using this enrichment technique (**Supplemental Dataset 1**). Notably, by 24h after 30 nM Cfz, cell viability was approximately 30% of baseline, indicating significant drug-induced cytotoxicity by this final time point.

For comparison to our phosphoproteomic results, at each time point we simultaneously performed single-end RNA-seq for gene expression using rRNA-depleted total RNA. **Fig. 1B** shows 58 upregulated (red) and 75 downregulated (blue) phosphopeptides from proteins with largely unchanged RNA transcript abundance as detected by unsupervised hierarchical clustering. Upon this initial analysis, we were encouraged to find decreased phosphorylation of the translation factor EIF4E-BP1 as well as the ribosomal subunit RPS6 (**Fig. 1B**). These phosphorylation-level responses related to suppressed translation are expected upon PI-

bioRxiv preprint doi: https://doi.org/10.1101/508549; this version posted December 30, 2018. The copyright holder for this preprint (which was not certified by peer review) is the author/funder. All rights reserved. No reuse allowed without permission.

induced cellular stress (Wiita et al., 2013). While other downregulated phosphopeptides did not suggest a specific highly-enriched biological function, upon manual inspection of upregulated phosphosites we were surprised to find that 14 of 58 were present on proteins related to pre-mRNA splicing. These primarily included phosphopeptides deriving from the heterogeneous ribonucleoprotein (HNRNP) family of proteins as well as phosphopeptides belonging to the SRSF family of splicing factors (**Fig. 1B**). In particular, the arginine- and serine-rich "RS" domain of the SRSF proteins are known to have their splicing activity modulated by phosphorylation (Long and Caceres, 2009). Notably, these prominent signaling-level effects on splicing factors were invisible to prior gene expression studies of PI response and have not been investigated previously. We therefore chose to further explore the interaction between PIs and the splicing machinery.

To validate this initial result from label free quantitative proteomics, we prepared independent samples using a stable isotope labeling (SILAC) phosphoproteomics approach. Based on our results above, for SILAC we examined only the 24 hr time point in MM.1S cells. In biological replicate for each dose, we evaluated both a low dose (10 nM) and a moderate dose (18 nM) of Cfz (**Fig. 2A-B**). With this lot of Cfz, 10 nM drug elicited ~20% cell death after 24 h, while 18 nM killed ~85% of cells (**Fig. S3A**). Of the 520 phosphosites significantly ($p < 0.05$; > 2-fold-change) upregulated in MM.1S treated with 18 nM Cfz in **Fig. 2A**, 127 (24.4%) are associated with splicing-related proteins, with 23 of these as part of the SRSF protein family of splicing factors. Background-corrected Gene Ontology (GO) analysis (see Methods) confirms that all of the top enriched biological processes involve RNA splicing regulation and mRNA processing (**Fig. S1B, 2D**). At 10 nM Cfz, though, this signaling response is much weaker with only 60 upregulated phosphopeptides; none of these are splicing-related. These results suggest that there is a strong dose-response effect of phosphorylation changes after proteasome inhibition, both across splicing factors and the broader proteome.

To compare these changes at the signaling level to changes at the protein level, unenriched peptides were also analyzed by LC-MS/MS (**Fig. S2A-B**). Confirming expected responses to proteasome inhibition, the most upregulated proteins included heat shock-induced chaperones as well as *SQSTM1*/p62 associated with autophagy (Wiita et al., 2013). In contrast, splicing factors with increased phosphorylation sites do not significantly change in abundance, confirming that phosphosite increases are due to changes at the signaling level and not protein copy number.

**Melphalan induces a similar but not identical phosphorylation response**

We next investigated whether this broad splicing factor phosphorylation phenotype was unique to proteasome inhibition or was also seen under a different drug mechanism of action. We chose to compare the response of MM.1S cells to melphalan, a DNA alkylating agent and

bioRxiv preprint doi: https://doi.org/10.1101/508549; this version posted December 30, 2018. The copyright holder for this preprint (which was not certified by peer review) is the author/funder. All rights reserved. No reuse allowed without permission.

clinically-used myeloma therapeutic. In parallel, we also treated another MM cell line, AMO-1, with Cfz to determine if the phosphorylation response to proteasome inhibitor is consistent across cell line models.

For these experiments we again used a single-time point SILAC approach. Here, both 10 μM melphalan and 15 nM Cfz led to ~20% cell death in MM.1S and AMO-1, respectively, at 24 hr (**Fig. S3A**). Western blot confirmed induction of DNA damage by melphalan and proteotoxic stress response for Cfz (**Fig. S3C-D**). Compared to 18 nM Cfz, we saw largely decreased phosphorylation-level responses to both of these agents (**Fig. 2C**). Of 113 phosphosites significantly upregulated in AMO-1, 7 belong to splicing related proteins (SRSF2, SRSF6, SRRM1, HNRNPH1, TRA2A, DDX1). This result is consistent with the results of **Fig. 2A-B**, where greater cytotoxicity correlates with more prominent phosphorylation effects.

Under 10 μM melphalan, 93 phosphosites were significantly upregulated, with 8 sites on splicing related proteins (HNRNPK, TRA2A, SRRM2, and WDR77), although none are SRSF family members (**Fig. 2D**). Furthermore, as expected, both unenriched shotgun proteomics and RNA-seq for gene expression confirms differential biological responses in response to proteasome inhibition and DNA damage (**Fig. S2A,D,E**). Again, no splicing factors with altered phosphosites under either drug treatment were changed at the protein abundance level.

We further performed Kinase Set Enrichment Analysis (KSEA) (Casado et al., 2013) on our MM.1S datasets to identify kinases whose activity may regulate differential phosphorylation found by phosphoproteomics. While this tool is limited by a reliance on well-characterized kinase-substrate relationships, and despite the different number of phosphosites upregulated under each condition, within this framework this tool identified similar kinases active under both 18 nM Cfz and 10 μM melphalan treatment (**Fig. 2F**). Notably, both drugs are predicted to induce activity of cdc2-like kinase 1 (CLK1), a kinase known to phosphorylate SRSF family splicing factors among other proteins (Colwill et al., 1996). However, in line with the specific biology of PIs, Cfz also strongly induced inhibitory kappa B kinase (IKBKB) activity, a kinase leading to NF-kB inhibition after PI treatment (Traenckner et al., 1994). Taken together, these results indicate that drug-induced stress may broadly lead to phosphorylation of splicing factors, though precise patterns of phosphorylation may differ in a drug-specific manner.

**Proteasome inhibition induces intron retention in MM cells**

Given our results demonstrating that PI treatment can lead to splicing factor phosphorylation, a clear next question was to ask whether pre-mRNA splicing itself was altered after drug treatment. We therefore obtained paired-end sequencing data from polyA-enriched RNA on the same samples used for phosophoproteomics and one additional biological replicate ($n$ = 3 total) of each of the following: MM.1S treated with 18 nM Cfz, MM.1S treated with 10 μM melphalan, MM.1S treated with DMSO as control, AMO-1 treated with 15 nM Cfz, AMO-1

bioRxiv preprint doi: https://doi.org/10.1101/508549; this version posted December 30, 2018. The copyright holder for this preprint (which was not certified by peer review) is the author/funder. All rights reserved. No reuse allowed without permission.

treated with DMSO as control. We used JuncBASE (Brooks et al., 2011) to process the aligned sequencing data by identifying and quantifying both annotated and novel splice junctions. Data for each alternative splicing event was evaluated using the standard measure of "percent spliced in" or PSI ($\psi$) (**Fig. 3A**).

Examination of the differential PSI ($\Delta$PSI) between 18 nM Cfz- and DMSO-treated MM.1S demonstrated a broad distribution of alternative splicing events in categories such as alternative exon acceptor, alternative last exon, alternative first exon, and intron retention (IR) (**Fig. 3B**). However, of the splicing differences assessed by JuncBASE, the $\Delta$PSI distribution for IR demonstrated the clearest positive shift after Cfz treatment ($n$ = 25,807 total IR events measured; median = 2.54), whereas $\Delta$PSI for other categories were closer to a median of zero ($p$ < 2.2E-16 for median of IR distribution vs. median of alternative exon acceptor by Mann-Whitney test). This finding particularly intrigued us as PIs are well known to induce a strong heat shock response (Shah et al., 2015). Prior work in murine 3T3 fibroblasts demonstrated that heat shock alone showed similar global effects on inducing IR without broadly affecting other alternative splicing events (Shalgi et al., 2014). Our results suggest that a similar phenomenon may be present in MM cells exposed to PI.

From a mechanistic perspective, we also considered the possibility that the IR phenotype results from a global dysfunction of the splicing machinery during drug-induced apoptosis. Our prior proteomic data indicated that SF3B1 and U2AF1, core components of the splicing machinery, are some of the earliest substrates cleaved by caspases during PI-induced apoptosis (Wiita et al., 2013). Indeed, by Western blotting we validated that SF3B1 and U2AF1 are proteolytically cleaved after Cfz treatment and this cleavage can be blocked by the pan-caspase inhibitor zVAD-fmk (**Fig. S3E**).

However, arguing against caspase cleavage of splicing factors as the sole cause of IR, we found a similar, but not identical global shift in IR distribution in AMO-1 cells treated with 15 nM Cfz ($n$ = 27,386; median = 2.2) (**Fig. 3C**) despite much less cytoxicity than the 18 nM Cfz treatment in MM.1S (~20% vs. ~85% cytotoxicity, respectively). Furthermore, a much smaller shift in IR was noted after 10 μM melphalan treatment at ~20% cytotoxicity ($n$ = 24,247; median = 0.44; $p$ < 2.2E-16 for IR distribution MM.1S 18 nM Cfz vs 10 μM melphalan). These findings illustrate a more pronounced IR phenotype after PI than DNA damage, even at the same relatively low degree of drug-induced cell death.

**SRSF splicing factors appear highly phosphorylated at baseline in MM cells**

To investigate our phosphoproteomic results via an orthogonal method, we performed Western blots to evaluate for phosphorylation-induced gel shift after Cfz treatment of SRSF1, SRSF3, and SRSF6. After Cfz treatment we saw no discernable gel shift of these proteins (**Fig. S3F**). However, even in our DMSO control we noted that both proteins ran at molecular weights

bioRxiv preprint doi: https://doi.org/10.1101/508549; this version posted December 30, 2018. The copyright holder for this preprint (which was not certified by peer review) is the author/funder. All rights reserved. No reuse allowed without permission.

significantly above that predicted from primary sequence. After treatment of lysate with calf alkaline phosphatase we noted a substantial shift to the predicted molecular weight (**Fig. S3F**). Therefore, these SRSF factors exist in a highly phosphorylated state even at baseline in MM plasma cells. Upregulated phosphorylation post-Cfz identified by mass spectrometry may therefore represent additional phosphorylation at only selected phosphosites. While these changes in phosphorylation may still result in biological effects, Cfz-induced modulation does not appear to reflect a dramatic shift in the overall phosphorylation status of these SRSF proteins in this system.

To further investigate baseline phosphorylation status of SRSF proteins, we treated MM.1S cells with 50 μM KH-CB19 (Fedorov et al., 2011), a reported highly selective inhibitor of the SRSF kinases CLK1 and CLK4 ($K_D$ = 20 nM vs. CLK1). We did not observe any viability effects in MM.1S even at this high concentration (**Fig. S3A**). Unbiased phosphoproteomics after 24 hr of KH-CB19 treatment surprisingly showed no significant change in phosphorylation status of any quantified SRSF phosphosites (**Fig. S2F**). These results suggest that other kinases also play a role in maintaining SRSF phosphorylation in this system, either at baseline or via feedback mechanisms after sustained CLK1 inhibition.

**Exogenous expression of SRSF1 wildtype and RS-domain mutants do not significantly alter splicing patterns**

Thus far we have found that proteasome inhibition can lead to both robust splicing factor phosphorylation as well as widespread IR of pre-mRNA. A major question raised by these results is whether these two processes are causally linked or whether they instead occur via parallel mechanisms. To initially investigate this question, we considered SRSF1 (also known as SF2 or ASF), a well-characterized member of the SR family of splicing factors and a putative proto-oncogene (Karni et al., 2007; Long and Caceres, 2009). All members of this family contain RNA recognition motifs (RRM) and arginine- and serine-rich domains (RS) (Long and Caceres, 2009). In most cases, SR proteins recognize *cis*-acting splice enhancers on pre-mRNA and work to promote splicing by initially recruiting the spliceosome to these intron-exon junctions (Long and Caceres, 2009). We found that SRSF1 demonstrates upregulated phosphorylation at sites in both the RS1 and RS2 domain when MM cells are treated with Cfz (**Fig. 2A**). The current model of SRSF1 function suggests that SR-protein kinases (SRPK)-mediated phosphorylation of RS domains leads to translocation into the nucleus, further hyperphosphorylation by CLK1 causes association with the U1 spliceosome, and partial dephosphorylation is required for splicing catalysis (Ghosh and Adams, 2011; Long and Caceres, 2009; Misteli et al., 1998).

To study the effects of SRSF1 phosphorylation in MM, we exogenously expressed a wildtype (SRSF1 WT), phosphomimetic (SRSF1mSD), or phosphodead (SRSF1mSA) variant in

bioRxiv preprint doi: https://doi.org/10.1101/508549; this version posted December 30, 2018. The copyright holder for this preprint (which was not certified by peer review) is the author/funder. All rights reserved. No reuse allowed without permission.

AMO-1 plasma cells. We assumed an all-or-none model of SR protein phosphorylation, where exogenous SRSF1 mutants have all 20 serines in the RS1 and RS2 domains replaced with either an aspartate (SD) or an alanine (SA). Exogenously expressed SRSF1 proteins are tagged with a C-terminal mCherry, nuclear localization signal (NLS) and 3x FLAG-peptide (**Fig. 4A**). It is known that phosphorylation of the RS1 domain is necessary for nuclear localization (Caceres et al., 1998; Misteli et al., 1997); the attempted forced nuclear localization of the SA mutant was chosen to probe potential splicing-level effects of phospho-dead SRSF1 interacting with the spliceosome. Immunoblot of exogenous SRSF1 constructs in **Fig. S4C**, which migrates higher than endogenous SRSF1 and can be compared directly, demonstrates lower expression than the high-abundance endogenous protein. Epi-fluorescent images in **Fig. 4B** show the distribution of exogenous SRSF1 WT, SD, and SA mutants. Notably, most of WT and SD signal is localized to the nucleus, suggestive of functional protein product and consistent with expected biology. However, a much larger fraction of SA mutant is trapped in the cytosol despite NLS tagging. Consistent with prior work (Aubol et al., 2018; Caceres et al., 1997), this finding suggests that phosphorylation of RS domains is a major requirement for entry into the nucleus.

Upon JuncBASE analysis of poly-A RNA-seq data from DMSO-treated WT, SD, and SA construct ($n$ = 3 for each), we saw remarkably few global ΔPSI differences as a function of modeled SRSF1 phosphorylation status (**Fig. 4D**). This lack of change is not entirely unexpected, as despite evidence for SRSF1 phosphorylation status playing a critical role in splicing catalysis for individual model transcripts *in vitro* (Cao et al., 1997; Prasad et al., 1999), global splicing changes as a function of SR protein phosphorylation have not been definitively shown. In addition, our results in **Fig. 1B** suggested that phosphorylation of multiple SRSF proteins occurs simultaneously under Cfz-induced stress; altered phosphorylation of SRSF1 alone may not carry any significant effects.

**SRSF1 RS-domain phosphomimetic mutant demonstrates weakened interaction with the spliceosome**

Though we cannot draw a direct link between SRSF1 phosphorylation status and specific alternative splicing events, we further investigated the diverse biological roles of SRSF1. In addition to modulating pre-mRNA splicing, these include regulating nuclear export of spliced mRNAs and translational regulation in the cytosol via interaction with the ribosome (Das et al., 2007; Huang et al., 2003; Xiao and Manley, 1997). Using the 3x-FLAG tag on constructs we performed affinity purification mass spectrometry (AP-MS) with label-free quantitative proteomics vs. an mCherry-NLS-$[FLAG]_3$ control (**see methods**). We specifically evaluated differential binding partners of SRSF1 as a function of phosphorylation status across both the nuclear and cytoplasmic compartments.

bioRxiv preprint doi: https://doi.org/10.1101/508549; this version posted December 30, 2018. The copyright holder for this preprint (which was not certified by peer review) is the author/funder. All rights reserved. No reuse allowed without permission.

While clear differences were observed between the nuclear and cytosolic interactome for each construct, overall biological signatures based on GO analysis were surprisingly similar across WT, SD, and SA within each compartment (**Fig. S5B, D, F**). Notably, in the cytosol we found consistent interactions between both SRSF1 WT and SRSF1mSD with several RNA-binding proteins as well as components of the translational machinery. We do note one stark difference based on phosphorylation status in the nuclear fraction, where the WT construct showed direct evidence of interaction with several small nuclear ribonucleoprotein polypeptides, core components of the U1-U2 spliceosome (**Fig. 4E**). Unexpectedly, these nuclear interactions were not enriched in the SD construct, which instead interacted with other splicing-related factors such as TRA2a, TRA2b, and PABPC (**Fig. 4F**). This interactome mapping may help refine the current model of SRSF1 biology, which suggests that hyperphosphorylation of RS domains leads to preferential integration with the U1 spliceosome (Cho et al., 2011; Ngo et al., 2005).

**Proteasome inhibition of MM cells results in both stochastic intron retention and specific alternative exon usage**

We next explored the splicing-level effects of 15 nM Cfz treatment on AMO-1 cells expressing the WT, SD, and SA constructs. Notably, in this setting cytotoxicity at 24 hr was <10% in 8 of 9 total replicates (**Fig. S4B**). Compared to DMSO-treated samples (**Fig. 4C**), Cfz again elicited a response consistent with that found in **Fig. 3C**: despite minimal cell death, we observed a clear shift in the median ΔPSI toward increased global IR (n=12,139; median = 2.45, $p$ < 2.2E-16 for one-sample Wilcoxon summed rank test). These findings in the absence of apoptosis underscore that caspase cleavage of splicing factors is unlikely to be a primary mechanism of intron retention after proteasome inhibition.

These additional SRSF1 constructs allowed us to perform JuncBASE analysis on a combined dataset of all Cfz-treated samples vs. DMSO ($n$ = 24 replicates total across all AMO-1 (data in **Fig. 3C, 4C**)). With this increased statistical power, we were able to identify *CNNM3*, which encodes a divalent metal cation transporter, as showing among the strongest signatures of IR across all events (FDR-corrected $p$-value = 0.032) (**Fig. S4E**). However, despite the consistent, global shift of median IR to higher values, as well as the overall large number of IR events detected by JuncBASE (**Fig. 5B, left**), very few individual transcripts ($n$ = 43, including *CNNM3*) showed statistically significant (FDR-corrected $p$-value < 0.05) IR across samples (**Fig. 5B, right**). This finding suggests that Cfz-induced IR may be a stochastic process, perhaps resulting from general interference with the splicing machinery but without a strong selection for specific transcripts.

In contrast, we saw statistically significant changes across two other types of alternative splicing events: alternative exon donor ($n$ = 1134) and alternative exon acceptor ($n$ = 810)

bioRxiv preprint doi: https://doi.org/10.1101/508549; this version posted December 30, 2018. The copyright holder for this preprint (which was not certified by peer review) is the author/funder. All rights reserved. No reuse allowed without permission.

usage. These differential effects were found despite no pronounced global shift in the ΔPSI median for these categories and a lesser number of total events detected by JuncBASE (**Fig. 5B**). We investigated whether these consistently observed alternative splicing events may carry some biological relevance. Interestingly, GO enrichment analysis of all the genes undergoing significant alternative splicing after Cfz (n = 2,575 events total across all categories in **Fig. 5B, right**) revealed 'proteasome-mediated ubiquitin-dependent protein catabolic process' (*p* = 2.08E-16) and 'protein polyubiquitination' (*p* = 1.39E-13) as highly enriched (**Fig. 5C**). Notably, multiple proteasome subunits (*PSMA3/5/7, PSMB4/5, PSMC1/4/5, PSMD1-4, PSME2*), the protein homeostasis node p97 (*VCP*), and ubiquitin (*UBB, UBC*) itself are included within these genes demonstrating some degree of alternative splicing after Cfz (example in **Fig. 5D**). While these effects are modest (ΔPSI ~10-15%), they raise the possibility that alternative splicing may modulate the protein homeostasis machinery in response to therapeutic proteasome inhibition.

Taken together, our results offer a model for the effects of proteasome inhibition on the splicing machinery in myeloma (**Fig. 5E**). Upon therapeutic insult, the stress response induces phosphorylation of multiple splicing factors. Though the effect of this phosphorylation on specific splicing events remains unclear, these events may relate to specific alterations in exon usage based on known SRSF biochemistry. In parallel, we observe a broad increase in the number of stochastically distributed IR events. These IR events, expected to reduce the number of functional protein products, may broadly reduce proteotoxic stress and conserve cellular resources normally devoted to protein synthesis, thereby playing a role in adaptation to proteasome inhibition. Alternatively, the intron retention phenotype may indicate malfunction of the spliceosome, an essential process whose loss reduces tumor cell fitness. Interference with splicing may therefore be a previously unappreciated part of the PI mechanism of action. Finally, our analysis of specific exon usage suggests that modification of the proteasome itself via alternative splicing may play a role in adaptation or resistance to proteasome inhibitor.

**The spliceosome inhibitor E7107 is broadly potent versus MM cells and synergistic with proteasome inhibitor**

Extending from this potential new mechanism of action of PIs as interfering with splicing, we further investigated the therapeutic potential of more dramatic spliceosome disruption in myeloma. For our preclinical studies we employed the tool compound E7107, a pladienolide B analog and direct inhibitor of the core U2 catalytic spliceosome component SF3B1 (Lee and Abdel-Wahab, 2016). This molecule has recently been described to induce extreme IR and strong cytotoxic effects versus models of myeloid malignancy, particularly those carrying mutations within splicing factors (Lee et al., 2016).

Using both qPCR validation of canonical IR events after SF3B1 inhibition (Seiler et al., 2018b) (**Fig. S6B**) as well as JuncBASE analysis of RNA-seq data (**Fig. 6A**), as expected we

bioRxiv preprint doi: https://doi.org/10.1101/508549; this version posted December 30, 2018. The copyright holder for this preprint (which was not certified by peer review) is the author/funder. All rights reserved. No reuse allowed without permission.

identified very significant IR after 6h of 10 nM E7107 treatment in MM.1S cells. There was no noted cytotoxicity at this early time point (**Fig. S6A**). However, underscoring the potential of splicing inhibition as a therapeutic strategy in MM, E7107 was extremely potent versus a panel of seven MM cell lines treated for 48 hr, with $LC_{50}$'s ranging from <1 nM to 30 nM (**Fig. 6B**). In addition, a PI-resistant AMO-1 cell line (Soriano et al., 2016) showed very similar sensitivity to E7107 as the parental line (**Fig. 6C**). This finding suggests the potential for clinical utility of splicing inhibition even in PI-refractory disease.

We noted that our MM cell line sensitivities appeared essentially bimodal, with one group of more sensitive lines with $LC_{50}$'s of <1 nM and another slightly less sensitive group of cell lines with $LC_{50}$ of 20-50 nM. In an attempt to identify potential determinants of this differential drug sensitivity, we examined publicly available RNA-seq data of baseline gene expression in MM cell lines (www.keatslab.org). We were intrigued to find that the more sensitive lines demonstrated significantly higher RNA expression of SF3B1 (**Fig. 6D**). This outcome hinted that more sensitive cell lines may somehow be more "addicted" to SF3B1, leaving them more vulnerable to splicing inhibition, as well as revealing a potential biomarker that could be used for patient stratification. Unfortunately, however, this result was not confirmed at the protein level (**Fig. 6D**), suggesting that SF3B1 may undergo post-transcriptional regulation. We were unable to identify any other candidates for markers of sensitivity or resistance to E7107 based on available DNA or RNA sequencing data from this limited cohort of cell lines.

We further explored the hypothesis that interfering with splicing via two different mechanisms may lead to synergistic MM cell death. Indeed, combination studies with Cfz and E7107 showed strong synergy across the dosing landscape based on ZIP synergy scoring (Yadav et al., 2015) (**Fig. 6E-F**). In contrast, melphalan, which induced much less IR than PI (**Fig. 3B-C**), showed much weaker synergy in combination with E7107 (**Fig. 6G-H**). These findings support the approach of using splicing inhibitors in combination with PIs in MM treatment. Also, this result supports the hypothesis that splicing inhibition is a part of the PI mechanism of action.

**E7107 is a highly potent versus myeloma both *in vivo* and *ex vivo***

Based on this encouraging *in vitro* data, we then moved into a standard *in vivo* MM model of luciferase-labeled MM.1S cells implanted intravenously into NOD *scid* gamma (NSG) immunocompromised mice. These cells home to the murine bone marrow, partially recapitulating the tumor microenvironment in human disease (McMillin et al., 2013). We found that E7107 was generally well-tolerated with no appreciable weight loss (**Fig. S7A**). At 3 mg/kg E7107 I.V., a relatively low dose compared to prior studies in other malignancies (Lee et al., 2016), we still found pronounced anti-MM effect after a brief 2 week treatment (**Fig. 7A-C**). This

bioRxiv preprint doi: https://doi.org/10.1101/508549; this version posted December 30, 2018. The copyright holder for this preprint (which was not certified by peer review) is the author/funder. All rights reserved. No reuse allowed without permission.

suppression of tumor translated into a significant survival benefit ($p$ = 0.01, Log-Rank test; $n$ = 6 per arm).

We next turned to *ex vivo* evaluation versus primary patient samples. Fresh bone marrow mononuclear cells from five PI-refractory MM patients were treated for 48 hr with varying doses of E7107. Based on flow cytometry analysis of CD138+ plasma cells (**Fig. S7B**), we found similar high sensitivity of patient tumor cells to E7107 as found in cell lines, with estimated $LC_{50}$'s in the low-nM range (**Fig. 7D**). Notably, non-plasma cell bone marrow mononuclear cells (CD138- fraction) showed remarkably little cytotoxicity at these same doses, supporting a potential therapeutic index for splicing inhibitors in MM.

**Functional genomics and whole exome sequencing suggests clinical applications of splicing inhibition in MM**

E7107 is no longer in active clinical development due to aberrant visual toxicity in patients (Lee and Abdel-Wahab, 2016). However, in a phase I clinical trial in advanced solid tumors, nM levels in blood were otherwise well-tolerated (Hong et al., 2014). Given our data showing low-nM cytotoxicity of E7107 in this hematologic malignancy, this clinical data also supports a potential therapeutic index of similarly potent splicing inhibitors in myeloma.

Notably, analysis of CRISPR essentiality screen data in the Cancer Dependency Map (www.depmap.org; Avana library public 18Q4 (Tsherniak et al., 2017)), across over 400 cancer cell lines, demonstrates that myeloma has among the strongest genetic dependencies on *SF3B1* (**Fig. S7C**). This genetic ablation data further supports the ability to pharmacologically eliminate MM tumor cells via splicing inhibition while sparing normal cells. We further extended this analysis to other core components of the U1- U2 spliceosome (Wahl et al., 2009) found to be "common essential" genes per DepMap CRISPR functional genomic screening. We found that MM cell lines are, on aggregate, the most sensitive tumor cell type to genetic ablation of these central protein components of snRNP association with pre-mRNA and splicing catalysis (**Fig. 7E**). As a comparator, based on DepMap analysis we note even more favorable genetic evidence for targeting the spliceosome in MM than even the essential subunits of the 20S proteasome (including the direct PI target *PSMB5*) (**Fig. S7D**).

Furthermore, a recent study validated the sulfonimide indisulam as an inhibitor of splicing via targeted degradation of RBM39, another component of the spliceosome with high homology to U2AF2 (Han et al., 2017). In this work, hematopoeitic malignancy cell lines were broadly more sensitive to indisulam than solid tumor cell lines. We confirmed cytotoxicity of indisulam versus a panel of MM cell lines (**Fig. S7E**), though $LC_{50}$'s (0.3->20 μM) were much higher than those for the SF3B1 inhibitor E7107. In DepMap data, MM was again among the more sensitive tumor types to RBM39 ablation (**Fig. S7F**). Indisulam may therefore represent

bioRxiv preprint doi: https://doi.org/10.1101/508549; this version posted December 30, 2018. The copyright holder for this preprint (which was not certified by peer review) is the author/funder. All rights reserved. No reuse allowed without permission.

another approach to targeting the spliceosome in this disease, though given lower potency the potential for clinical translation is less clear.

We next took advantage of genomic and transcriptomic data from isolated malignant plasma cells from newly-diagnosed MM patients in the Multiple Myeloma Research Foundation CoMMpass study (research.themmrf.org; version IA11). First evaluating gene expression data, we intriguingly found significantly decreased progression-free survival among patients in the top quartile of *SRSF1* expression versus those in the bottom quartile ($p$ = 0.0081 by Log-Rank test) and a trend toward similarly decreased overall survival for patients in the top vs. bottom quartile of *SF3B1* expression ($p$ = 0.087) (**Fig. S7G**). These results raise the possibility of poorer outcomes in patients whose disease is more dependent on the spliceosome.

However, we note that both E7107 (Lee et al., 2016) and the recently described splicing inhibitor H3B-8800 (Seiler et al., 2018b) have both been shown to have the greatest potency versus hematopoietic malignancies carrying mutations in splicing factors such as *SF3B1*, *SRSF2*, *U2AF2*, and *ZRSR2* (Saez et al., 2017). These mutations are seen frequently in myelodysplastic syndromes (MDS), acute myeloid leukemia, and chronic lymphocytic leukemia, appearing in up to 50% of MDS patients (Saez et al., 2017). We therefore examined exome sequencing data available in CoMMpass and found that 28.0% of MM patients (268 of 956) were found to carry missense mutations within at least one of 119 splicing-associated factors recently proposed to be most relevant to tumorigenesis across a survey of the The Cancer Genome Atlas (**Fig. 7F, Supplemental Dataset 3**) (Seiler et al., 2018a). While only a small minority of these identified mutations have been functionally validated to affect splicing, the most common single mutation was at the known "hotspot" *SF3B1* K666T, found in three patients. Variant allele frequencies for these expected heterozygous mutations were 42%, 35%, and 22%, suggestive of a prominent subclonal fraction of the tumor cell population. Among well-characterized genes, mutations were found in *SF3B1* ($n$ = 10 patients total including noted K666T mutations), *SRSF2* ($n$ = 2), *U2AF1* ($n$ = 4), and *ZRSR2* ($n$ = 1). Unfortunately we were unable to obtain rare primary patient samples containing mutations in these genes, and no myeloma cell lines are known to carry hotspot mutations in these well-characterized splicing factors (www.keatslab.org). While our data suggest that spliceosome inhibition should be considered a therapeutic option for MM patients of any genotype, recent work in other malignancies (Lee et al., 2016; Seiler et al., 2018b) supports the potential for particular benefit in the subset of patients carrying pathogenic splicing factor mutations.

**DISCUSSION:**

Our results demonstrate that PI therapy in myeloma leads to broad-scale interference with spliceosome function. This observation, initially generated through unbiased phosphoproteomics, led us to explore the spliceosome itself as a myeloma vulnerability. Our

bioRxiv preprint doi: https://doi.org/10.1101/508549; this version posted December 30, 2018. The copyright holder for this preprint (which was not certified by peer review) is the author/funder. All rights reserved. No reuse allowed without permission.

preclinical evaluation and analysis of functional genomics and exome sequencing data further reinforced the spliceosome as a therapeutic target in myeloma.

These results raise a number of intriguing questions. From a mechanistic perspective, much remains unknown about the relationship between upregulated phosphorylation on multiple splicing factors and splicing interference as assessed by increased IR. Prior work examining SR phosphorylation after cellular perturbation using Western blotting did not consistently show a broad hyperphosphorylation signature (Jakubauskiene et al., 2015; Ninomiya et al., 2011; Shin et al., 2004). Our results therefore illustrate the utility of unbiased phosphoproteomics to elucidate cancer drug response. Recent work suggests that additional kinases beyond the well-characterized SRPKs and CLKs may be involved in SR phosphorylation (Long et al., 2018; Shinde et al., 2017). However, in the context of drug-induced stress in cancer, the mechanism that leads to coordinated, upregulated phosphorylation across multiple splicing factors, whether via kinase activation or phosphatase inhibition, will be an important topic for future investigation.

Notably, it remains unclear what effect such broad-scale SR phosphorylation truly has upon splicing. Causal links have been noted in single transcript, *in vitro* systems (Cao et al., 1997; Prasad et al., 1999; Xiao and Manley, 1997), but isolating global effects of SR phosphorylation on splicing within cells have remained elusive. Our expression studies of SRSF1, the best-characterized member of this family, using a phosphomimetic mutant did not lead to prominent global changes on either IR or exon selection. Intriguingly, though, we did find that mimicking hyperphosphorylation surprisingly led to decreased interaction with the core spliceosome by AP-MS, in contrast to the current model (Zhou and Fu, 2013). Admittedly, our phosphomimetic construct likely does not fully recapitulate the complex phosphorylation biology of SRSF1 within cells (Ghosh and Adams, 2011), nor does it fully match the level of expression of endogenous SRSF1. Furthermore, using genetic approaches we cannot readily model phosphorylation changes on multiple SR proteins simultaneously, which may be necessary to elicit broader phenotypic effects. Despite these limitations, however, our WT expression studies provide a landscape of the SRSF1 cytosolic and nuclear interactome, which may inform future studies of SR protein biology in myeloma and other systems.

Based on our data, after PI treatment the observed splicing factor phosphorylation and IR phenotypes appear to be largely uncoupled. Furthermore, we found a clear dose-response effect in our data, where high levels of stress and cell death were necessary to generate prominent splicing factor phosphorylation. We found that under lower levels of cell death, the DNA alkylator melphalan led to minimal IR effects. These findings were consistent with another recent study evaluating alternative splicing after melphalan in MM cells, which also did not report prominent IR but did find specific alternative splicing of DNA-damage associated genes (Marchesini et al., 2017), as we also found (**Fig. 3D**). Here, Cfz, in contrast, led to widespread IR even in the absence of any notable cell death.

bioRxiv preprint doi: https://doi.org/10.1101/508549; this version posted December 30, 2018. The copyright holder for this preprint (which was not certified by peer review) is the author/funder. All rights reserved. No reuse allowed without permission.

This PI-specific interference with normal splicing even at minimal cytotoxicity may relate to the activation of the heat shock response. We found prominent heat shock chaperone induction even under a non-cytotoxic dose of the PI bortezomib in MM.1S cells (Liu et al., 2017). As previously shown in non-cancer cells, heat shock alone, without cell death, can lead to significant intron retention (Shalgi et al., 2014). One hypothesis is that this broad-scale inhibition of splicing acts in a similar fashion to translational inhibition after drug-induced stress: a way to conserve cellular resources and focus on only producing genes required for survival and the stress response. However, as described in our model of **Fig. 5E**, and evidenced by our mRNA-seq data after E7107 treatment (**Fig. 6A**), another possible result of widespread intron retention and downstream loss of normal protein production is significant decrease in cellular fitness and ultimately, cell death. There may be a quantitative threshold effect between these two outcomes that remains to be elucidated.

Here, we propose that the loss-of-fitness modality of drug-induced IR constitutes a previously unexplored mechanism of action of PIs. We further performed a preclinical evaluation of splicing inhibition in myeloma using E7107, finding potent anti-myeloma effects *in vitro*, *in vivo*, and *ex vivo* versus primary patient samples. From a therapeutic perspective, one of the major questions is the potential toxicity of targeting such an essential process as the catalytic spliceosome. However, our analysis of genetic dependency data and our *ex vivo* data with E7107 clearly demonstrates the potential to target core spliceosome subunits in MM while largely sparing normal cells. In fact, based on this analysis the spliceosome appears to be an even more promising target than the clinically-validated approach of targeting essential subunits of the proteasome. Furthermore, presumed efficacious doses (based on measured blood concentrations) of E7107 were largely well-tolerated in a Phase I clinical trial (Hong et al., 2014). While this molecule is no longer in clinical development, it is thought that E7107 visual toxicity was molecule-specific and is not a function of targeting the spliceosome in general (Lee and Abdel-Wahab, 2016). Our genomic analysis suggests that mutations in splicing factors, both well-characterized and less well-characterized, are found in a substantial fraction of MM patients. Newer generations of splicing inhibitors are currently in clinical trials for other hematologic malignancies (Seiler et al., 2018b) (NCT02841540) and may be of particular benefit for these patients. Our results support clinical investigation of these compounds in MM as an emerging approach to overcome PI resistance or enhance PI efficacy as combination therapy.

**Acknowledgements**

We thank Dr. Silvia Buonamici at H3 Biomedicine for providing E7107 and insightful discussions, Drs. Sandy Wong, Nina Shah, Jeffrey Wolf, and Tom Martin for collection of primary patient specimens, and Jacob Runyan for assisting in quality control of sequencing data. We thank Drs. Renata Burger and Christoph Driessen for providing INA-6 and AMO-1

bioRxiv preprint doi: https://doi.org/10.1101/508549; this version posted December 30, 2018. The copyright holder for this preprint (which was not certified by peer review) is the author/funder. All rights reserved. No reuse allowed without permission.

parental and bortezomib resistant cell lines, respectively. This work was supported by NIH/NHGRI T32HG008345 (to A.M.T.), the Damon Runyon Cancer Research Foundation Dale Frey Breakthrough Award (DFS 14-15), NIH/NCI K08CA184116, NIH/NIGMS DP2OD022552, and the UCSF Stephen and Nancy Grand Multiple Myeloma Translational Initiative (to A.P.W.) and NIH/NCI R01CA226851 (to A.N.B. and A.P.W.).

**Author Contributions**

H.H.H., I.F., C.L., P.B., M.C.M., M.M., and A.P.W. performed experiments and analyzed experimental data. A.M.T., Y-H.L., and A.B. analyzed transcriptomic and genomic data. J.M., P.P., and B.C.H. performed in vivo studies. H.H.H. and A.P.W. wrote the manuscript.

**Declaration of Interests**

The authors declare no relevant conflicts of interest.

**REFERENCES**

Anders, S., Pyl, P. T., and Huber, W. (2014). HTSeq--a Python framework to work with high-throughput sequencing data. Bioinformatics 31(2), 166-169.

Aubol, B.E., Serrano, P., Fattet, L., Wuthrich, K., and Adams, J.A. (2018). Molecular interactions connecting the function of the serine-arginine-rich protein SRSF1 to protein phosphatase 1. *J Biol Chem 293*, 16751-16760.

Brooks, A.N., Yang, L., Duff, M.O., Hansen, K.D., Park, J.W., Dudoit, S., Brenner, S.E., and Graveley, B.R. (2011). Conservation of an RNA regulatory map between Drosophila and mammals. *Genome Res 21*, 193-202.

Caceres, J.F., Misteli, T., Screaton, G.R., Spector, D.L., and Krainer, A.R. (1997). Role of the modular domains of SR proteins in subnuclear localization and alternative splicing specificity. *J Cell Biol 138*, 225-238.

Caceres, J.F., Screaton, G.R., and Krainer, A.R. (1998). A specific subset of SR proteins shuttles continuously between the nucleus and the cytoplasm. *Genes Dev 12*, 55-66.

Cao, W., Jamison, S.F., and Garcia-Blanco, M.A. (1997). Both phosphorylation and dephosphorylation of ASF/SF2 are required for pre-mRNA splicing in vitro. *RNA 3*, 1456-1467.

Casado, P., Hijazi, M., Britton, D., and Cutillas, P.R. (2017). Impact of phosphoproteomics in the translation of kinase-targeted therapies. *Proteomics 17*.

Casado, P., Rodriguez-Prados, J.C., Cosulich, S.C., Guichard, S., Vanhaesebroeck, B., Joel, S., and Cutillas, P.R. (2013). Kinase-substrate enrichment analysis provides insights into the heterogeneity of signaling pathway activation in leukemia cells. *Sci Signal 6*, rs6.

bioRxiv preprint doi: https://doi.org/10.1101/508549; this version posted December 30, 2018. The copyright holder for this preprint (which was not certified by peer review) is the author/funder. All rights reserved. No reuse allowed without permission.

Cho, S., Hoang, A., Sinha, R., Zhong, X.Y., Fu, X.D., Krainer, A.R., and Ghosh, G. (2011). Interaction between the RNA binding domains of Ser-Arg splicing factor 1 and U1-70K snRNP protein determines early spliceosome assembly. *Proc Natl Acad Sci USA 108*, 8233-8238.

Chen, E. Y., Tan, C. M., Kou, Y., Duan, Q., Wang, Z., Meirelles, G. V., Clark, N. R., Ma'ayan, A. (2013). Enrichr: interactive and collaborative HTML5 gene list enrichment analysis tool. BMC Bioinformatics. 128(14).

Colwill, K., Pawson, T., Andrews, B., Prasad, J., Manley, J.L., Bell, J.C., and Duncan, P.I. (1996). The Clk/Sty protein kinase phosphorylates SR splicing factors and regulates their intranuclear distribution. *EMBO J 15*, 265-275.

Das, R., Yu, J., Zhang, Z., Gygi, M.P., Krainer, A.R., Gygi, S.P., and Reed, R. (2007). SR proteins function in coupling RNAP II transcription to pre-mRNA splicing. *Mol Cell 26*, 867-881.

Cox, J. and Mann, M. (2008). MaxQuant enables high peptide identification rates, individualized p.p.b.-range mass accuracies and proteome-wide protein quantification. Nat Biotechnol 26, 1367-72.

Cox, J., Hein, M. Y., Luber, C. A., Paron, I., Nagaraj, N., and Mann, M., (2014). Accurate Proteome-wide Label-free Quantification by Delayed Normalization and Maximal Peptide Ratio Extraction, Termed MaxLFQ. Mol Cell Proteomics 13, 2513–2526.

Fedorov, O., Huber, K., Eisenreich, A., Filippakopoulos, P., King, O., Bullock, A.N., Szklarczyk, D., Jensen, L.J., Fabbro, D., Trappe, J.*, et al.* (2011). Specific CLK inhibitors from a novel chemotype for regulation of alternative splicing. *Chem Biol 18*, 67-76.

Gandolfi, S., Laubach, J.P., Hideshima, T., Chauhan, D., Anderson, K.C., and Richardson, P.G. (2017). The proteasome and proteasome inhibitors in multiple myeloma. *Cancer Metastasis Rev 36*, 561-584.

Ghosh, G., and Adams, J.A. (2011). Phosphorylation mechanism and structure of serine-arginine protein kinases. *FEBS J 278*, 587-597.

Han, T., Goralski, M., Gaskill, N., Capota, E., Kim, J., Ting, T.C., Xie, Y., Williams, N.S., and Nijhawan, D. (2017). Anticancer sulfonamides target splicing by inducing RBM39 degradation via recruitment to DCAF15. *Science 356*.

Hong, D.S., Kurzrock, R., Naing, A., Wheler, J.J., Falchook, G.S., Schiffman, J.S., Faulkner, N., Pilat, M.J., O'Brien, J., and LoRusso, P. (2014). A phase I, open-label, single-arm, dose-escalation study of E7107, a precursor messenger ribonucleic acid (pre-mRNA) splicesome inhibitor administered intravenously on days 1 and 8 every 21 days to patients with solid tumors. *Invest New Drugs 32*, 436-444.

Hornbeck, P.V., Zhang, B., Murray, B., Kornhauser, J.M., Latham, V., Skrzypek, E. (2015) PhosphoSitePlus, 2014: mutations, PTMs and recalibrations. Nucleic Acids Res. 43, D512-D520.

bioRxiv preprint doi: https://doi.org/10.1101/508549; this version posted December 30, 2018. The copyright holder for this preprint (which was not certified by peer review) is the author/funder. All rights reserved. No reuse allowed without permission.

Huang, Y., Gattoni, R., Stevenin, J., and Steitz, J.A. (2003). SR splicing factors serve as adapter proteins for TAP-dependent mRNA export. *Mol Cell 11*, 837-843.

Ianevski, A., He, L., Aittokallio, T., Tang, J. (2017). SynergyFinder: a web application for analyzing drug combination dose–response matrix data. Bioinformatics 33(15), 2413–2415.

Jakubauskiene, E., Vilys, L., Makino, Y., Poellinger, L., and Kanopka, A. (2015). Increased Serine-Arginine (SR) Protein Phosphorylation Changes Pre-mRNA Splicing in Hypoxia. *J Biol Chem 290*, 18079-18089.

Karni, R., de Stanchina, E., Lowe, S.W., Sinha, R., Mu, D., and Krainer, A.R. (2007). The gene encoding the splicing factor SF2/ASF is a proto-oncogene. *Nat Struct Mol Biol 14*, 185-193.

Kim, D., Langmead, B., and Salzberg, S. L. (2015). HISAT: a fast spliced aligner with low memory requirements. Nature methods 12(4), 357-360.

Kuleshov, M. V., Jones, M. R., Rouillard, A. D., Fernandez, N. F., Duan, Q., Wang, Z., Koplev, S., Jenkins, S. L., Jagodnik, K. M., Lachmann, A., McDermott, M. G., Monteiro, C. D., Gundersen, G. W., Ma'ayan, A. (2016). Enrichr: a comprehensive gene set enrichment analysis web server 2016 update. Nucleic Acids Research 44, W90-W97.

Le Moigne, R., Aftab, B.T., Djakovic, S., Dhimolea, E., Valle, E., Murnane, M., King, E.M., Soriano, F., Menon, M.K., Wu, Z.Y.*, et al.* (2017). The p97 inhibitor CB-5083 is a unique disrupter of protein homeostasis in models of Multiple Myeloma. *Mol Cancer Therap*. *16*, 2375-86.

Lee, A.H., Iwakoshi, N.N., Anderson, K.C., and Glimcher, L.H. (2003). Proteasome inhibitors disrupt the unfolded protein response in myeloma cells. *Proc Natl Acad Sci USA 100*, 9946-9951.

Lee, S.C., and Abdel-Wahab, O. (2016). Therapeutic targeting of splicing in cancer. *Nat Med 22*, 976-986.

Lee, S.C., Dvinge, H., Kim, E., Cho, H., Micol, J.B., Chung, Y.R., Durham, B.H., Yoshimi, A., Kim, Y.J., Thomas, M.*, et al.* (2016). Modulation of splicing catalysis for therapeutic targeting of leukemia with mutations in genes encoding spliceosomal proteins. *Nat Med 22*, 672-678.

Li, H., Handsaker, B., Wysoker, A., Fennell, T., Ruan, J., Homer, N., Marth, G., Abecasis, G., Durbin, R., 1000 Genome Project Data Processing Subgroup (2009). The Sequence Alignment/Map format and SAMtools. Bioinformatics 25(16), 2078-2079.

Li, X., Colvin, T., Rauch, J.N., Acosta-Alvear, D., Kampmann, M., Dunyak, B., Hann, B., Aftab, B.T., Murnane, M., Cho, M.*, et al.* (2015). Validation of the Hsp70-Bag3 protein-protein interaction as a potential therapeutic target in cancer. *Mol Cancer Therap 14*, 642-648.

Liu, T.Y., Huang, H.H., Wheeler, D., Xu, Y., Wells, J.A., Song, Y.S., and Wiita, A.P. (2017). Time-Resolved Proteomics Extends Ribosome Profiling-Based Measurements of Protein Synthesis Dynamics. *Cell Syst 4*, 636-644 e639.

bioRxiv preprint doi: https://doi.org/10.1101/508549; this version posted December 30, 2018. The copyright holder for this preprint (which was not certified by peer review) is the author/funder. All rights reserved. No reuse allowed without permission.

Long, J.C., and Caceres, J.F. (2009). The SR protein family of splicing factors: master regulators of gene expression. *Biochem J 417*, 15-27.

Long, Y., Sou, W.H., Yung, K.W.Y., Liu, H., Wan, S.W.C., Li, Q., Zeng, C., Law, C.O.K., Chan, G.H.C., Lau, T.C.K.*, et al.* (2018). Distinct mechanisms govern the phosphorylation of different SR protein splicing factors. *J Biol Chem.* ePub ahead of print.

Love, M. I., Huber, W., & Anders, S. (2014). Moderated estimation of fold change and dispersion for RNA-seq data with DESeq2. Genome biology 15(12), 550.

Marchesini, M., Ogoti, Y., Fiorini, E., Aktas Samur, A., Nezi, L., D'Anca, M., Storti, P., Samur, M.K., Ganan-Gomez, I., Fulciniti, M.T.*, et al.* (2017). ILF2 Is a Regulator of RNA Splicing and DNA Damage Response in 1q21-Amplified Multiple Myeloma. *Cancer Cell 32*, 88-100 e106.

McMillin, D.W., Negri, J.M., and Mitsiades, C.S. (2013). The role of tumour-stromal interactions in modifying drug response: challenges and opportunities. *Nat Rev Drug Discov 12*, 217-228.

McMillin, D. W., Delmore, J., Weisberg, E., Negri, J.M., Geer, D. C., Klippel, S., Mitsiades, N., Schlossman, R. L., Munshi, N. C., Kung, A. L., Griffin, J. D., Richardson, P. G., Anderson, K. C., and Mitsiades, C. S. (2010). Tumor cell-specific bioluminescence platform to identify stroma-induced changes to anticancer drug activity. Nature medicine 16, 438-489.

Misteli, T., Caceres, J.F., Clement, J.Q., Krainer, A.R., Wilkinson, M.F., and Spector, D.L. (1998). Serine phosphorylation of SR proteins is required for their recruitment to sites of transcription in vivo. *J Cell Biol 143*, 297-307.

Misteli, T., Caceres, J.F., and Spector, D.L. (1997). The dynamics of a pre-mRNA splicing factor in living cells. *Nature 387*, 523-527.

Mitra, A.K., Harding, T., Mukherjee, U.K., Jang, J.S., Li, Y., HongZheng, R., Jen, J., Sonneveld, P., Kumar, S., Kuehl, W.M.*, et al.* (2017). A gene expression signature distinguishes innate response and resistance to proteasome inhibitors in multiple myeloma. *Blood Cancer J 7*, e581.

Mitsiades, N., Mitsiades, C.S., Poulaki, V., Chauhan, D., Fanourakis, G., Gu, X., Bailey, C., Joseph, M., Libermann, T.A., Treon, S.P.*, et al.* (2002). Molecular sequelae of proteasome inhibition in human multiple myeloma cells. *Proc Natl Acad Sci USA 99*, 14374-14379.

Ngo, J.C., Chakrabarti, S., Ding, J.H., Velazquez-Dones, A., Nolen, B., Aubol, B.E., Adams, J.A., Fu, X.D., and Ghosh, G. (2005). Interplay between SRPK and Clk/Sty kinases in phosphorylation of the splicing factor ASF/SF2 is regulated by a docking motif in ASF/SF2. *Mol Cell 20*, 77-89.

Ninomiya, K., Kataoka, N., and Hagiwara, M. (2011). Stress-responsive maturation of Clk1/4 pre-mRNAs promotes phosphorylation of SR splicing factor. *J Cell Biol 195*, 27-40.

Obeng, E.A., Carlson, L.M., Gutman, D.M., Harrington, W.J., Jr., Lee, K.P., and Boise, L.H. (2006). Proteasome inhibitors induce a terminal unfolded protein response in multiple myeloma cells. *Blood 107*, 4907-4916.

bioRxiv preprint doi: https://doi.org/10.1101/508549; this version posted December 30, 2018. The copyright holder for this preprint (which was not certified by peer review) is the author/funder. All rights reserved. No reuse allowed without permission.

Prasad, J., Colwill, K., Pawson, T., and Manley, J.L. (1999). The protein kinase Clk/Sty directly modulates SR protein activity: both hyper- and hypophosphorylation inhibit splicing. *Mol Cell Biol 19*, 6991-7000.

R Core Team (2018). R: A language and environment for statistical computing. R Foundation for Statistical Computing, Vienna, Austria. URL https://www.R-project.org/.

Ran, F.A., Hsu, P.D., Wright, J., Agarwala, V., Scott, D.A., Zhang, F. (2013). Genome engineering using the CRISPR-Cas9 system. Nat Protoc. 8(11), 2281-2308.

Rasband, W.S., ImageJ, U. S. National Institutes of Health, Bethesda, Maryland, USA, https://imagej.nih.gov/ij/, 1997-2018.

Saez, B., Walter, M.J., and Graubert, T.A. (2017). Splicing factor gene mutations in hematologic malignancies. *Blood 129*, 1260-1269.

Seiler, M., Peng, S., Agrawal, A.A., Palacino, J., Teng, T., Zhu, P., Smith, P.G., Cancer Genome Atlas Research, N., Buonamici, S., and Yu, L. (2018a). Somatic Mutational Landscape of Splicing Factor Genes and Their Functional Consequences across 33 Cancer Types. *Cell Rep 23*, 282-296 e284.

Seiler, M., Yoshimi, A., Darman, R., Chan, B., Keaney, G., Thomas, M., Agrawal, A.A., Caleb, B., Csibi, A., Sean, E.*, et al.* (2018b). H3B-8800, an orally available small-molecule splicing modulator, induces lethality in spliceosome-mutant cancers. *Nat Med 24*, 497-504.

Shah, S.P., Lonial, S., and Boise, L.H. (2015). When Cancer Fights Back: Multiple Myeloma, Proteasome Inhibition, and the Heat-Shock Response. *Mol Cancer Res 13*, 1163-1173.

Shalgi, R., Hurt, J.A., Lindquist, S., and Burge, C.B. (2014). Widespread inhibition of posttranscriptional splicing shapes the cellular transcriptome following heat shock. *Cell Rep 7*, 1362-1370.

Shin, C., Feng, Y., and Manley, J.L. (2004). Dephosphorylated SRp38 acts as a splicing repressor in response to heat shock. *Nature 427*, 553-558.

Shinde, M.Y., Sidoli, S., Kulej, K., Mallory, M.J., Radens, C.M., Reicherter, A.L., Myers, R.L., Barash, Y., Lynch, K.W., Garcia, B.A.*, et al.* (2017). Phosphoproteomics reveals that glycogen synthase kinase-3 phosphorylates multiple splicing factors and is associated with alternative splicing. *J Biol Chem 292*, 18240-18255.

Soriano, G.P., Besse, L., Li, N., Kraus, M., Besse, A., Meeuwenoord, N., Bader, J., Everts, B., den Dulk, H., Overkleeft, H.S.*, et al.* (2016). Proteasome inhibitor-adapted myeloma cells are largely independent from proteasome activity and show complex proteomic changes, in particular in redox and energy metabolism. *Leukemia*. *30*, 2198-207.

Suraweera, A., Munch, C., Hanssum, A., and Bertolotti, A. (2012). Failure of amino acid homeostasis causes cell death following proteasome inhibition. *Mol Cell 48*, 242-253.

Szklarczyk, D., Morris, J.H., Cook, H., Kuhn, M., Wyder, S., Simonovic, M., Santos, A., Doncheva, N. T., Roth, A., Bork, P., Jensen, L. J., von Mering, C. (2017). The STRING

bioRxiv preprint doi: https://doi.org/10.1101/508549; this version posted December 30, 2018. The copyright holder for this preprint (which was not certified by peer review) is the author/funder. All rights reserved. No reuse allowed without permission.

database in 2017: quality-controlled protein-protein association networks, made broadly accessible. Nucleic Acids Res. 45, D362-D368.

Traenckner, E.B., Wilk, S., and Baeuerle, P.A. (1994). A proteasome inhibitor prevents activation of NF-kappa B and stabilizes a newly phosphorylated form of I kappa B-alpha that is still bound to NF-kappa B. *EMBO J 13*, 5433-5441.

Trapnell, C., Williams, B., Pertea, G., Mortazavi, A., Kwan, G., van Baren, J., Salzberg, S., Wold, B., Pachter, L. (2010). Transcript assembly and quantification by RNA-Seq reveals unannotated transcripts and isoform switching during cell differentiation. Nature Biotechnology 28(5), 511-515.

Tsherniak, A., Vazquez, F., Montgomery, P.G., Weir, B.A., Kryukov, G., Cowley, G.S., Gill, S., Harrington, W.F., Pantel, S., Krill-Burger, J.M.*, et al.* (2017). Defining a Cancer Dependency Map. *Cell 170*, 564-576 e516.

Tyanova, S., Temu, T., and Cox, J., (2016). The MaxQuant computational platform for mass spectrometry-based shotgun proteomics, Nat Protocols 11, 2301–2319.

Tyanova, S., Temu, T., Sinitcyn, P., Carlson, A., Hein M. Y., Geiger, T., Mann, M., and Cox, J. (2016). The Perseus computational platform for comprehensive analysis of (prote)omics data. Nature Methods 13, 731–740.

Vizcaíno, J.A., Csordas, A., del-Toro, N., Dianes, J.A., Griss, J., Lavidas, I., Mayer, G., Perez-Riverol, Y., Reisinger, F., Ternent, T., Xu, Q.W., Wang, R., Hermjakob, H. (2016). 2016 update of the PRIDE database and related tools. Nucleic Acids Res 44(D1), D447-D456

Wahl, M.C., Will, C.L., and Luhrmann, R. (2009). The spliceosome: design principles of a dynamic RNP machine. *Cell 136*, 701-718.

Wallington-Beddoe, C.T., Sobieraj-Teague, M., Kuss, B.J., and Pitson, S.M. (2018). Resistance to proteasome inhibitors and other targeted therapies in myeloma. *Br J Haematol 182*, 11-28.

Walter, P., and Ron, D. (2011). The unfolded protein response: from stress pathway to homeostatic regulation. *Science 334*, 1081-1086.

Wiredja, D.D., Koyutürk, M., Chance, M.R. (2017) The KSEA App: a web-based tool for kinase activity inference from quantitative phosphoproteomics. Bioinformatics 33(21), 3489-3491.

Wiita, A.P., Ziv, E., Wiita, P.J., Urisman, A., Julien, O., Burlingame, A.L., Weissman, J.S., and Wells, J.A. (2013). Global cellular response to chemotherapy-induced apoptosis. *eLife 2*, e01236.

Xiao, S.H., and Manley, J.L. (1997). Phosphorylation of the ASF/SF2 RS domain affects both protein-protein and protein-RNA interactions and is necessary for splicing. *Genes Dev 11*, 334-344.

Yadav, B., Wennerberg, K., Aittokallio, T., and Tang, J. (2015). Searching for Drug Synergy in Complex Dose-Response Landscapes Using an Interaction Potency Model. *Comp Struct Biotechnol J 13*, 504-513.

bioRxiv preprint doi: https://doi.org/10.1101/508549; this version posted December 30, 2018. The copyright holder for this preprint (which was not certified by peer review) is the author/funder. All rights reserved. No reuse allowed without permission.

Zhou, Z., and Fu, X.D. (2013). Regulation of splicing by SR proteins and SR protein-specific kinases. *Chromosoma 122*, 191-207.

Yang, X., Boehm, J. S., Yang, X., Salehi-Ashtiani, K., Hao, J., Shen, Y., Lubonja, R., Thomas, S. R., Alkan, O., Bhimdi, T., Green, T. M., Johannessen, C. M., Silver, S. J., Nguyen, C., Murray, R. R., Hieronymus, H., Balcha, D., Fan, C., Lin, C., Ghamsari, L., Vidal, M., Hahn, W. C., Hill, D. E., Root, D. E. (2011). A public genome-scale lentiviral expression library of human ORFs. Nature Methods 8, 659–661.

**Main Figure Titles and Legends**

**Figure 1. Unbiased phosphoproteomic timecourse analysis of MM.1S cells treated with the PI carfilzomib (Cfz). A.** Workflow of timecourse treatment of MM.1S cells with 30 nM Cfz over 24h. Cells were allotted for both RNA-seq analysis and LC-MS/MS. Phosphopeptides were enriched using Fe3+-NTA immobilized metal affinity chromatography (IMAC). **B.** Downregulated (left) and upregulated (right) $\log_2$ transformed phospho-peptide mass spec intensities for two technical replicates of proteins with relatively unchanged transcript levels (RNA-seq). Labels highlight dephosphorylation of known stress-responsive phosphosites on RPS6 and EIF4EBP1 on the left and increased phosphorylation of splicing-related proteins on the right.

**Figure 2. Cfz induces phosphorylation of splicing factors in a dose-responsive manner. A-D.** Volcano plots showing $\log_2$ transformed ratios of phosphosite abundances between **A.** MM.1S treated with18 nM Cfz, **B.** treated with10 nM Cfz, or **D.** treated with 10 μM melphalan compared to MM.1S treated with DMSO and **C.** AMO-1 treated with 15 nM Cfz vs, AMO-1 treated with DMSO, all for 24 hr. Significantly upregulated sites (>2-fold increase, T-test $p < 0.05$) are in red, while downregulated (>2-fold decrease, T-test $p < 0.05$) are in blue. Sites belonging to SRSF family proteins are in orange. Size of circles correspond to summed light and heavy SILAC signal intensities. **E.** Top-ranked (FDR q-value) GO enrichment terms for genes with significantly upregulated phosphosites in MM.1S cells treated with 18 nM Cfz for 24 h. **F**. Top-ranked (Kinase Z-score) activated kinases (with at least 5 substrates) as determined by KSEA for MM.1S treated with 18 nM Cfz (top) and 10 μM melphalan for 24 h.

**Figure 3. Cfz treatment leads to prominent intron retention. A.** Cartoon description of different forms of alternative splicing events (ASE) and description of evaluation of ΔPSI. **B.** Histograms of ΔPSI for JUNCBase identified ASE's in MM.1S treated with 18 nM Cfz stratified according to type of splicing event (IR = yellow, alternative exon acceptor = blue, alt. 1st exon = green, alt. last exon = purple). Bin = 2, red line indicates ΔPSI = 0. **C.** Histograms of ΔPSI for all intron retention events in AMO-1 cells treated with 15 nM Cfz (left) and MM.1S cells 10 μM

bioRxiv preprint doi: https://doi.org/10.1101/508549; this version posted December 30, 2018. The copyright holder for this preprint (which was not certified by peer review) is the author/funder. All rights reserved. No reuse allowed without permission.

melphalan (right). **D.** Top ranked (log10 Fisher's T-test p-val * rank deviation weighted Z-score) GO enrichment analysis terms for genes with significant ($p < 0.05$) ASEs for MM.1S cells treated with 18 nM Cfz (left) and MM.1S cells treated with 10 μM melphalan (right).

**Figure 4. Modeling SRSF1 phosphorylation in MM drives interactome dynamics but not global splicing changes. A.** Cartoon of protein architecture for exogenous SRSF1-NLS-mCherry-[FLAG]3 construct. Phospho-mimetic mutant (SD) replaces all 20 Ser with Asp in RS-domain, while phospho-dead mutant (SA) replaces Ser with Ala. **B.** Epi-fluorescent imaging of DAPI stained AMO-1 expressing mCherry (m) labeled SRSF1 WT (top), SRSF1mSD (middle), and SRSF1mSA (bottom). Scalebar represents 10 μM. **C and D.** Histograms of ΔPSI for IR, alt. exon acceptor, alt. 1st exon, alt. last exon ASE's in AMO-1 expressing **C.** SRSF1 WT treated with 15 nM Cfz compared to DMSO and **D.** SRSF1mSD compared to SRSF1 WT. E. Volcano plots indicating differential interactors of SRSF1mSD compared to WT in both the nucleus and cytoplasmic fractions of AMO-1. F. Specific interactors enriched with SRSF1 WT and SRSF1mSD compared to NLS-mCherry-[FLAG]3 control in AMO-1 nucleus reveals preferential association of WT SRSF1 with spliceosome compared to SD. Significantly enriched proteins in pink, de-enriched proteins in cyan ($p < 0.05$, > 2-fold change). Size of circles corresponds to summed LFQ intensities. mCherry ratio is in red and SRSF1 ratio is in yellow.

**Figure 5. Combined SRSF1 constructs validate the IR phenotype after Cfz. A.** Histograms of ΔPSI for all stratified ASE's in pooled parental AMO-1, AMO-1 SRSF1 WT, SRSF1mSD, SRSF1mSA expressing cells treated with 15 nM Cfz with respect to all pooled parental AMO-1 and AMO-1 SRSF1 constructs in DMSO after 24 h. **B.** Graph shows number of total events (n = 62,474) for each ASE stratification (left) vs only the significant (FDR-corrected $p < 0.05$) events (n = 2,575) for each stratification (right). **C.** Top ranked (log10 Fisher's T-test p-val * rank deviation weighted Z-score) terms from GO enrichment analysis of all genes involved in significant ASE's, regardless of type of splicing. **D.** Bar graph represents differential RNA-seq counts for the proteasomal subunit PSMC5 between AMO-1 treated with 15 nM cfz (bottom) and AMO-1 treated with DMSO (top). Inset displays sequencing counts showing alternative first exon. **E.** Cartoon depicting proposed model of MM cell response and cell fate decision process when treated with proteasome inhibitor.

**Figure 6. The catalytic spliceosome inhibitor E7107 induces IR and has potent anti-MM activity in vitro. A.** Histogram of ΔPSI of JUNCBase identified IR events for MM.1S cells treated with 10 nM E7107 for 6 h with respect to DMSO. Bin = 2 and red line at ΔPSI = 0. **B.** Dose-response curves measure cell viability of a panel of 7 MM cell lines treated with E7107 for 48 h (n=4; mean +/- S.D.). **C.** Dose-response curves compare the cell viability of WT AMO-1

bioRxiv preprint doi: https://doi.org/10.1101/508549; this version posted December 30, 2018. The copyright holder for this preprint (which was not certified by peer review) is the author/funder. All rights reserved. No reuse allowed without permission.

and PI-resistant AMO-1 cell line (BtzR) when treated with E7107 (n=4; mean +/- S.D.) **D.** Evaluation of SF3B1 expression by RNAseq (top; FPKM expression data from www.keatslab.org, mean +/- S.D.) and Western blot (bottom) across more E7107-sensitive (AMO-1, INA6, L363, and RPMI8266) and less E7107-sensitive (MM.1S, KMS34, JJN3) cell lines. **E.** Dose-response curves showing MM.1S viability with E7107 in combination with Cfz (n=4; mean +/- S.D.) **F.** 2-D heatmap of ZIP synergy-scored landscape in MM.1S Cfz and E7107 combination study. Red = synergy; green = antagonism; white = additive. Overall ZIP score of 6.295 suggests strong synergy. **G and H.** Same as E. and F. but for melphalan + E7107 combination. Overall ZIP synergy score of 2.663 denotes weaker synergy than with Cfz.

**Figure 7. Inhibition of the spliceosome is a promising therapeutic strategy in myeloma.** **A-B.** Bioluminescence imaging of luc-labeled MM.1S cells implanted intravenously in NSG mice treated with either Vehicle (left, n = 6) or 3 mg/kg I.V. E7107 (right, n = 6). Drug or vehicle were administered daily on Days 14-18 and 21-25 after tumor implantation. **C.** E7107 leads to significant improvement in murine survival (p = 0.01 by Log-ranked test) **D.** Treatment of primary bone marrow aspirate samples from PI-refractory myeloma patients at various doses of E7107 for 48 hr demonstrates significant cytotoxicity to CD138+ MM plasma cells at low-nM concentrations but minimal effects on other (CD138-) hematopoietic cells in the marrow (n=2 technical replicates; mean +/- S.D.). **E.** Analysis of CRISPR-Cas9 essentiality screen data in the Cancer Dependency Map (www.depmap.org; Avana 18Q4 release) demonstrates that myeloma cell lines appear to be the most genetically dependent on “common essential” core subunits of the U1-U2 spliceosome among all tested tumor cell types. **F.** Analysis of data in the MMRF CoMMpass database (research.themmrf.org; release **IA11**) demonstrates mutations with possible functional effects in numerous splicing-relating factors (as defined by Seiler et al., 2018a) within MM patient plasma cells. Table of variant allele frequencies can be found in **Supplemental Dataset 3**.

**Supplemental Figure Titles and Legends:**

**Figure S1. Time-course of MM cell phosphorylation after Cfz treatment. A.** Heatmap with all 5791 quantified phosphosites, $\log_2$-transformed label-free quantification (LFQ) intensity ratios (relative to 0 h at 8, 16, 24 hr) for 2 technical replicates of MM.1S cells treated with 30 nM Cfz over a 24 h time course. **B.** Top ranked (FDR *q*-value) GO enrichment terms for genes with increased phosphorylation and relatively unchanged transcript levels as a proxy for protein abundance increase (**Fig. 1 B**) over 24 h.

**Figure S2. Protein abundance and gene expression respone to drug perturbation.** Volcano plots showing $\log_2$ transformed ratios of single time-point SILAC-based LC-MS/MS

bioRxiv preprint doi: https://doi.org/10.1101/508549; this version posted December 30, 2018. The copyright holder for this preprint (which was not certified by peer review) is the author/funder. All rights reserved. No reuse allowed without permission.

protein intensities of MM cells treated with **A.** 18 nM Cfz, **B.** 10 nM Cfz. **C.** 15 nM Cfz (AMO-1), or **D.** 10 μM melphalan, compared to DMSO. Red circles are proteins with significantly increasing abundances ($p < 0.05$, > 2-fold increase), blue circles are significantly decreasing proteins ($p < 0.05$, > 2-fold decrease), and orange circles belong to SRSF family of proteins. Size of dots correspond to summed SILAC light and heavy signals for each protein. **E.** Volcano plot of $\log_2$ transformed ratio of changes in gene expression for MM.1S treated with 18 nM Cfz, compared to DMSO, with significantly changed genes in green ($p < 0.05$, > 2-fold). **F.** Normalized SILAC LC-MS/MS intensity ratios for phosphopeptides enriched from MM.1S cells treated with 50 μM KH-CB19 versus DMSO for 24 hr. Red and blue circles are significantly changed sites ($p < 0.05$, >2-fold). Notably, detected SRSF phosphopeptides (orange circles) do not change significantly in response to CLK1/4 inhibitor. Dot size corresponds to summed SILAC intensities of the phosphopeptides.

**Figure S3. Characterization of myeloma response to Cfz and melphalan. A.** Normalized cell viability (by CellTiterGlo) vs. DMSO control of MM cells treated with indicated drugs for 24 h. (n=3; mean +/- S.D.). **B.** Representative scatter plot showing correlation between 2 biological replicates for normalized SILAC ratios (left) and summed (light + heavy, right) intensities for phosphosites from MM.1S treated with 18 nM Cfz shows high quantitative reproducibility. **C.** Immunoblot of stress biomarkers (PERK, BiP, phospho-/total eIF2α, phospho-/total 4EBP1) for AMO-1 treated with DMSO, 10 nM, 15 nM Cfz, MM.1S treated with DMSO, 10nM Cfz, and 15 nM Cfz, and MM.1S treated with DMSO, 15 μM melphalan, and 20 μM melphalan. Vertical lines indicate excised lanes containing ladder or irrelevant conditions. **D.** Immunoblot of biomarkers for DNA damage (phospho-CHK1, phospho-H2AX) for AMO-1 and MM.1S treated with DMSO, 15 nM Cfz, and 10 μM melphalan, showing activation of DNA damage response only with melphalan. **E.** Immunoblot of core spliceosome components, U2AF2, SF3B1, and SF3A1 showing Caspase-3 cleavage (* in red) from MM.1S treated with Cfz for 18 h with and without 50 μM of Caspase inhibitor zVAD-fmk. Note that under these conditions viability after 7.5 nM Cfz = 70%; 10 nM Cfz = 54%. Viability 100% after zVAD-fmk treatment at both doses. **F.** Western blot for SRSF1, SRSF3, and SRSF6 in MM.1S and AMO-1 treated with DMSO and Cfz. Cell extract treated with calf intestinal phosphatase (+ CIP) to highlight retarded migration of phosphorylated species of SRSF proteins. Ponceau-S stain included as loading control.

**Figure S4. Cfz-induced splicing alterations across SRSF constructs. A.** List of PCR reactions referencing oligos in **Table S1**.and the subsequent Gibson Assemblies to generate lentiviral SRSF1 plasmids. IDs are related to SRSF1 WT or mutants: A4 and B2 = WT, I1 and II2 = SD, III1/X3 and IV3/X4 = SA. **B.** Normalized cell viability of AMO-1 cells expressing SRSF1 WT, SRSF1mSD, and SRSF1mSA treated with 15 nM Cfz for 24 h (*n*=3; mean +/-

bioRxiv preprint doi: https://doi.org/10.1101/508549; this version posted December 30, 2018. The copyright holder for this preprint (which was not certified by peer review) is the author/funder. All rights reserved. No reuse allowed without permission.

S.D.). **C.** anti-SRSF1 immunoblot of parental AMO-1, AMO-1 expressing exogeneous SRSF1WT, SRSF1mSD, and SRSF1mSA, comparing exogenous SRSF1-mCherry-NLS-$[FLAG]_3$ and endogenous SRSF1 abundance. **D.** Top ranked (combined Fisher's p-value and background weighted Z-score) GO enrichment terms for genes with significant ASE ($p < 0.05$) of all types from AMO-1 SRSF1 WT treated with 15 nM Cfz compared to DMSO (left) and AMO-1 SRSF1mSD in DMSO compared to AMO-1 SRSF1 WT in DMSO (right). **E.** Examples of Cfz-induced alternative splicing: alternative first exon splicing in KIAA 1217 (top) and intron retention in CNNM3 (bottom) for all AMO-1 cells (parental, SRSF1 WT, SD, SA) with 15 nM Cfz compared to DMSO.

**Figure S5. The phosphorylation-dependent interactome of SRSF1. A.** Volcano plot showing AP-MS enriched interaction partners to SRSF1 WT (*left*) and SRSF1mSD (*right*) compared with mCherry-NLS-$[FLAG]_3$ control in AMO-1 cytoplasm. Significantly enriched proteins ($p < 0.05$, > 2-fold) are in pink and excluded proteins in cyan. Dot size corresponds to combined LFQ intensities for that protein. Proteasomal subunits are colored in brown. **B.** Top ranked (FDR *q*-value) GO enrichment terms for significantly enriched interaction partners for SRSF1 WT and SRSF1mSD compared to mCherry-NLS-$[FLAG]_3$ control in either the nucleus or cytoplasm of AMO-1. **C and E**. Volcano plots depicting differential interaction partners of SRSF1mSA compared to SRSF1 WT (*left*) and SRSF1mSA enriched proteins compared to control (*right*) in **C)** the cytoplasm and **E)** the nucleus of AMO-1. Significantly enriched and excluded proteins ($p < 0.05$, > 2-fold) in pink and cyan. Heat shock proteins colored in green. **D and F.** Top ranked (FDR *q*-value) GO enrichment terms for significantly enriched interaction partners for SRSF1mSA in either the **D)** cytoplasm or **F)** nucleus of AMO-1.

**Figure S6. E7107 cell toxicity and functional splicing assay. A.** Normalized cell viability measurements (by CellTiterGlo assay) with respect to time for MM.1S (top) and AMO-1 (bottom) treated with increasing E7107 concentration, per protocol of Seiler et al. (2018b). Cells with a washout of E7107 (with exchanged media) at 6 h have pink and red outlines, while cells without washout are shown with gray and black outlines. **B.** Bar graph depicting $\log_2$ transformed ratio of transcript abundance between cells treated with 10 nM E7107 for 6 h, and DMSO, via qPCR ΔΔCt values (with respect to housekeeping gene PPIA) of pre-splice and splice competent forms of two mRNA targets (MBD4 in blue and FBXW5 in green) in MM.1S (top) and AMO-1 cells confirm significant intron retention of canonical targets at this dose and time point. Error bars represent standard deviation of technical replicates ($n$=3).

**Figure S7. Preclinical and clinical relevance of targeting the spliceosome in myeloma. A.** 3 mg/kg I.V. E7107 leads to minimal weight loss in NSG mice (mean +/- S.D.; $n$=6 per arm). **B.**

bioRxiv preprint doi: https://doi.org/10.1101/508549; this version posted December 30, 2018. The copyright holder for this preprint (which was not certified by peer review) is the author/funder. All rights reserved. No reuse allowed without permission.

Example flow cytometry plots from primary MM patient bone marrow aspirates. Gated region indicates CD138+ plasma cells. **C.** DepMap (www.depmap.org) CRISPR screen (Avana library 18Q4) dependency data indicating that MM cell lines are among the most sensitive to *SF3B1* depletion based on cell line rank (#1 = most sensitive, with lowest average CERES score; #27 = least sensitive, with highest average CERES score). Red line indicates cutoff (CERES score = -1) indicative of an essential gene. **D.** Aggregated DepMap ranking of cancer cell lines across all genes comprising the 20S proteasome, indicating increased but not maximal sensitivity of MM lines to genetic proteasome subunit ablation. **E.** Cytotoxicity (by CellTiterGlo) of indisulam versus a panel of MM cell lines (48 hr treatment; *n*=4 per data point +/- S.D.). **F.** DepMap dependency data (as in **D.**) for RBM39. **G.** Progression-free and overall survival data from the CoMMpass study (version IA11) with respect to top and bottom quartiles of *SRSF1* and *SF3B1* gene expression in newly-diagnosed MM patient tumor cells. *p*-values by Log-Ranked test.

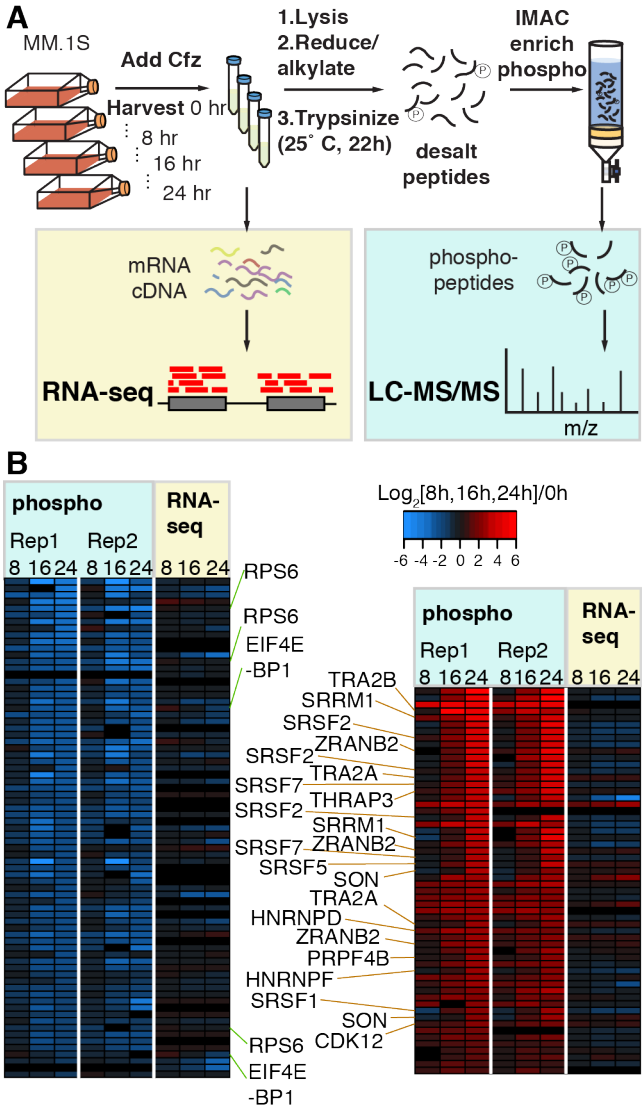


**Figure 1. Unbiased phosphoproteomic timecourse analysis of MM.1S cells treated with the PI carfilzomib (Cfz).**

bioRxiv preprint doi: https://doi.org/10.1101/508549; this version posted December 30, 2018. The copyright holder for this preprint (which was not certified by peer review) is the author/funder. All rights reserved. No reuse allowed without permission.

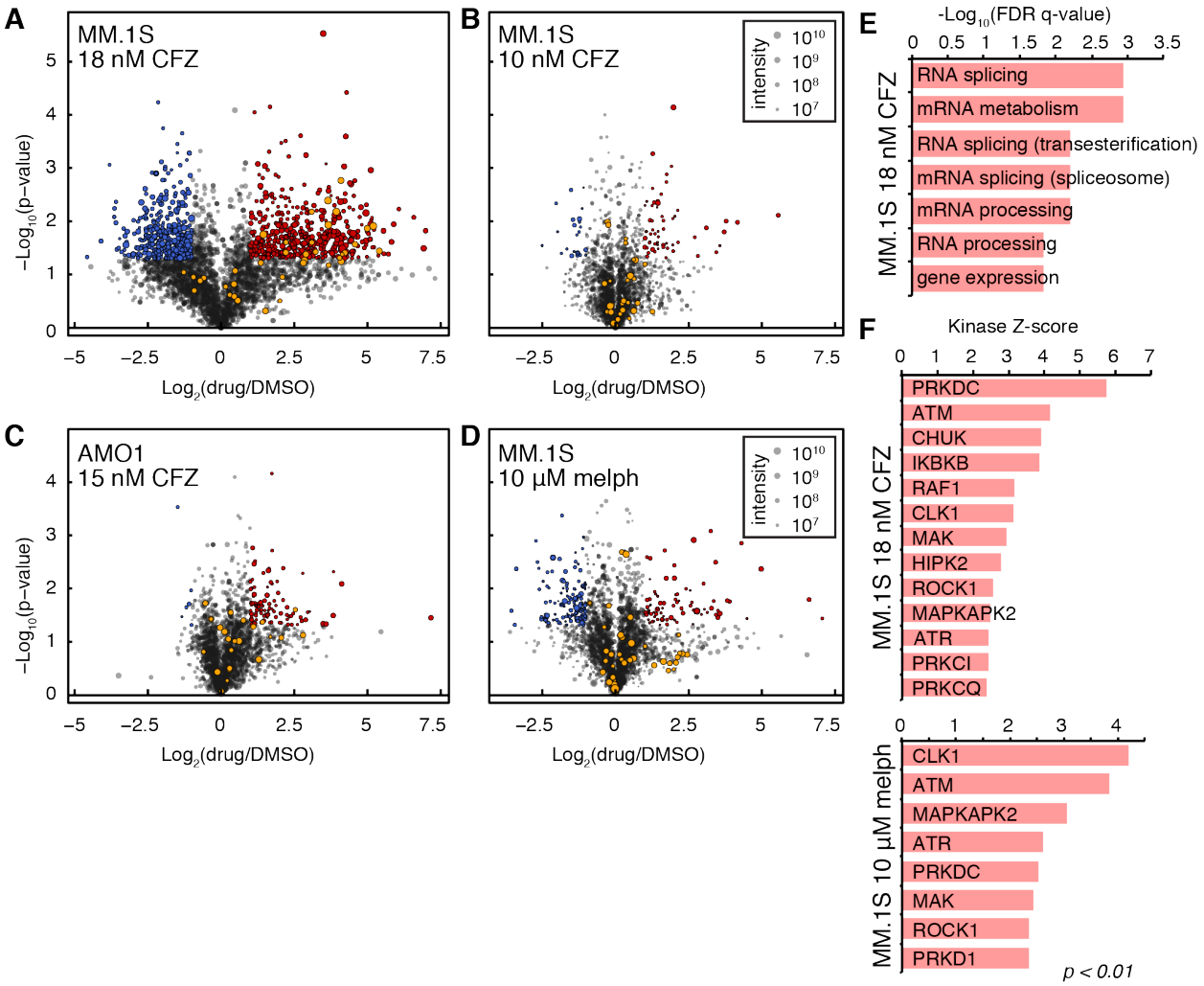


**Figure 2. Cfz induces phosphorylation of splicing factors in a dose-responsive manner.**

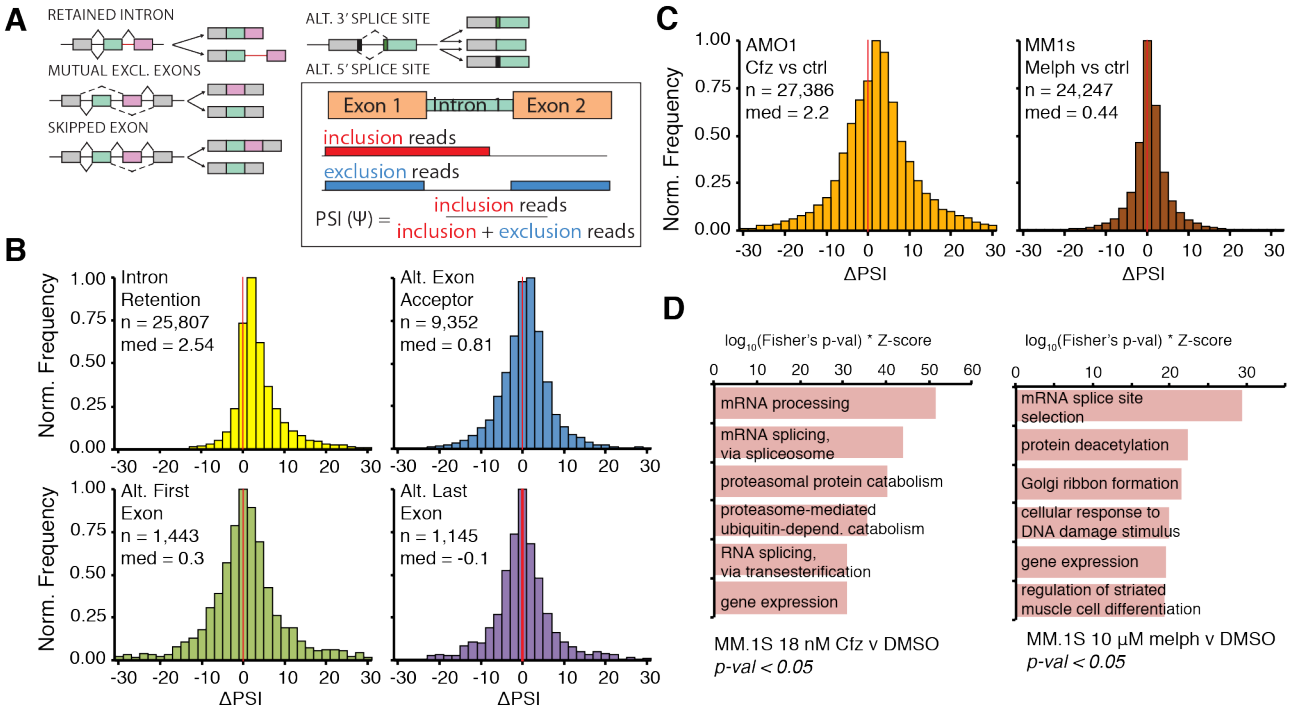


**Figure 3. Cfz treatment leads to prominent intron retention.**

bioRxiv preprint doi: https://doi.org/10.1101/508549; this version posted December 30, 2018. The copyright holder for this preprint (which was not certified by peer review) is the author/funder. All rights reserved. No reuse allowed without permission.

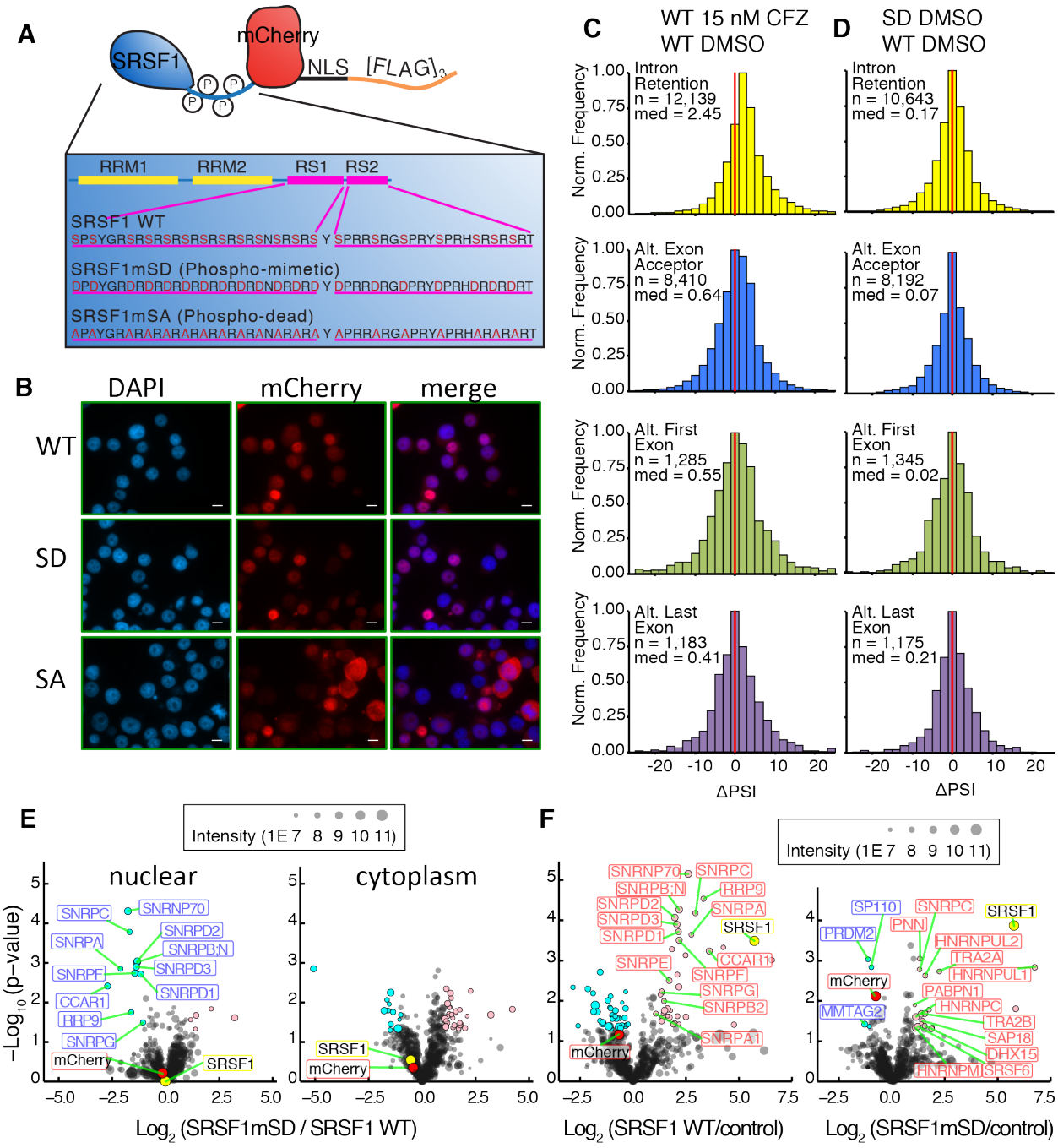


**Figure 4. Modeling SRSF1 phosphorylation in MM drives interactome dynamics but not global splicing changes.**

bioRxiv preprint doi: https://doi.org/10.1101/508549; this version posted December 30, 2018. The copyright holder for this preprint (which was not certified by peer review) is the author/funder. All rights reserved. No reuse allowed without permission.

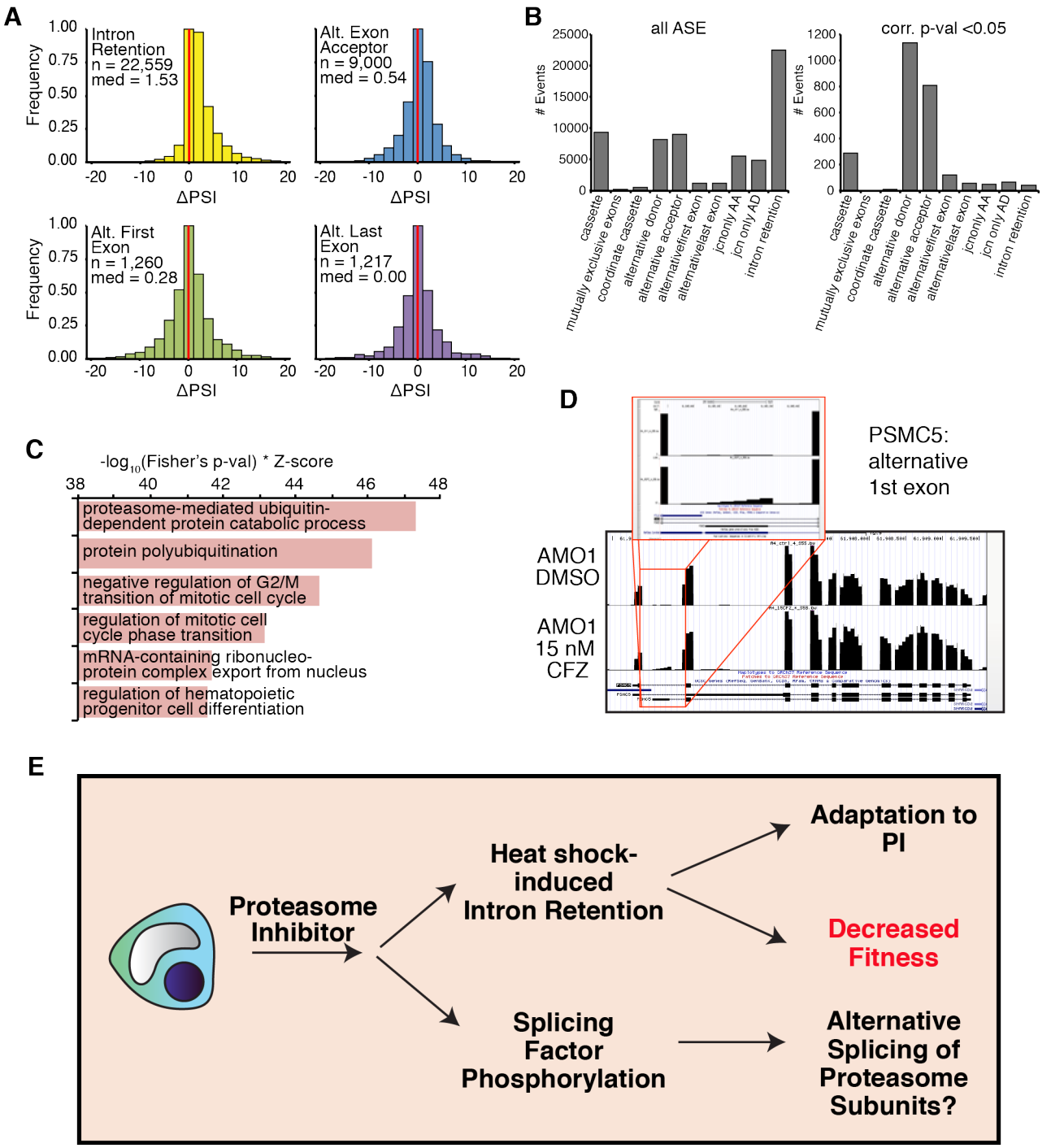


**Figure 5. Combined SRSF1 constructs validate the IR phenotype after Cfz.**

bioRxiv preprint doi: https://doi.org/10.1101/508549; this version posted December 30, 2018. The copyright holder for this preprint (which was not certified by peer review) is the author/funder. All rights reserved. No reuse allowed without permission.

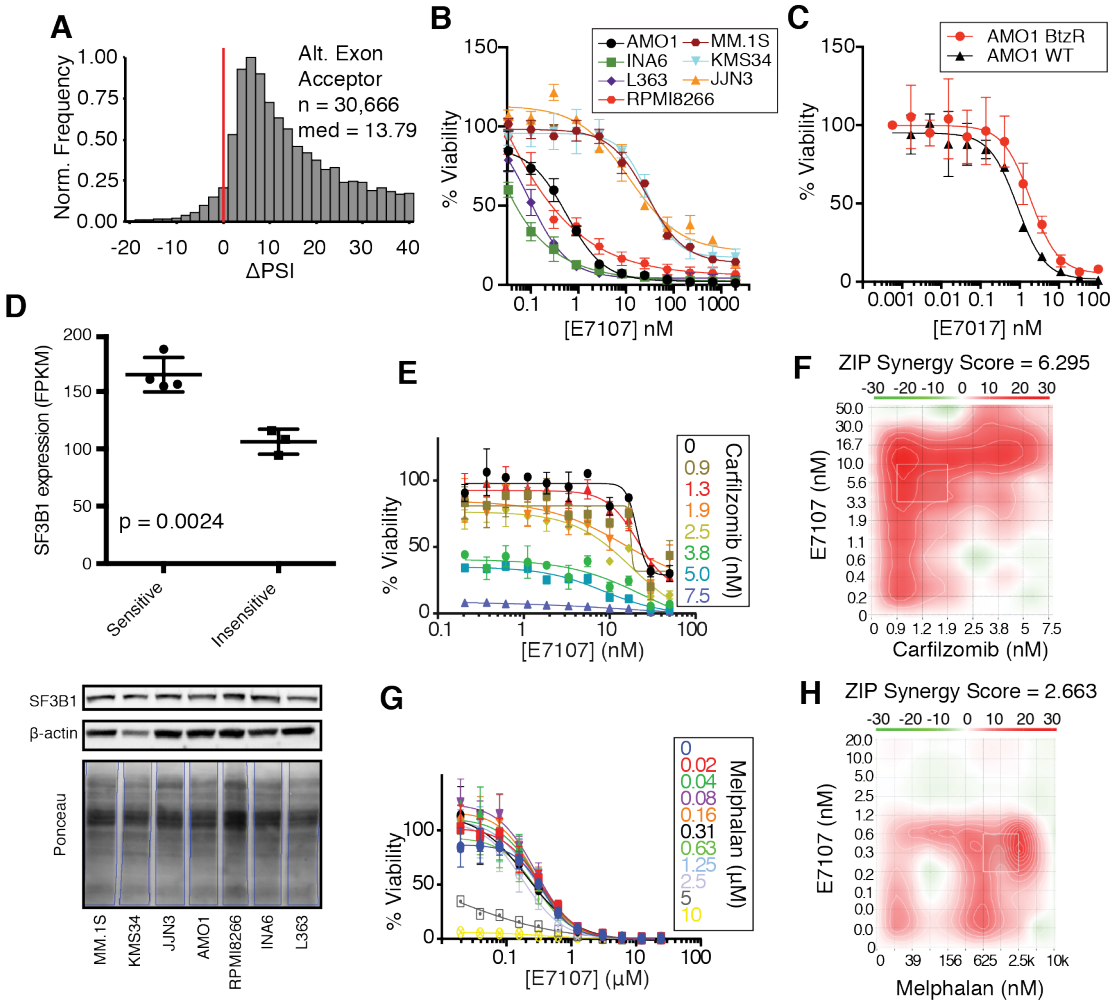


**Figure 6. The catalytic spliceosome inhibitor E7107 induces IR and has potent anti-MM activity *in vitro*.**

bioRxiv preprint doi: https://doi.org/10.1101/508549; this version posted December 30, 2018. The copyright holder for this preprint (which was not certified by peer review) is the author/funder. All rights reserved. No reuse allowed without permission.

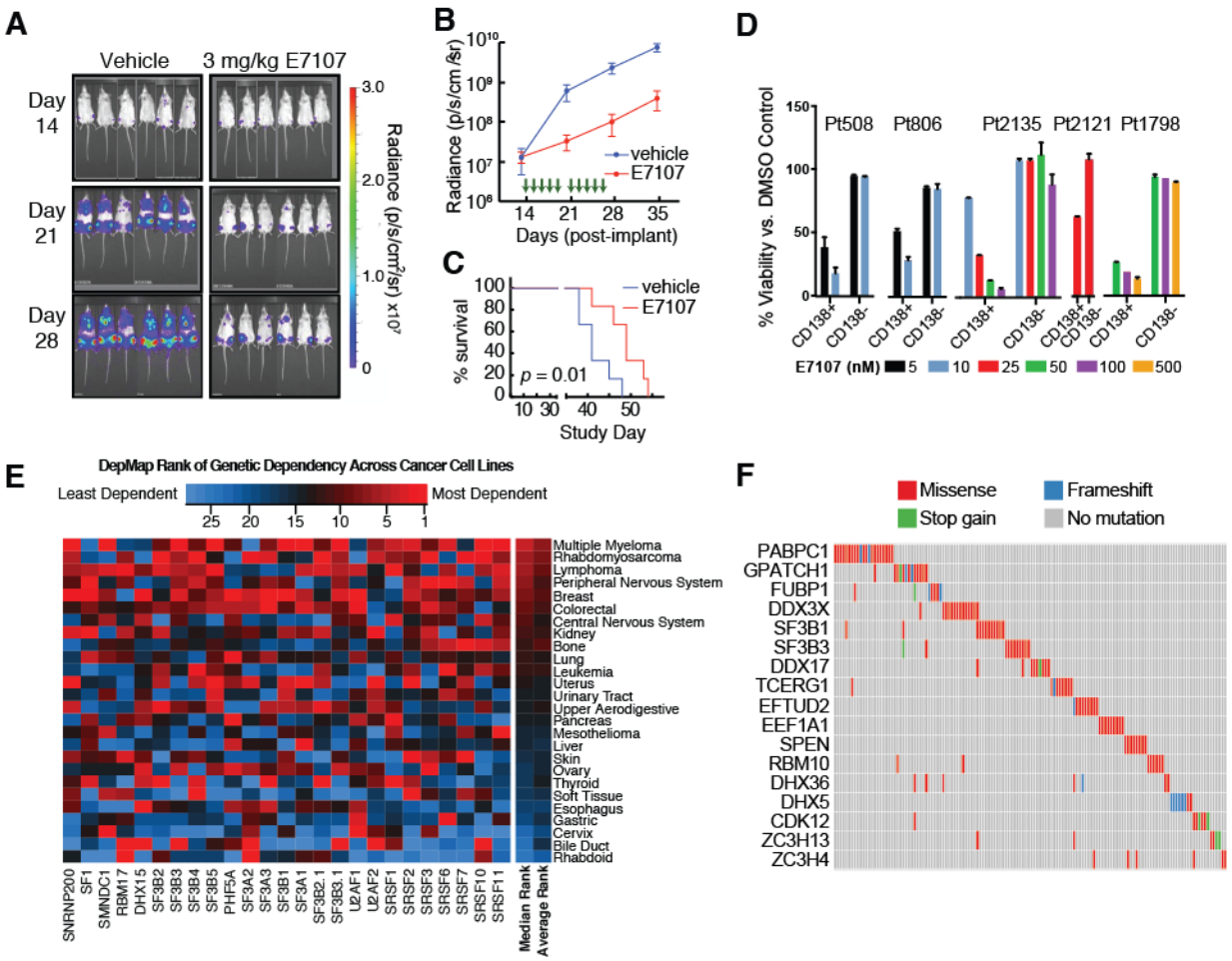


**Figure 7. Inhibition of the spliceosome is a promising therapeutic strategy in myeloma.**

bioRxiv preprint doi: https://doi.org/10.1101/508549; this version posted December 30, 2018. The copyright holder for this preprint (which was not certified by peer review) is the author/funder. All rights reserved. No reuse allowed without permission.

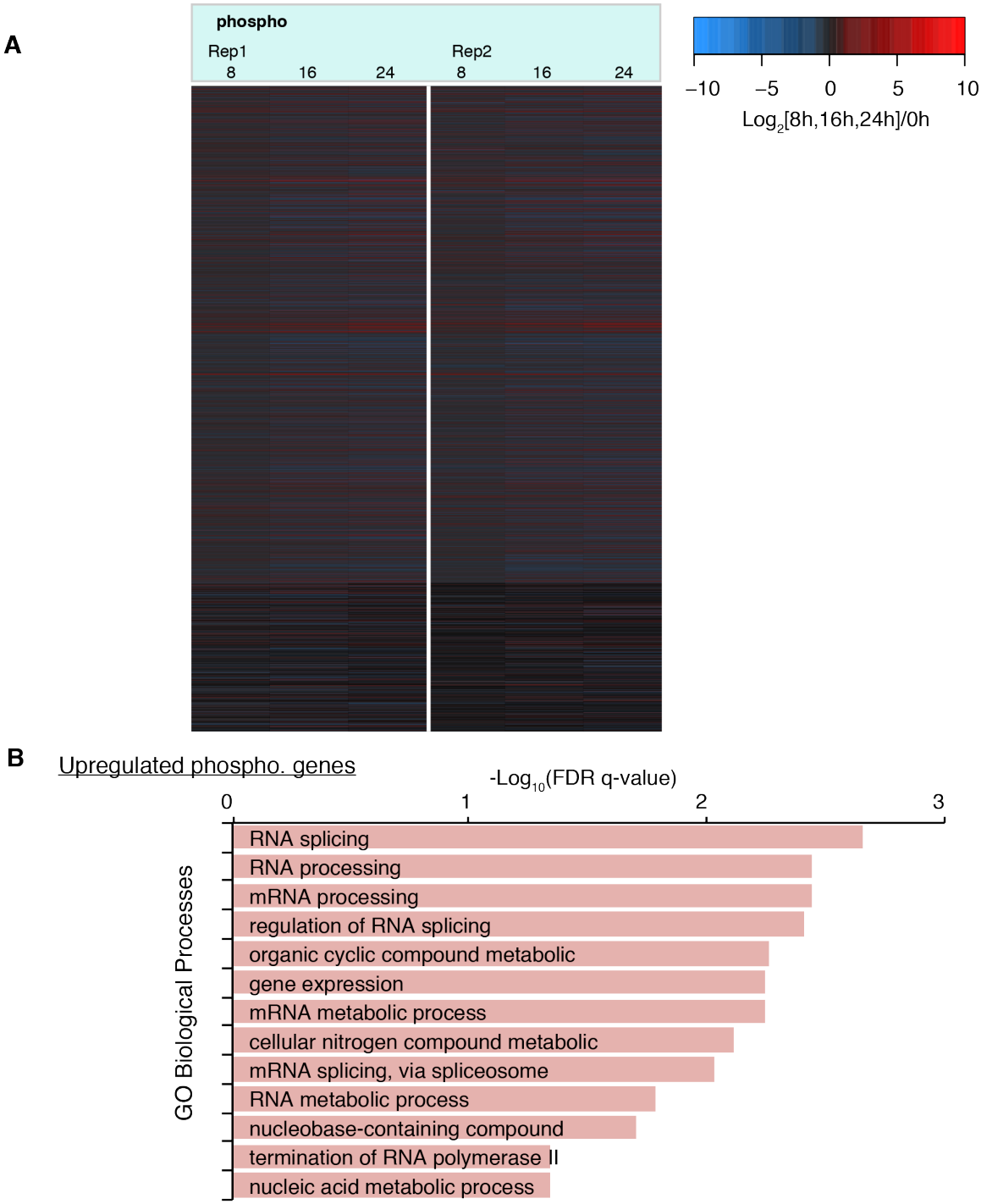


**Figure S1. Time-course of MM cell phosphorylation after Cfz treatment.**

bioRxiv preprint doi: https://doi.org/10.1101/508549; this version posted December 30, 2018. The copyright holder for this preprint (which was not certified by peer review) is the author/funder. All rights reserved. No reuse allowed without permission.

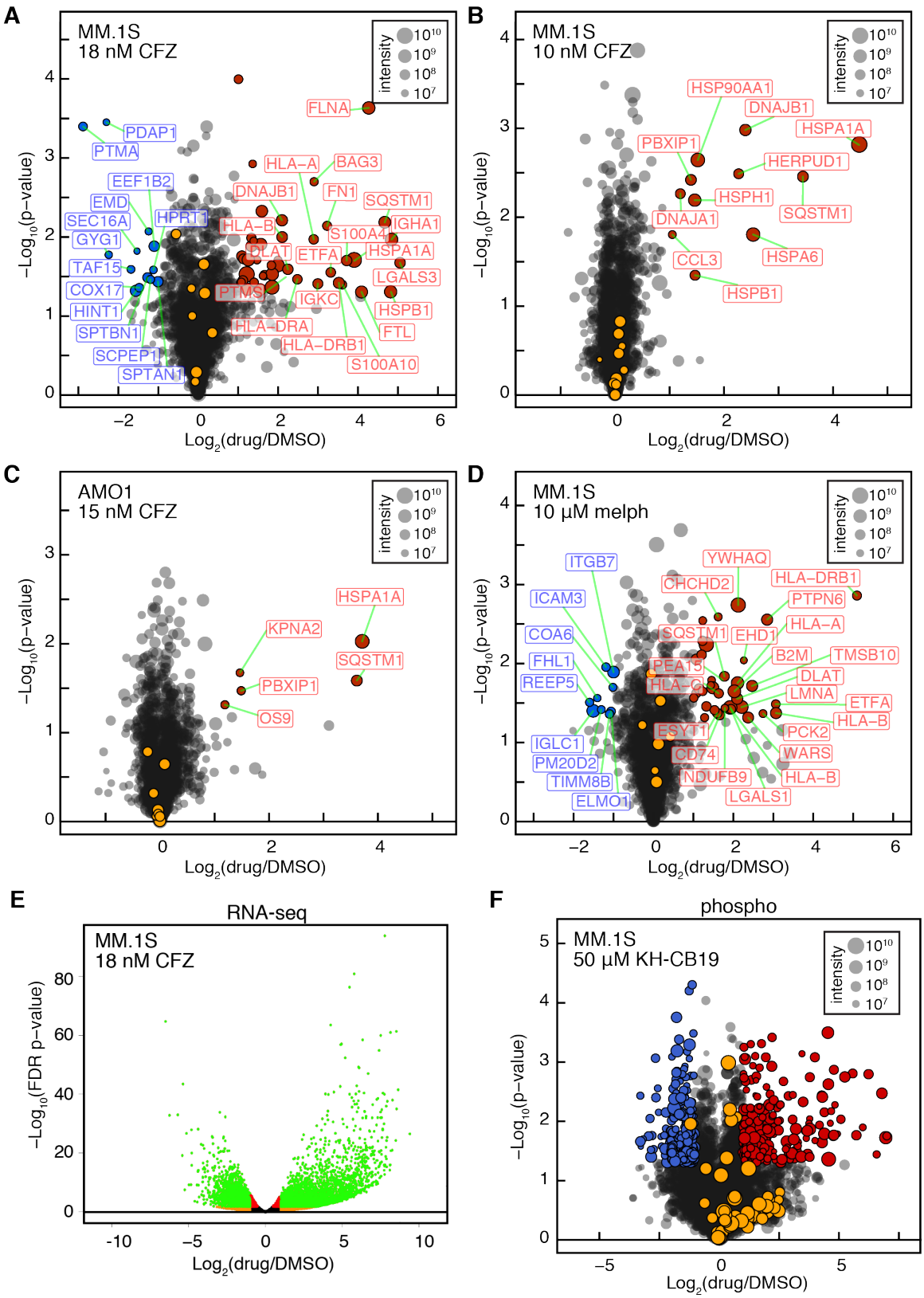


**Figure S2. Protein abundance and gene expression respone to drug perturbation.**

bioRxiv preprint doi: https://doi.org/10.1101/508549; this version posted December 30, 2018. The copyright holder for this preprint (which was not certified by peer review) is the author/funder. All rights reserved. No reuse allowed without permission.

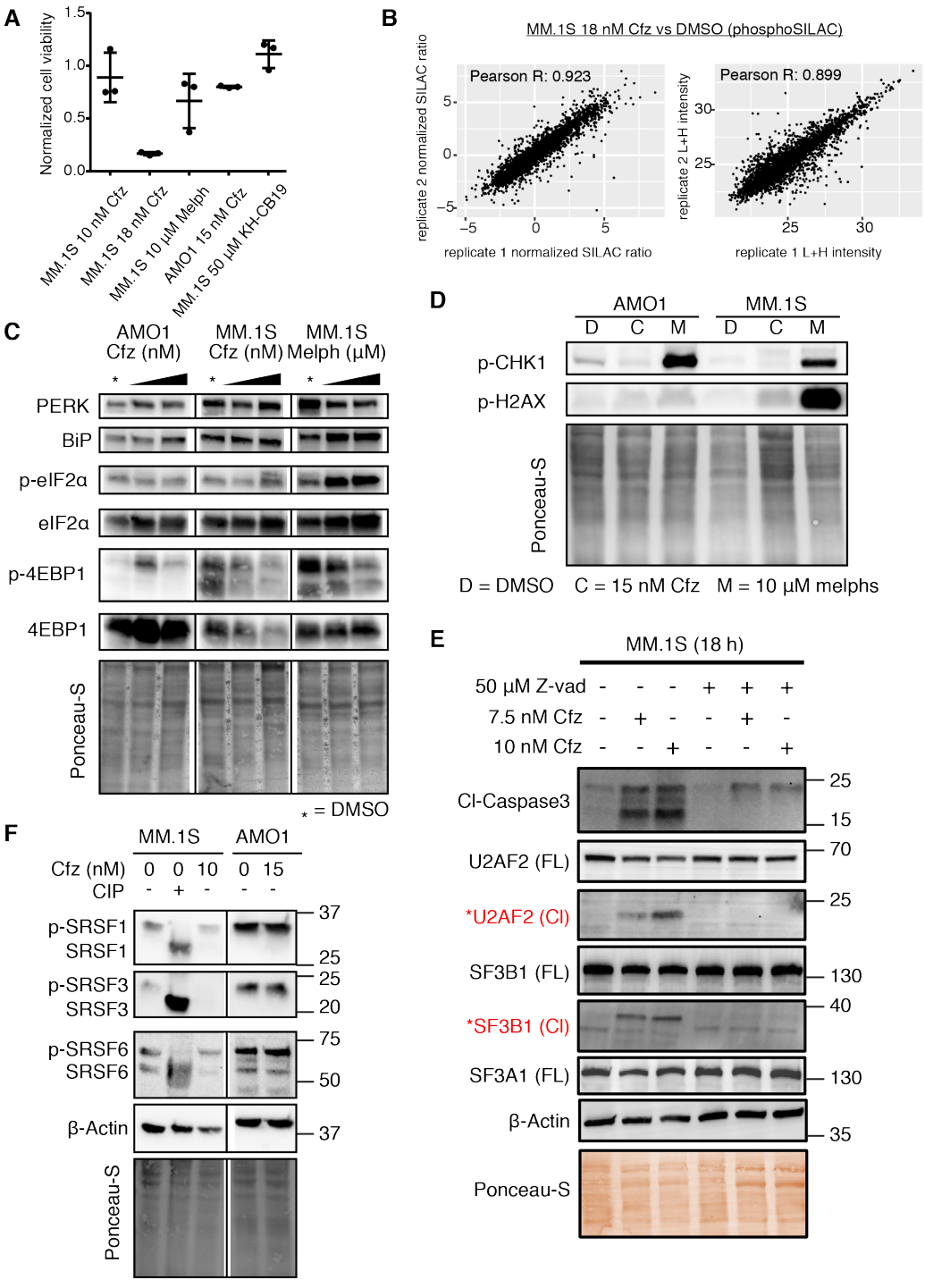


**Figure S3. Characterization of myeloma response to Cfz and melphalan.**

bioRxiv preprint doi: https://doi.org/10.1101/508549; this version posted December 30, 2018. The copyright holder for this preprint (which was not certified by peer review) is the author/funder. All rights reserved. No reuse allowed without permission.

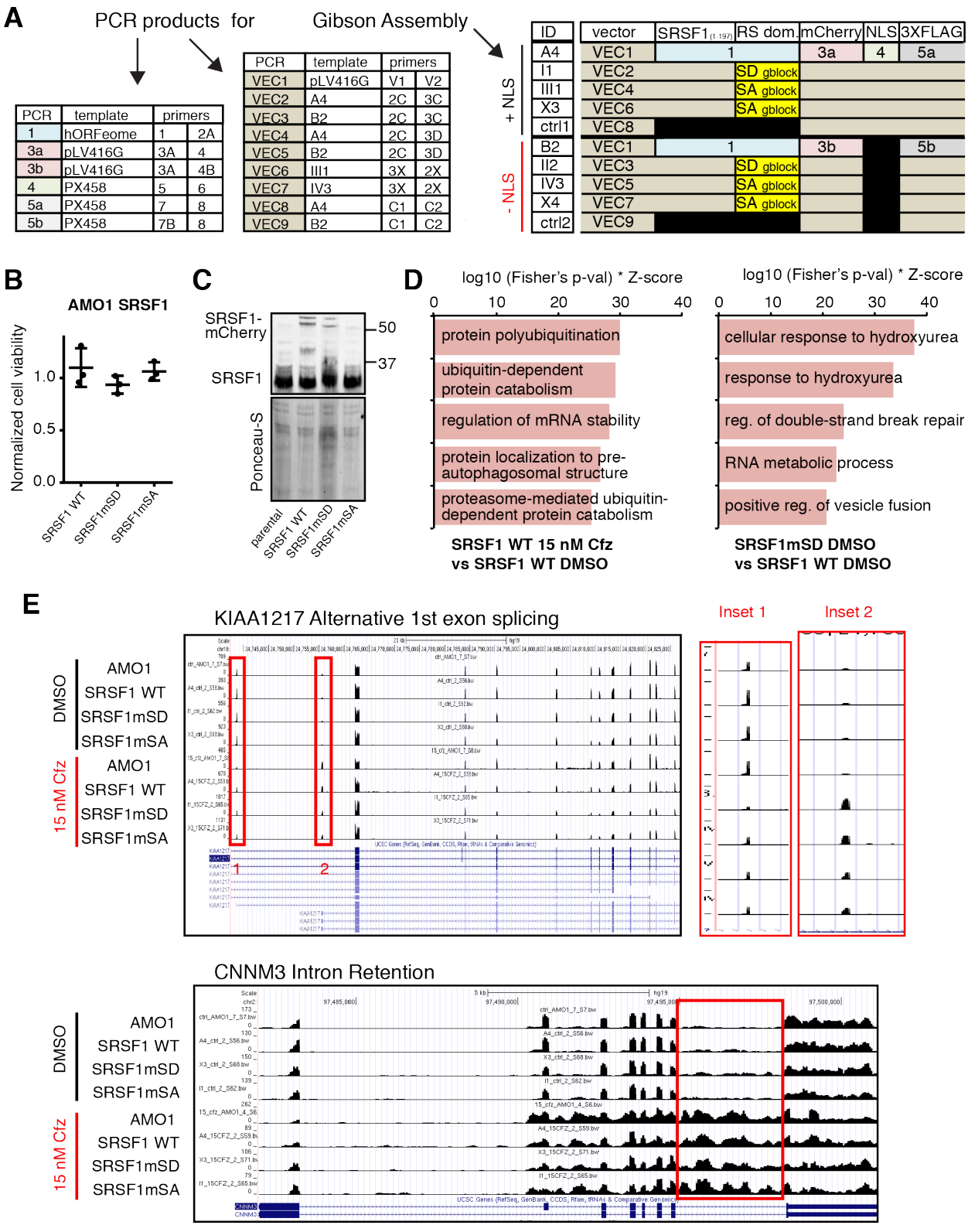


**Figure S4. Cfz-induced splicing alterations across SRSF constructs.**

bioRxiv preprint doi: https://doi.org/10.1101/508549; this version posted December 30, 2018. The copyright holder for this preprint (which was not certified by peer review) is the author/funder. All rights reserved. No reuse allowed without permission.

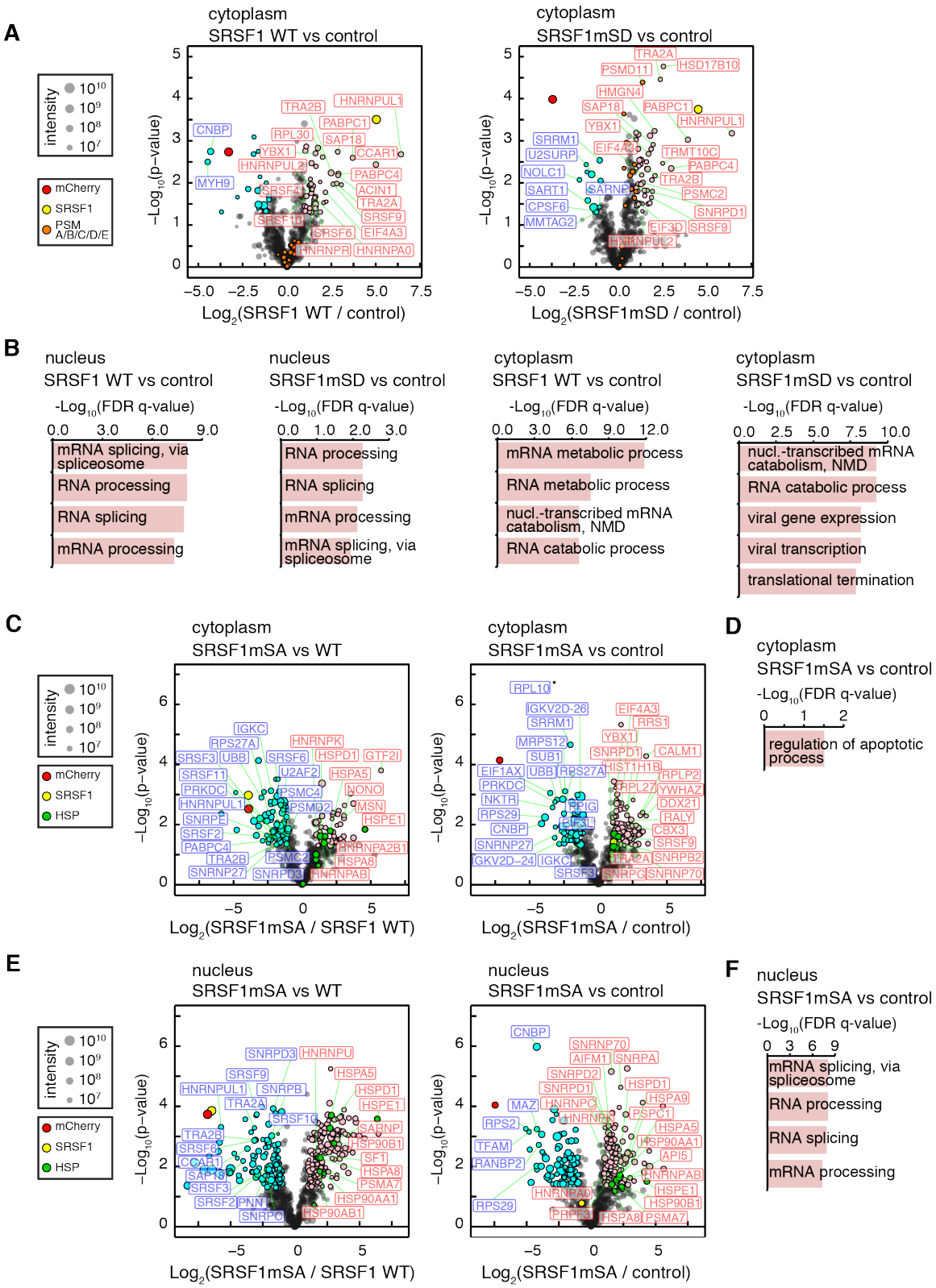


**Figure S5. The phosphorylation-dependent interactome of SRSF1.**

bioRxiv preprint doi: https://doi.org/10.1101/508549; this version posted December 30, 2018. The copyright holder for this preprint (which was not certified by peer review) is the author/funder. All rights reserved. No reuse allowed without permission.

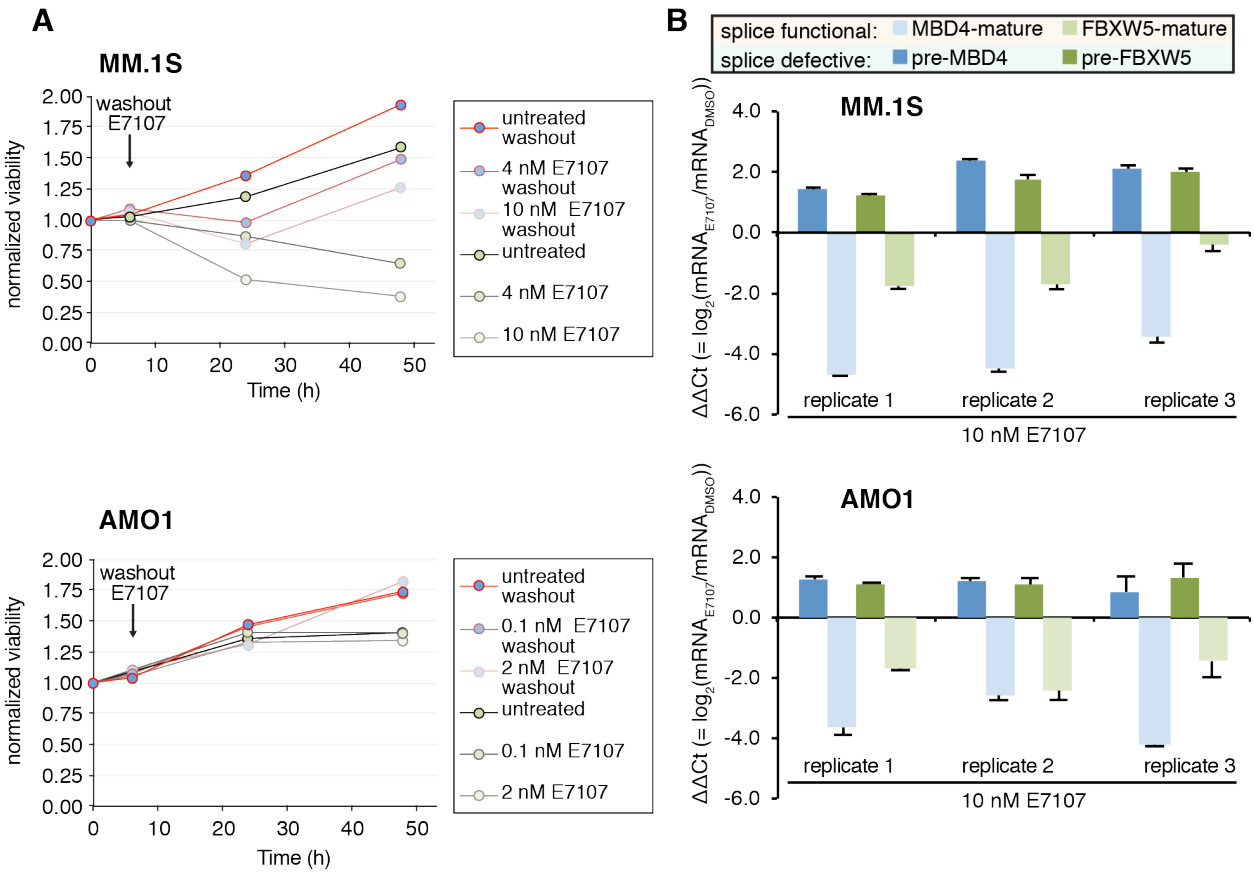


**Figure S6. E7107 cell toxicity and functional splicing assay.**

bioRxiv preprint doi: https://doi.org/10.1101/508549; this version posted December 30, 2018. The copyright holder for this preprint (which was not certified by peer review) is the author/funder. All rights reserved. No reuse allowed without permission.

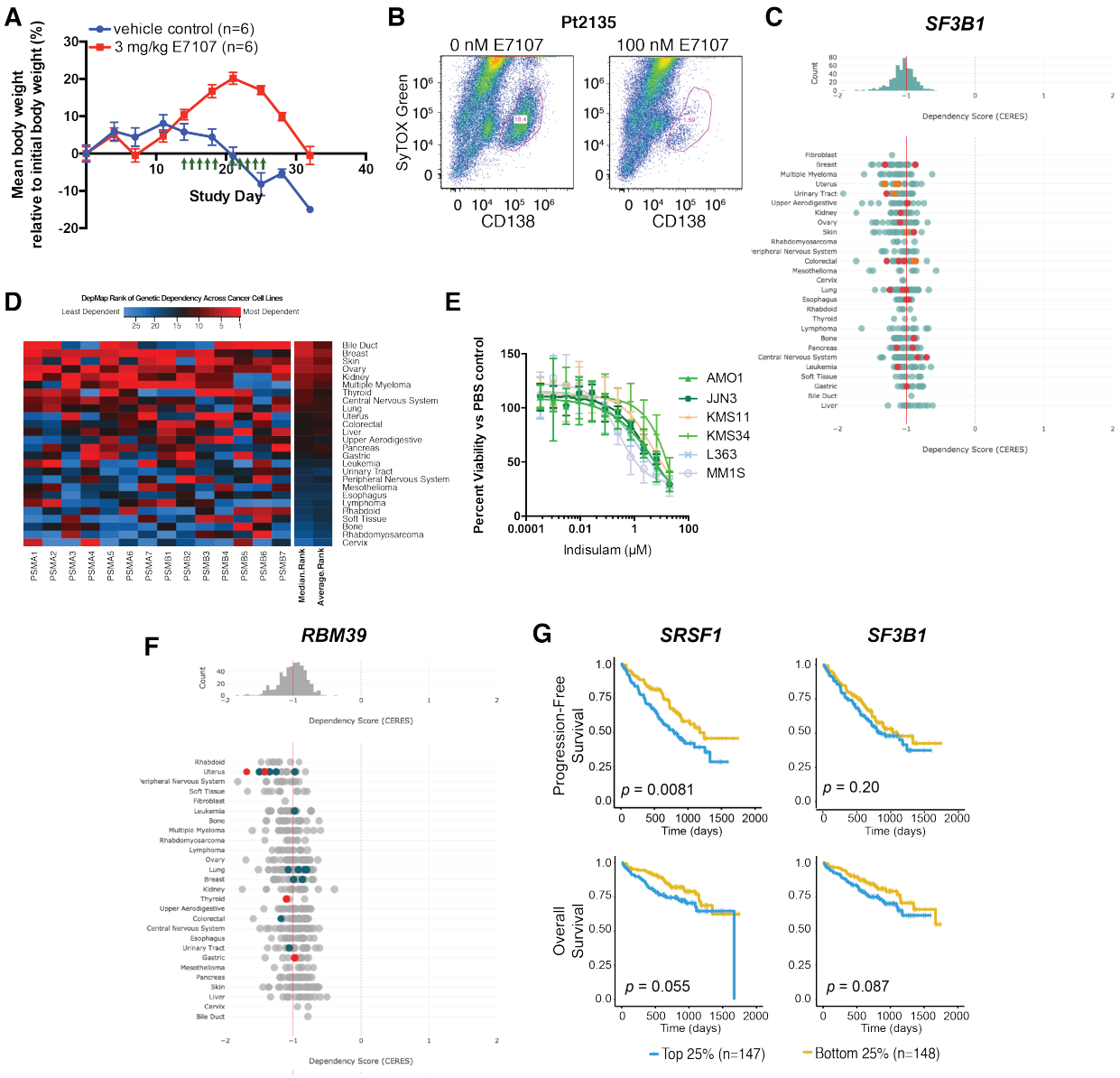


**Figure S7. Preclinical and clinical relevance of targeting the spliceosome in myeloma.**

**Table S1: Oligo sequences for cloning, qPCR, and RNA-seq cDNA library.**

| | oligo ID | sequence | target gene | vendor |
|---|---|---|---|---|
| | | | | |
| CLONING | V1 | AAGATGGCCTAGTAGACCCAGCTTTCTTGTACAAAGTGG | pLV416G | sigma |
| | V2 | CCCGACATAGCAGCCTGCTTTTTTGTACAA | pLV416G | sigma |
| | 1 | GGCTGCTATGTCGGGAGGTGGTGTGAT | SRSF1 | sigma |
| | 2A | CTGGTGCCTGTACGAGAGCGAGATCTGCTATGAC | SRSF1 | sigma |
| | 3A | TCGTACAGGCACCAGCGGTACCA | mCherry | sigma |
| | 4 | CGGCCTTTTCTTGTACAGCTCGTCCATGCC | mcherry | sigma |
| | 5 | TGTACAAGAAAAGGCCAGCGGCCAC | NLS | sigma |
| | 6 | CCTTATAGTCGCCGAATTCCTTTTTCTTTTTTGCCT | NLS | sigma |
| | 7 | GAATTCGGCGACTATAAGGACCACGACGGAGACT | 3XFLAG | sigma |
| | 8 | GGTCTACTAGGCCATCTTATCGTCATCGTCTTTG | 3XFLAG | sigma |
| | 2C | CATCAACTTTAACCCGGATGTAGGC | SRSF1 | sigma |
| | 3C | TCGTACAGGCACCAGCGGTACCA | mCherry | sigma |
| | 3D | CCCGTACAATGGTGAGCAAGGGCGAGG | mCherry | sigma |
| | 4B | CCTTATAGTCCTTGTACAGCTCGTCCATGCC | mCherry | sigma |
| | 7B | GCTGTACAAGGACTATAAGGACCACGACGGAG | 3XFLAG | sigma |
| | 3X | GGCACCAGCGGTACAATGGTGAGCAAGGGCGAGGAGG | mCherry | sigma |
| | 2X | TGTACCGCTGGTGCCTGTACGGGCGCGGGCTCTG | SRSF1 | sigma |
| | C1 | AGGCTGCTATGGTGAGCAAGGGCGAG | pLV416G | sigma |
| | C2 | CTCACCATAGCAGCCTGCTTTTTTGTACAAACT | pLV416G | sigma |
| | SD gblock | ATCCGGGTTAAAGTTGATGGGCCCAGAGATCCAGATTATGGAAGAGATCGAGATCGAGATCGTGATCGTGATAGAGAT CGTGATAGAGATAACGATAGGGATCGCGATTACGATCCAAGGAGAGATAGAGGAGATCCACGCTATGATCCCCGTCATG ATAGAGATCGCGATCGTACAGGCACCAG | | IDT |
| | SA gblock | ATCCGGGTTAAAGTTGATGGGCCCAGAGCCCCAGCCTATGGAAGAGCCCGAGCCCGAGCCCGTGCCCGTGCCAGAGCCC GTGCCAGAGCCAACGCCAGGGCCCGCGCCTACGCTCCAAGGAGAGCCAGAGGAGCTCCACGCTATGCTCCCCGTCATGCC AGAGCCCGCGCCCGTACAATGGTGAG | | IDT |
| | | | | |
| qPCR | F1 | CACACCAGATCGGCATCAA | FBXW5 mature | sigma |
| | F2 | CGATGATGTGTCCGTGTATGT | FBXW5 mature | sigma |

| | | | | |
|---|---|---|---|---|
| | F3 | AGACACCACTGAGGTAGGAA | FBXW5 unspliced | sigma |
| | F4 | TGGCAGGATCTGCTTGATG | FBXW5 unspliced | sigma |
| | M1 | GGAAGCTTCTCATCGCTACTAT | MBD4 | sigma |
| | M2 | GTTCTGACACATCTCTCCAGTC | MBD4 mature | sigma |
| | M3 | CCCTACCACACTGTCTCTACTA | MBD4 unspliced | sigma |
| | PP1 | AGACAAGGTCCCAAAGAC | PPIA | sigma |
| | PP2 | ACCACCCTGACACATAAA | PPIA | sigma |
| | | | | |
| TruSeq adapters | Univ. Adapt. (P5) | AATGATACGGCGACCACCGAGATCTACACTCTTTCCCTACACGACGCTCTTCCGATC*T | [* = phosphorothioate] | sigma |
| P7 (barcode sequence underlined) | Index 1 | GATCGGAAGAGCACACGTCTGAACTCCAGTCAC<u>ATCACG</u>ATCTCGTATGCCGTCTTCTGCTTG | | sigma |
| | Index 2 | GATCGGAAGAGCACACGTCTGAACTCCAGTCAC<u>CGATGT</u>ATCTCGTATGCCGTCTTCTGCTTG | | sigma |
| | Index 3 | GATCGGAAGAGCACACGTCTGAACTCCAGTCAC<u>TTAGGC</u>ATCTCGTATGCCGTCTTCTGCTTG | | sigma |
| | Index 4 | GATCGGAAGAGCACACGTCTGAACTCCAGTCAC<u>TGACCA</u>ATCTCGTATGCCGTCTTCTGCTTG | | sigma |
| | Index 5 | GATCGGAAGAGCACACGTCTGAACTCCAGTCAC<u>ACAGTG</u>ATCTCGTATGCCGTCTTCTGCTTG | | sigma |
| | Index 6 | GATCGGAAGAGCACACGTCTGAACTCCAGTCAC<u>GCCAAT</u>ATCTCGTATGCCGTCTTCTGCTTG | | sigma |
| | Index 7 | GATCGGAAGAGCACACGTCTGAACTCCAGTCAC<u>CAGATC</u>ATCTCGTATGCCGTCTTCTGCTTG | | sigma |
| | Index 8 | GATCGGAAGAGCACACGTCTGAACTCCAGTCAC<u>ACTTGA</u>ATCTCGTATGCCGTCTTCTGCTTG | | sigma |
| | Index 9 | GATCGGAAGAGCACACGTCTGAACTCCAGTCAC<u>GATCAG</u>ATCTCGTATGCCGTCTTCTGCTTG | | sigma |
| | Index 10 | GATCGGAAGAGCACACGTCTGAACTCCAGTCAC<u>TAGCTT</u>ATCTCGTATGCCGTCTTCTGCTTG | | sigma |
| | Index 11 | GATCGGAAGAGCACACGTCTGAACTCCAGTCAC<u>GGCTAC</u>ATCTCGTATGCCGTCTTCTGCTTG | | sigma |
| | Index 12 | GATCGGAAGAGCACACGTCTGAACTCCAGTCAC<u>CTTGTA</u>ATCTCGTATGCCGTCTTCTGCTTG | | sigma |
| | Index 13 | GATCGGAAGAGCACACGTCTGAACTCCAGTCAC<u>AGTCAA</u>ATCTCGTATGCCGTCTTCTGCTTG | | sigma |
| | Index 14 | GATCGGAAGAGCACACGTCTGAACTCCAGTCAC<u>AGTTCC</u>ATCTCGTATGCCGTCTTCTGCTTG | | sigma |
| | Index 15 | GATCGGAAGAGCACACGTCTGAACTCCAGTCAC<u>ATGTCA</u>ATCTCGTATGCCGTCTTCTGCTTG | | sigma |
| | Index 16 | GATCGGAAGAGCACACGTCTGAACTCCAGTCAC<u>CCGTCC</u>ATCTCGTATGCCGTCTTCTGCTTG | | sigma |
| | Index 18 | GATCGGAAGAGCACACGTCTGAACTCCAGTCAC<u>GTCCGC</u>ATCTCGTATGCCGTCTTCTGCTTG | | sigma |
| | Index 19 | GATCGGAAGAGCACACGTCTGAACTCCAGTCAC<u>GTGAAA</u>ATCTCGTATGCCGTCTTCTGCTTG | | sigma |

**Table S2. Genetic constructs.**

| ID | Name | Features | Promoter | Details |
|---|---|---|---|---|
| | | | | |
| **A4** | SRSF1 WT | SRSF1-mCherry-NLS-3XFLAG | EF1α | human SRSF1 was obtained from hORFeome v8.1; plasmid backbone was amplified by PCR from pLV416G-f-luc/mCherry lentiviral vector used for constitutive expression of luciferase in mouse models |
| **I1** | SRSF1mSD | SRSF1(1-197)-all RS domain S--> D substitution-mCherry-NLS-3XFLAG | EF1α | templated from A4 construct |
| **X3** | SRSF1mSA | SRSF1(1-197)-all RS domain S--> A substitution-mCherry-NLS-3XFLAG | EF1α | templated from III1 construct, which was initial SRSF1mSA construct with shortened mCherry linker |
| **ctrl1** | ctrl1 | mCherry-NLS-3XFLAG | EF1α | templated from A4 construct |
| **B2** | SRSF1 WT no NLS | SRSF1-mCherry-3XFLAG | EF1α | human SRSF1 was obtained from hORFeome v8.1; plasmid backbone was amplified by PCR from pLV416G-f-luc/mCherry lentiviral vector used for constitutive expression of luciferase in mouse models |
| **II2** | SRSF1mSD no NLS | SRSF1(1-197)-all RS domain S-->D substitution-mCherry-3XFLAG | EF1α | templated from B2 construct |
| **X4** | SRSF1mSA no NLS | SRSF1(1-197)-all RS domain S--> substitution-mCherry-3XFLAG | EF1α | templated from IV3 construct, which was initial SRSF1mSA no NLS construct with erroneous short mCherry linker |
| **ctrl2** | ctrl2 | mCherry-3XFLAG | EF1α | templated from B2 construct |

**Table S3. JuncBASE statistics.**

| Condition | event_type | total events | significant events (raw_pval <0.05) | significant events (raw_pval<0.05) & \|deltaPSI\| >10 | median deltaPSI total | median deltaPSI significant (raw_pval < 0.05) | Mode_total (bin size = 2) | Mode_significant (raw_pval < 0.05, bin size = 2) |
|---|---|---|---|---|---|---|---|---|
| MM.1S 18 nM Cfz vs. MM.1S DMSO (related to **Fig. 3B)** | cassette | 11125 | 640 | 254 | 0.29 | 2.895 | 2 | 6 |
| | mutually_exclusive | 68 | 2 | 1 | -2.355 | -12.915 | -6 | -20;6 |
| | coord_cassette | 1164 | 43 | 23 | 0.54 | 5.56 | 2 | 16 |
| | alternative_donor | 9188 | 635 | 215 | 1.64 | 3.41 | 2 | 4 |
| | alternative_acceptor | 9352 | 630 | 167 | 0.81 | 3.035 | 2 | 2 |
| | alternative_first_exon | 1443 | 100 | 50 | 0.3 | 2.71 | 0 | 2; 6 |
| | alternative_last_exon | 1145 | 73 | 32 | -0.1 | 1.9 | 0 | 6 |
| | jcn_only_AA | 6759 | 284 | 103 | 0 | 1.645 | 2 | 4 |
| | jcn_only_AD | 5595 | 277 | 129 | 0.09 | -1.31 | 2 | -8; 10 |
| | intron_retention | 25807 | 122 | 69 | 2.54 | 7.72 | 2 | 6 |
| | **All Types** | **71646** | **2806** | **1043** | **1.52** | **3.07** | **2** | **4** |
| MM.1S 10 uM melph vs. MM.1S DMSO (related to **Fig. 3C**) | cassette | 12267 | 472 | 187 | 1.06 | 5.035 | 2 | 4 |
| | mutually_exclusive | 84 | 2 | 1 | -1.455 | -8.39 | -2 | -22; 6 |
| | coord_cassette | 1417 | 53 | 23 | 1.75 | 6.52 | 2 | 4; 8 |
| | alternative_donor | 9535 | 331 | 91 | 0.37 | 2.33 | 0 | 2 |
| | alternative_acceptor | 10445 | 280 | 68 | 0.18 | 1.965 | 0 | 4 |
| | alternative_first_exon | 1561 | 85 | 37 | 0.37 | 2.41 | 0 | 6 |
| | alternative_last_exon | 1328 | 58 | 18 | -0.215 | 0.685 | 0 | -4 |
| | jcn_only_AA | 7667 | 240 | 87 | -0.13 | -2.48 | -2 | -4 |
| | jcn_only_AD | 6651 | 294 | 136 | -0.14 | -1.91 | -2 | -8 |
| | intron_retention | 24247 | 24 | 16 | 0.44 | -6.07 | 0 | -32; -28 |
| | **All Types** | **75202** | **1839** | **664** | **0.42** | **2.87** | **0** | **4** |
| AMO-1 15 nM Cfz vs. AMO-1 DMSO (related **Fig. 3C**) | cassette | 11645 | 685 | 313 | -0.82 | -4.72 | -2 | -4 |
| | mutually_exclusive | 397 | 15 | 5 | -0.65 | -7.48 | -6 | -8; 6 |
| | coord_cassette | 1673 | 58 | 33 | -1.37 | -5.41 | -4 | 6 |

| | | | | | | | | |
|---|---|---|---|---|---|---|---|---|
| | alternative_donor | 8116 | 358 | 147 | 0.605 | 3.83 | 2 | 4 |
| | alternative_acceptor | 9620 | 385 | 128 | 0.4 | 3.7 | 2 | 4 |
| | alternative_first_exon | 1241 | 90 | 53 | 0.13 | 2.465 | -2; 0 | 8 |
| | alternative_last_exon | 899 | 36 | 21 | 0.05 | 5.075 | 0 | 12 |
| | jcn_only_AA | 10700 | 368 | 165 | 0.2 | 3.185 | 2 | 6 |
| | jcn_only_AD | 9795 | 390 | 196 | 0.3 | -2.125 | 2 | 6 |
| | intron_retention | 27386 | 174 | 126 | 2.2 | 12.835 | 2 | 6 |
| | **All Types** | **81472** | **2559** | **1187** | **0.77** | **2.9** | **2** | **6** |
| MM.1S 10 nM E7107 vs. MM.1S DMSO (related to **Fig. 6A**) | cassette | 24053 | 11484 | 9945 | -16.6 | -31.66 | -6 | -8 |
| | mutually_exclusive | 91 | 21 | 16 | -0.5 | 5.64 | 0 | 6; 10 |
| | coord_cassette | 6137 | 2200 | 1904 | -13.34 | -34.09 | -4 | -6 |
| | alternative_donor | 7854 | 2502 | 1618 | 3.43 | 8.545 | 4 | 4 |
| | alternative_acceptor | 8493 | 2835 | 1846 | 3.09 | 7.59 | 4 | 6 |
| | alternative_first_exon | 1402 | 377 | 267 | -1.38 | -5.45 | -2 | -12 |
| | alternative_last_exon | 1088 | 356 | 245 | -3.705 | -9.8 | -2 | -8; -6 |
| | jcn_only_AA | 5495 | 792 | 463 | -0.02 | -2.24 | 2 | -6 |
| | jcn_only_AD | 4709 | 698 | 415 | 0.02 | 2.805 | 4 | 8 |
| | intron_retention | 30666 | 7171 | 6564 | 13.79 | 37.2 | 6 | 24 |
| | **All Types** | **89988** | **28436** | **23283** | **1.27** | **-8.685** | **4** | **-6** |
| SRSF1 WT 15 nM Cfz vs. SRSF1 WT DMSO (related to **Fig. 4C**) | cassette | 8337 | 539 | 215 | 0.48 | 2.56 | 2 | 10 |
| | mutually_exclusive | 147 | 3 | 1 | -0.42 | -2.9 | 2 | -20; -2 |
| | coord_cassette | 798 | 51 | 25 | 1.38 | 6.7 | 4 | 10 |
| | alternative_donor | 7639 | 343 | 98 | 0.83 | 3.74 | 2 | 10 |
| | alternative_acceptor | 8410 | 450 | 104 | 0.64 | 3.255 | 0 | 5 |
| | alternative_first_exon | 1285 | 112 | 63 | 0.55 | 5.11 | 0 | 10 |
| | alternative_last_exon | 1183 | 80 | 32 | 0.41 | 4.17 | 0 | 10 |
| | jcn_only_AA | 7030 | 318 | 112 | 0.035 | -0.845 | -2 | -25 |
| | jcn_only_AD | 6257 | 371 | 160 | 0.32 | 3.06 | 2 | 10 |
| | intron_retention | 12139 | 60 | 36 | 2.45 | 7.865 | 2 | 10 |

| | | | | | | | | |
|---|---|---|---|---|---|---|---|---|
| | **All Types** | **53225** | **2327** | **846** | **1.09** | **3.24** | **2** | **4** |
| SRSF1mSD DMSO vs. SRSF1 WT DMSO (related to **Fig. 4D**) | cassette | 8425 | 335 | 94 | 0.09 | 1.79 | 0 | 4 |
| | mutually_exclusive | 184 | 4 | 0 | 0.025 | 1.025 | 4 | -2 |
| | coord_cassette | 810 | 39 | 22 | 0.12 | 2.83 | -2 | 4 |
| | alternative_donor | 7204 | 217 | 45 | 0.05 | -0.28 | 0 | 2 |
| | alternative_acceptor | 8192 | 209 | 43 | 0.07 | 1.37 | 0 | 4 |
| | alternative_first_exon | 1345 | 60 | 20 | 0.02 | 0.995 | 0 | -6 |
| | alternative_last_exon | 1175 | 38 | 11 | 0.21 | 2.98 | 0 | 6 |
| | jcn_only_AA | 7139 | 234 | 100 | 0 | 1.66 | 0 | -4 |
| | jcn_only_AD | 6247 | 237 | 98 | 0 | 1.95 | 2 | 4 |
| | intron_retention | 10643 | 33 | 19 | 0.17 | -12.5 | 0 | -10 |
| | **All Types** | **51364** | **1406** | **452** | **0.08** | **1.1** | **0** | **4** |
| **Conditions** | event_type | **total events** | **significant events (corrected_pval <0.05)** | **significant events (corrected_pval < 0.05) & \|deltaPSI\| >10** | **median deltaPSI total** | **median deltaPSI significant (corrected_pval < 0.05)** | **Mode_total (bin size = 2)** | **Mode_significant (corrected_pval < 0.05, bin size = 2)** |
| AMO-1 (all: parental, WT, SD, SA) 15 nM Cfz vs. AMO-1 (all) DMSO (related to **Fig. 5A**) | cassette | 9401 | 286 | 115 | 0.08 | -3.49 | 0 | 5 |
| | mutually_exclusive | 47 | 0 | 0 | 0.42 | NA | 0 | 0 |
| | coord_cassette | 562 | 6 | 3 | 0.425 | 8.775 | 0 | 5 |
| | alternative_donor | 8147 | 1134 | 139 | 0.68 | 1.83 | 0 | 10 |
| | alternative_acceptor | 9000 | 810 | 114 | 0.54 | 1.635 | 0 | 10 |
| | alternative_first_exon | 1260 | 119 | 58 | 0.28 | 3.69 | 0 | 10 |
| | alternative_last_exon | 1217 | 61 | 21 | 0 | 1.24 | 0 | 5 |
| | jcn_only_AA | 5482 | 48 | 21 | 0 | 1.705 | 0 | -5 |
| | jcn_only_AD | 4799 | 68 | 24 | 0.07 | -1.95 | 0 | 5 |
| | intron_retention | 22559 | 43 | 25 | 1.53 | 10.8 | 0 | 10 |
| | **All Types** | **62474** | **2575** | **520** | **0.84** | **1.76** | **0** | **2** |

bioRxiv preprint doi: https://doi.org/10.1101/508549; this version posted December 30, 2018. The copyright holder for this preprint (which was not certified by peer review) is the author/funder. All rights reserved. No reuse allowed without permission.

## Methods

### CONTACT FOR REAGENT AND RESOURCE SHARING

Further information and requests for resources and reagents should be directed to and will be fulfilled by Arun Wiita (arun.wiita@ucsf.edu).

### Experimental Model and Subject Details

#### Mouse models

Mice used in mouse model studies were NOD.Cg-*Prkdc*$^{scid}$ *Il2rg*$^{tm1Wjl}$/SzJ (NSG) from The Jackson Laboratory. All the mice were female, 6-8 wks old at start of studies, and typically weigh 20-25 g. NSG mice are severely immunodeficient and were handled with aseptic techniques and housed in pathogen free environments at the UCSF Laboratory Animal Research Center. All mouse studies were performed according to UCSF Institutional Animal Care and Use Committee-approved protocols.

#### Human patient primary cell culture

De-identified primary multiple myeloma patient bone marrow (BM) samples were obtained from the UCSF Hematologic Malignancy Tissue Bank in accordance with the UCSF Committee on Human Research-approved protocols and the Declaration of Helsinki. Bone marrow mononuclear cells were isolated by density gradient centrifugation with Histopaque-1077 (Sigma Aldrich) at room temperature, 400 rcf for 30 min, then washed with 10 mL D-PBS 3 times by centrifugation at 400 rcf for 7 min. Mononuclear cells were resuspended in a small volume (~1.5 mL) of media (RPMI1640, 10% FBS, 1% penicillin/streptomycin, 2 mM glutamine) and incubated at 37°C, 5% $CO_2$ for 15min, immediately before E7107 treatment.

#### Cell culture

All cell lines were grown in suspension at 37°C, 5% $CO_2$ in RPMI 1640 medium (Gibco), supplemented with 10% fetal bovine serum (FBS, Atlanta Biologicals for proteomics experiments and Gemini for drug viability experiments) and 1% penicillin-streptomycin. Cell lines were seeded at 0.3-0.5E+6 cells/mL and passaged every 2-4 days when cells reach 1E+6 cells/mL density. INA6 cell media was supplemented with 90 ng/mL recombinant human IL-6 (ProSpec). All cell lines used are female, except INA6 and RPMI8266. All cell lines were validated using STR profiling service by ATCC.

### Method Details

#### Cell culture drug cytotoxicity assay

For dose-response cell toxicity assays in **Fig. 6**, 1E+3 myeloma cells were seeded per well in 384 well plates (Corning) using the Multidrop Combi (Thermo Fisher) and incubated for 24 hr.

bioRxiv preprint doi: https://doi.org/10.1101/508549; this version posted December 30, 2018. The copyright holder for this preprint (which was not certified by peer review) is the author/funder. All rights reserved. No reuse allowed without permission.

In the case of monotherapy cytotoxicity assays in **Fig. 6B-C and S7E**, cells were treated with drug or DMSO and incubated for 48 hr, while cells were further incubated with E7107 (H3) for an additional 24 hr in E7107 dual therapy combination assays in **Fig. 6E and G**. Carfilzomib (Cfz, Selleck), melphalan (melph, Sigma), and E7107 were solubilized in DMSO at 10 mM and stored in aliquots at -80° C, to minimize freeze-thaw degradation, and diluted in media when administered to cells.

For E7107 time-course "washout" experiment in **Fig. S6A**, cells are treated in 6-well plates at 1E+6 cells/mL with DMSO, 0.1 nM, 2 nM E7107 for AMO-1 and DMSO, 4 nM , and 10 nM E7107 for MM.1S . Cell viability was measured at 0 hr, 6 hr, 24 hr, and 48 hr, where media for "washout" samples were exchanged for fresh media, without E7107after the 6 hr measurement. All cell viability was determined with Cell-Titer Glo reagent (Promega) using a Glowmax Explorer (Promega) luminescence plate reader. For the drug titration cytotoxicity assays, measurements were performed in quadruplicate, while measurements were performed in triplicate in all other assays, and viabilities are reported as normalized to DMSO-treated controls or measurements at 0 hr. For ZIP synergy calculations in **Fig. 6F and H**, normalized viability data was submitted to SynergyFinder web application (Yadav et al, 2015).

For proteomic/phosphoproteomic/RNA-seq experiments, all experiments were performed at a starting cell density of 1E+6 cells/mL. For timecourse studies, ~20E+6 cells were grown in media or 15-20E+6 cells in SILAC media (RPMI 1640 without lysine or arginine, supplemented with 1% Pencillin/Streptomycin, 10% dialyzed FBS, and 321.6 μM L-Lysine or L-Lysine-$^{13}C_6$,$^{15}N_2$ (Cambridge Isotope) and 190.4 μM Arginine or L-Arginine-$^{13}C_6$,$^{15}N_4$ (Cambridge Isotope)) for single timepoint experiments and treated with either DMSO or drug compound (10 nM Cfz, 15nM Cfz, 18 nM Cfz, 10 μM melph, 50 μM KH-CB19 (Santa Cruz)). For SRSF1 AP-MS, 25-30E+6 cells were grown in label-free media (RPMI1640, 10% FBS) and treated with DMSO for 24 hr before harvest. Timecourse experiments were harvested at 0, 8, 16, and 24 hr while all other experiments were harvested after 24 hr. Cell viability measurements in **Fig. S3A and S4B** were performed with Cell-Titer Glo at 0 hr and 24 hr, and reported as the mean (± S.D.) ratio of luminescence intensities. The cells were harvested by centrifugation at 300 rcf for 5 min and washed with 5 mL PBS. 1-3E+6 cells were aliquoted for RNA-seq, and the remainder for proteomics. Cells were then pelleted by centrifugation, PBS was aspirated, and cell pellets were frozen in liquid nitrogen (LN2) and stored in -80°C. At least 2 biological replicates for each condition were gathered and analyzed (3 replicates for 10 nM carfilzomib and 50 μM KH-CB19).

**Cloning and lentiviral transduction**

bioRxiv preprint doi: https://doi.org/10.1101/508549; this version posted December 30, 2018. The copyright holder for this preprint (which was not certified by peer review) is the author/funder. All rights reserved. No reuse allowed without permission.

**Refer to Table S1** for primer sequences and **Table S2 and Fig. S4A** for construct details and assembly of lentiviral vectors encoding SRSF1-mCherry-(±NLS)-$[FLAG]_3$ and its RS domain mutants used in SRSF1 AP-MS experiments, microscopy experiments, and AMO-1 exogenous SRSF1 alternative splicing analysis. Plasmid encoding SRSF1 was isolated from Human ORFeome library v8.1 (Recombinant Antibody Network), and polymerase chain reaction (PCR) was used to amplify the gene from this plasmid, nucleoplasmin nuclear localization signal (NLS) and 3X FLAG sequences from PX458, and pLV lentiviral transfer plasmid backbone and mCherry from pLV-416G. Gibson assembly was used to combine SRSF1, mCherry, and 3X FLAG with the lentiviral vector backbone (excluding luciferase-T2A-mCherry genes) pLV-416G, with and without NLS. These lentiviral SRSF1 WT constructs, with and without NLS, are referred to internally as A4 and B2, respectively. SRSF1 mutant constructs were formed by PCR amplification of a truncated SRSF1 (1-197) in A4 and B2, and Gibson assembly with gBlock oligos (IDT), synthetically designed oligos substituting native codons for all Ser with codons for Asp or Ala, depending on it being a SD or SA mutant. SD constructs with and without NLS are referred to as I1 and II2, while SA constructs with and without NLS are referred to as III1 and IV3, respectively. However, SA gBlock design left a shortened linker region. This was corrected by further PCR amplification of III1 and IV3 templates with extended primers to create corrected SA construct with and without NLS, referred to as X3 and X4, respectively. AP-MS negative control of mCherry-(NLS)-$[FLAG]_3$, with and without NLS, referred to as ctrl1 and ctrl2, respectively, were constructed by PCR amplification of A4 and B2, respectively, with primers excluding SRSF1, and annealed by one fragment Gibson Assembly. Template vector is removed by DpnI nuclease treatment.

For each sample, 1.5 µg lentiviral-SRSF1 transfer plasmid was transfected along with 1.33 µg of the packaging plasmid pCMV-dR8.91 (containing Gag-Pol) and 0.17 µg of the VSV-G envelope expressing plasmid pMD2.G into Lenti-X (Takara) packaging cells (seeded the day before in 6-well plates with 0.6E+6 cells and 2.6 mL Opti-MEM (Life Tech) per well) with FuGene transfection reagent in 300 µl Opti-MEM (Life Tech), incubating for 30min, before adding to each well. After 2 days transfection, viral particles were harvested, and filtered with 0.45 µm filter and concentrated with 1 part viral titer and 3 part Lenti-X concentrator (Takara, ~9-10 mL total) by incubating at 4°C for more than 12 hr, then spinning at 1500 rcf for 45 min at 4°C. Supernatant is carefully aspirated and virus is resuspended in PBS. Entire viral titers were distributed between AMO-1 and MM.1S cells. ~0.75-1.5E+6 cells were seeded in each well of a 6-well plate with 1.5 mL normal growth media, with 8 ug/mL polybrene added (final concentration of 4 ug/mL) and 1mL of virus and 0.5 mL media, then mixed together. Cells were transduced by spinfection, spinning plates at 1000 rcf at 33°C for 2 hr. Afterwards, plates are stored in 37°C incubator (5% $CO_2$) for 2 days, before media is replaced. After a few passages, the cells

bioRxiv preprint doi: https://doi.org/10.1101/508549; this version posted December 30, 2018. The copyright holder for this preprint (which was not certified by peer review) is the author/funder. All rights reserved. No reuse allowed without permission.

positively transduced with exogenous SRSF1 constructs were selected with G418, for several passages and then sorted for mCherry fluorescence by Fluorescence Activated Cell Sorting (FACS, Sony SH800). Cells were maintained as all other MM cell lines.

**Global proteomic and phosphoproteomic preparation**

Frozen cell pellets of ~15-20E+6 cells were thawed (~7-8E+6 cells for each of the light (drugged) and heavy (DMSO) SILAC labeled samples), resuspended in 8M urea, 0.1 M Tris pH 8.0, 150 mM NaCl and 1X HALT phosphatase/protease inhibitor cocktail for timecourse experiments (**Fig. 1B, S1**) or 8 M Guanadine-Cl (Gdn), 0.1 M Tris pH 8.5, 10 mM tris(2-carboxyethyl)phosphine (TCEP), 40 mM 2-chloroacetamide (2-CAA), 1X HALT for SILAC samples (**Fig. 2 and S2A-D, F**) sonicated with probe sonicator (BRANSONIC) 3 X 10 s ON, 15 s OFF. Protein abundance was measured by bicinchoninic acid (BCA) assay. In the case of single-time point SILAC samples, equal part light and heavy labeled lysate samples were combined (~ 2.5–3 mg total). Lysate is diluted with 0.1 M Tris pH 8.0 to a final concentration of 1.3 M Gdn or urea. Proteome is digested with 1:100 dilution of trypsin overnight for 22-24 hr at RT. After digestion, peptides are acidified and cleaned up with SOLA SPE C18 desalting cartridges (Thermo). For single-time point SILAC samples, ~ 100 ug of eluted peptides were dried and analyzed separately by LC-MS/MS as unenriched “global proteomics.” Remainder of eluate was diluted 3-4 fold with water and lyophilized. ~1mg lyophilized peptides were resuspended in 80% ACN, 0.1% TFA and enriched on $FeCl_3$ charged NTA-agarose beads sitting atop a C18 matrix in a stage-tip platform. The iron binds charged phosphopeptides while uncharged peptides are passed through the beads and eluted from the C18 matrix. Phosphopeptides are washed, transeluted to the C18 matrix, washed again and eluted with 50% ACN, 0.1% TFA. Eluted phosphopeptides are dried in and stored at -80°C.

**Affinity Purification**

For each replicate, frozen cell pellets of 30E+6 AMO-1 cells expressing exogenous SRSF1-mCherry were gently lysed on ice with 200 µl hypotonic lysis buffer (20 mM Tris (pH 7.4@4C), 10mM KCl, 0.1mM EDTA, 0.5% NP-40 alternative, 1mM DTT, 1mM PMSF, 1x protease/phosphatase inhibitor cocktail (HALT), 300mM Sucrose, 0.03 U/mL aprotinin), underwent 3 X freeze-thaw cycles and clarified with 5 passes through an 18-gauge syringe needle. Lysate was centrifuged at 5,000 rcf, 4°C for 10 min and supernatant was reserved as cytoplasmic fraction. Wash pellet with 50 µl lysis buffer, spin again at 10,000 rcf, 4°C for 10 min, and combine supernatant with cytoplasmic fraction. Resuspend pellet in 60 µl nuclear extraction buffer (20mM HEPES (pH 7.9), 420 mM NaCl, 25% glycerol, 1mM EDTA, 1mM DTT, 1mM PMSF, 0.03 U/mL aprotinin, 1x protease/phosphatase inhibitor cocktail (HALT), 25 U

bioRxiv preprint doi: https://doi.org/10.1101/508549; this version posted December 30, 2018. The copyright holder for this preprint (which was not certified by peer review) is the author/funder. All rights reserved. No reuse allowed without permission.

Benzonase/mL), and clarified with 10 passes through 18-gauge syringe needle. Shake extract vigorously for 30 min at 4C, then centrifuge for 1 hr at 17,500 rcf, 4C, and collect supernatant as nuclear fraction. Both fractions were adjusted to 50 mM Tris pH 7.4, 150 mM NaCl, 1mM EDTA. Immunoprecipitation was carried out on cytoplasmic and nuclear fractions of cell lysate with M2 anti-FLAG magnetic beads (Sigma). Beads are equilibrated in binding buffer (50 mM Tris pH 7.4@4C, 150 mM NaCl, 1mM EDTA), and are incubated on a rotisserie with either cytoplasmic or nuclear fractions for 2 hr at 4C. Bound lysate beads were washed once with wash buffer (50 mM Tris pH 7.4@4C, 15 mM NaCl, 1 mM EDTA, 0.05% NP-40), once with binding buffer, then twice with FLAG rinse buffer (20 mM Tris pH 8.0, 2 mM $CaCl_2$). Protein bound beads are denatured and cystines are reduced and alkylated with 6 M Gdn, 40 mM 2-CAA, 5 mM TCEP, 100 mM Tris pH 8.0 at RT for 1 hr, then at 70°C for 1 hr. The Gdn is diluted back 6-fold to <1 M Gdn, and SRSF1 interacting proteins are trypsinized on-bead with ~0.75 ug trypsin/ sample, ~ 20h at 37°C, and peptides were desalted with homemade C18 stagetips, eluted with 40% ACN, 0.1% FA, dried and stored at -80°C.

**LC-MS/MS operation**

~1 µg sample of enriched phosphopeptides, unenriched "global" peptides, and SRSF1-mCherry-NLS-$[FLAG]_3$ interacting proteins were analyzed by "shotgun-" LC-MS/MS on a Dionex Ultimate 3000 RSLCnano (with 15 cm Acclaim PEPMAP C18 (Thermo) reverse phase column) and Thermo Q-Exactive plus mass spectometer. All samples except for AP-MS samples were analyzed by means of a 3h 15 min non-linear gradient from 2.4% ACN, 0.1% FA to 32% ACN, 0.1% FA, at 0.2 µL/min, 6 min linear gradient to 79% ACN, 0.1% FA at 0.5 µL/min, then wash with flowrate 0.5 µL/min at 79% ACN, 0.1% FA, for 7 min. AP-MS peptides were submitted to a 1h 23 min linear gradient from 2.4% ACN, 0.1% FA to 32% ACN, 0.1% FA, at 0.2 µL/min, 2 min linear gradient to 79% ACN, 0.1% FA, ramping flowrate from 0.3ul/min to 0.4 µL/min, then wash at 79% ACN, 0.1% FA, for 5 min ramping from 0.4 to 0.5 µL/min.

For timecourse, label free phosphoproteomics, MS1 scan range is from 350 to 1500 m/z, at resolution 70,000, AGC target 3E+6, and max. injection time(IT) 100 ms. Top 12 ions are selected for MS2 sequencing at resolution 17,500, AGC target 5E+4, max. IT 180 ms, normalized collision energy (NCE) 27 after each survey scan.

For SILAC phosphoproteomics, MS1 scan range is from 300 to 1750 m/z, at resolution 70,000, AGC target 3E+6, and max. injection time (IT) 20 ms. Top 12 ions are selected for MS2 sequencing at resolution 35,000, AGC target 1E+6, max. IT 108 ms, NCE 28 after each survey scan. For SILAC global proteomics and SRSF1 interacting AP-MS, MS1 scan range is from 350 to 1500 m/z, at resolution 70,000, AGC target 3E+6, and max. injection time(IT) 100 ms.

bioRxiv preprint doi: https://doi.org/10.1101/508549; this version posted December 30, 2018. The copyright holder for this preprint (which was not certified by peer review) is the author/funder. All rights reserved. No reuse allowed without permission.

Top 15 ions are selected for MS2 sequencing at resolution 17,500, AGC target 5E+4, max. IT 150 ms, normalized collision energy (NCE) 27 after each survey scan.
All MS2 isolation windows are 1.7 m/z with 20 s of dynamic exclusion.

**Proteomic data analysis and quantification**

Initial timecourse unlabeled phosphoproteomics data were processed together on Maxquant v1.5.1.2 with the following settings: Fixed modifications = "Carbamidomethyl (C), Variable modifications = "Oxidation (M)," "Acetyl (Protein N-term)," and "Phospho (STY)," PSM/Protein FDR = 0.01, min. peptide length = 7, matching time window for matching between runs = 2 min, with 20 min alignment time and all other default parameters. Phosphopeptides were searched against the human proteome, downloaded from Uniprot on 2014/12/3, with 89,706 entries. All SILAC samples were processed together on Maxquant v1.6.0.16 with the following settings: Fixed modifications = "Carbamidomethyl (C), Variable modifications = "Oxidation (M)," "Acetyl (Protein N-term)," PSM/Protein FDR = 0.01, min. peptide length = 6, max. peptide mass = 4600 Da, matching time window for matching between runs = 2 min, with 15 min alignment time and all other default parameters. For enriched phosphopeptides, variable modification includes "Phospho (STY)." Because RS domains contain many repeating arginines, max. missed cleavages = 9, Max. labeled AAs = 3. SILAC quantification for global proteomics at the protein level requires 1 minimum razor or unique peptide and uses all unmodified and "Oxidation (M)" and "Acetyl (Protein N-term)" modified peptides. Proteomics and phosphoproteomics were searched against the human proteome, downloaded from Uniprot on 2018/3/2, with 93,786 entries. AP-MS samples were also processed together on Maxquant v1.6.2.1with the following settings: Fixed modifications = "Carbamidomethyl (C), Variable modifications = "Oxidation (M)," "Acetyl (Protein N-term)," PSM/Protein FDR = 0.01, min. peptide length = 6, max. peptide mass = 4600 Da, matching time window for matching between runs = 2 min, with 20 min alignment time. Max. missed cleavages = 9. Proteins were searched against the human proteome, downloaded from Uniprot on 2017/11/15, with 71,544 entries. All relevant MaxQuant result files are deposited on
All proteomics (SILAC, AP-MS) quantifications, except for the timecourse study, were further evaluated in Perseus (v. 1.6.2.2), where potential contaminants, reverse dummy sequences, and proteins identified by site alone for protein level quantification are excluded. Gene ontology annotations were included to identify splicing related proteins. Two or three biological replicates were grouped and entries with less than 2 valid quantifications were filtered from the final analysis. For SILAC data, a one-sample T-test was applied to the log-2 transform of the normalized ratios (heavy:light) to determine the t-test difference and –log10 t-test p-value, shown in **Fig. 2A-D** and **S2A-D, and F**. For AP-MS data, two-sample T-test was applied to the log-2 transform of the median-normalized MaxQuant label-free quantification (LFQ) values of

bioRxiv preprint doi: https://doi.org/10.1101/508549; this version posted December 30, 2018. The copyright holder for this preprint (which was not certified by peer review) is the author/funder. All rights reserved. No reuse allowed without permission.

the SRSF1 pulldown versus the mCherry control pulldown samples. T-test differences and –log10 p-values are represented in **Fig. 4E and F**, **S5A, C, and E** volcano plots. List of all plotted proteins and phosphosites are included in **Supplemental Dataset 1**. The number of total entries (phosphosites, protein groups) and significantly changed/enriched entries ($p$<0.05, |t-test difference| >1), along with correlation statistics between replicates, are summarized in **Supplementary Dataset 1** and shown in **Fig. S3B**.

**Immunoblot**

Investigating stress response in **Fig. S3C**, AMO-1 cells were treated with DMSO, 10 nM Cfz, or 15 nM Cfz and MM.1S cells were treated with DMSO, 10 nM Cfz, 15 nM Cfz, 10 μM melphalan, or 15 μM melphalan for 24 hr. For DNA damage response markers in **Fig. S3D**, cells were either treated with DMSO, 15 nM Cfz, or 10 μM melphalan for 24 hr. To assay carfilzomib induced caspase cleavage of spliceosome components in **Fig. S3E**, MM.1S cells were treated with DMSO, 7.5 nM Cfz, or 10 nM Cfz, with or without pan-caspase inhibitor, z-Vad fmk for 18 hr. Cells were all treated with drugs at cell density of 1E+6 cells/mL and were harvested and centrifuged at 300x rcf, washed with 3-5 mL 1X PBS (UCSF), centrifuged again at 300x rcf, aspirated and flash frozen in 5E+6 cell aliquots in LN2 then stored in -80°C. For immunoblot determining expression level of exogenous SRSF1 in AMO-1 in **Fig. S4C**, SRSF1 expressing cells were treated with DMSO for 24 hr and harvested as above. Parental AMO-1, without exogenous SRSF1 was also included in immunoblot for comparison. For immunoblot examining baseline expression of SF3B1 in **Fig. 6D**, panel of MM cell lines were grown in culture and harvested without treatment.

For immunoblots, 5-10E+6 cells are thawed and lysed in 125-250 μl 1X RIPA buffer (Millipore) with 1X HALT protease/phosphatase inhibitor, incubated on ice for 15min, then sonicated with 3 bursts of 5 seconds ON, 10 seconds OFF, @ 20% amplitude with a tip sonicator (BRANSONIC), and keep chilled on ice. Protein concentration was quantified with either BCA protein assay kit (Pierce) or 660 nm protein assay reagent (Pierce), then combine ~300 μg lysate with 4X LDS loading dye. ~25-40 μg lysate is loaded per lane in SDS-PAGE gel (TGX, BioRad); the amount is kept consistent for each blot across all lanes. Proteins are electrophoresed for ~45 min at 170 V in Tris-Glycine buffer. Proteins are then transferred to PVDF blotting membrane (Millipore), pre-wet with MeOH, in Tris-glycine/20%MeOH transfer buffer at 38 V, 55 min. Afterwards, the membrane is rinsed with MeOH, stained with Ponceau-S for 5-20 min, shaking at room temperature, then imaged on a chemidoc gel imager (Bio-Rad) to account for total protein load. Plots are rinsed with TBS-Tween (TBS-T) several times, and blocked with 5% BSA in TBS-T for 30-60 min, shaking a room temperature. Primary antibodies are diluted in 5% BSA, TBS-T, according to manufacturer's specifications (1:1000) and blots are

bioRxiv preprint doi: https://doi.org/10.1101/508549; this version posted December 30, 2018. The copyright holder for this preprint (which was not certified by peer review) is the author/funder. All rights reserved. No reuse allowed without permission.

incubated in primary probe overnight at 4°C on a rocker, then washed the next day with a regimen of 4 X 5 min gently shaking with fresh TBS-T. Membranes are incubated in HRP-conjugated secondary antibody, diluted in 5%BSA and TBS-T for ~2 hr at room temperature on a rocker, washed again as before, then probes are visualized with either ECL Western blotting substrate or the SuperSignal West Femto ECL substrate for low abundance signals, such as phosphoprotein epitopes. Substrate luminescence on immunoblots were imaged on a chemidoc gel imager. Blots investigating phospho-specific probes were blotted with anti-phospho probes first, imaged, then stripped and re-probed with total protein probes, for a second round of probing and imaging.

For SRSF phosphorylation immunoblot in **Fig. S3F**, MM.1S were treated with DMSO or 10 nM Cfz while AMO-1 were treated with DMSO or 15 nM Cfz. Antibodies specific for phosphorylated RS domains of SRSF proteins are not commercially available, and phosphorylation was determined by gel migration. Cells were gently lysed in 100 mM Tris pH 8.5, 10 mM TCEP, 100 mM NaCl, 1% NP-40 alternative, 0.03 U/mL aprotinin and 1mM PMSF on ice for 30 min. Initial attempts showed no differential migration between treated and untreated samples. In order to identify differential migration of phosphorylated species, 20% of MM.1S DMSO sample was set aside and treated with calf intestinal phosphatase (NEB) for 1 hr at 37C in 1 X Cutsmart Buffer (NEB) to benchmark migration of dephosphorylated species. 1X HALT protease/phosphatase inhibitor was immediately added to all other samples and the remainder of the DMSO sample. The nucleus was separated from lysate by centrifugation and all samples were denatured with 4 M urea and 0.1% SDS. Immunoblot was prepared as above. Nuclear fractions were too viscous and ran with a smear, so were removed from final image in **Fig. S3F**.
See Key Resources Table for identifiers of antibodies used.

**RNA-seq library preparation**

RNA was extracted from frozen cell pellets with RNeasy Mini-prep kit (Qiagen). For timecourse experiments, cDNA library of expression transcripts was carried out with RNA Hyper Prep kit with RiboErase (Kapa) to enhance transcript reads above ribosomal reads, while single timepoint experiments assessing splicing required mRNA enrichment with magnetic mRNA Isolation kit poly-dT beads (NEB), then cDNA construction with RNA Hyper Prep kit (Kapa). Drug treated cells for RNA-seq were split from the same harvested cells that were used for phosphoproteomic studies. Cells were lysed on ice and genomic DNA was homogenized mechanically using a 18 gauge needle and syringe. For single-timepoint experiments Isolated total RNA was cleaned and concentrated with RNA clean & concentrator (Zymo). mRNA isolation begins with 3 ug total RNA resuspended in lysis/binding buffer, denatured at 65°C for 2 min and treated with SUPERasein, then bound to equilibrated poly-dT magnetic beads,

bioRxiv preprint doi: https://doi.org/10.1101/508549; this version posted December 30, 2018. The copyright holder for this preprint (which was not certified by peer review) is the author/funder. All rights reserved. No reuse allowed without permission.

incubated for 10 min, then subjected to a series of washes, according to manufacturer's protocol and eluted with 20 µµµRNAse-free water at 80°C for 2-3 min. cDNA library of 200-300 bp fragments was constructed with Illumina platform TruSeq indexed adapters using Hyper Prep RNAseq Illumina kit (Kapa), starting with at least 50 ng isolated mRNA. cDNA library between 200-400 bp were isolated by TBE-Urea PAGE (stained with SYBR Gold stain, imaged on Bio-Rad Chemidoc gel imager) and extracted from the gel by manual excision of bands. The gel pieces are blended by centrifuging through a needle prick hole at the bottom of an eppendorf into a collection tube at maximum speed for 3 min, then heated at 70°C for 10 min in 500 µl 10 mM Tris, pH 8.0 (with occasional vortexing). cDNA diffuses out of the gel matrix and separated from gel particles by spinning through Spin-X concentrator (Corning). cDNA is precipitated with 145 mM NaCl, 15ug/mL glycogen (Thermo), 58% isopropanol, incubated in -20°C overnight and centrifuged at 4°C for 45 min. The solution is removed and the precipitated white pellet is gently washed with 900 µl 80% ethanol, centrifuged at maximum speed for 5 min at 4°C. The ethanol is removed and the pellet is dried at room temperature for 10 min, then reconstituted in 5-10 µl 10mM Tris pH 8.0. RNA and DNA quantified at all steps by Nanodrop (Thermo Scientific) cDNA library size and quality were evaluated on a Bioanalyzer 2100 (Agilent) with High Sensitivity DNA Kit (Agilent), before being submitted for next generation sequencing on a HiSeq4000 (Illumina) at the UCSF Center for Advanced Technlogies laboratory.

**RNA-seq data analysis**

Four libraries from timecourse study were aligned with Bowtie v0.12.8 allowing for up to two mismatches. Aligned rRNA and tRNA reads were discarded. Remaining transcripts were aligned to known canonical transcriptsto human genome draft GRCh37/hg19. All other libraries were aligned with HISAT (v2.1.0). The mapped reads were converted from sequence alignment map format to binary alignment map format using Samtools (v1.3.1 for timecourse samples and v0.1.19 for all others). Transcriptome assembled and abundance quantified for four libraries from timecourse study by in-house C++ scripts, which assign and count unique reads mapping to canonical hg19 transcripts. Only uniquely mapping reads were used for analysis in **Fig. 1B**. All other binary alignment mapped reads were quantified for gene-level expression with HTSeq (v0.7.2). Differential gene expression analysis for single timepoint response study was performed in R with DESeq2. Differential gene expression is shown for MM.1S 18 nM Cfz vs. MM.1S DMSO condition in **Fig. S2E** and all differential expression lists are deposited in Gene Expression Omnibus (GEO, accession: *pending*). Please refer to Key Resources Table for software details.

**JuncBASE alternative splicing analysis**

bioRxiv preprint doi: https://doi.org/10.1101/508549; this version posted December 30, 2018. The copyright holder for this preprint (which was not certified by peer review) is the author/funder. All rights reserved. No reuse allowed without permission.

For all mapped reads, except for the timecourse study, alternative splicing events were quantified through JuncBASE v1.2-beta using default parameters. Intron-exon junction database was created from hg19 annotations. T-test was used to compare number of inclusion and exclusion reads and p-values were adjusted with Benjamini-Hochberg correction. For ΔPSI histograms in Fig. **3B and C, 4C and D, and 5A**, JuncBASE output included a small subset of alternative splice events with median PSI = 0.00 in both conditions or median PSI = 100.00 in both conditions, resulting in ΔPSI = 0.00. These were manually removed for all alternative splicing analyses. Histograms and splicing statistics were determined with statistical computing program R (v3.5.1) and a summary of the number of the number of total alternative splicing events, significant events (uncorrected $p < 0.05$ and $|\Delta PSI| > 10$), median and mode of total events ΔPSI, median and mode of significant events ΔPSI for all conditions are listed in **Table S3**. JuncBASE output files are deposited with RNA-seq data in GEO (accession: *pending review*)

**Gene Ontology enrichment analysis**

Gene Ontology (GO) enrichment analysis of upregulated phosphosites in **Fig. 2B and S1B**, and enriched SRSF1 interactors in **Fig. S5B,D, and F** were performed in STRING (v10.5, https://string-db.org/), searching against a background of all quantified protein entries that pass filtering criteria described above and listed in **Supplemental Dataset 1**. Enrichment analysis of all significantly alternative spliced genes presented in **Fig. 3D and S4D** (raw $p < 0.05$, all ΔPSI) and **Fig. 5C** (corrected $p < 0.05$) were performed using web-based enrichment analysis tool, Enrichr (Chen, et al. 2013, http://amp.pharm.mssm.edu/Enrichr/). Reported combined score is calculated by multiplying the natural log transform of the p-value with the Fisher's exact test of expected rank deviation (z-score). Functional GO analysis is limited to biological processes and compiled in **Supplementary Dataset 2**.

**Kinase Set enrichment analysis**

Entire phosphoproteomic results for MM.1S treated with 18 nM Cfz and MM.1S treated with 10 μM melphalan (see **Supplemental Dataset 1**) were submitted to kinase set enrichment analysis accessed through KSEAapp R package (https://github.com/casecpb/KSEAapp/). Gene name and phosphosite, along with fold change and associated T-test p-value statistic were input to generate kinase activity scores, listed in **Supplemental Dataset 2**. Bar graphs in **Figure 2F** show top ranked kinases, with at least 5 substrates (kinases with 4 or less were excluded from graph).

**Cell fixation and fluorescence imaging**

bioRxiv preprint doi: https://doi.org/10.1101/508549; this version posted December 30, 2018. The copyright holder for this preprint (which was not certified by peer review) is the author/funder. All rights reserved. No reuse allowed without permission.

5E+5 AMO-1cells expressing exogenous SRSF1WT-mCherry-NLS-3XFLAG and SRSF1mSD and SRSF1mSA mutants were harvested from cell culture, centrifuged at 300 rcf for 5 min. Media was aspirated and the cell pellet was washed once with 1X PBS, centrifuged again for 5 min at 300 rcf and aspirated. The cell pellet was then resuspended in ~200 µl 4% formaldehyde (Pierce) and incubated in the dark at room temperature for 1h 15 min to fix cells. After fixation, cells were centrifuged at 500 rcf for 5 min, and formaldehyde is removed gently. Cell pellet is resuspended in PBS and wash twice by centrifugation at 500 rcf for 5 min and aspiration of supernatant. After second wash, cells are resuspended at 5E+6 cells/mL in PBS and pipeted onto poly-L-lysine (Electron Microscopy Sciences) coated #1.5 coverglass (Fisher). A small drop of ProLong gold antifade with DAPI (Cell Signaling) is added to the cells on the coverslip and gently mixed by stirring with a pipet tip. The coverglass is mounted on glass slide and cured at room temperature, overnight.

Cells are imaged on a Zeiss Observer Z1 microscope using 63X plan-apochromat oil immersion objective (NA = 1.40). Filter sets for excitation and emission wavelengths for DAPI and mCherry imaging are ex = 335-383 nm, em = 420-470 nm and ex = 538-562 nm, em = 570-640 nm, respectively. Images in **Fig. 4B** were processed in ImageJ (v.1.48) and scale bar represents 10 µm.

**E7107 splicing assay**

RNA was extracted from AMO-1 and MM.1S with RNeasy Mini-prep kit and 500 ng total RNA was used to reverse transcribed polyA-tail mRNA to cDNA with Verso cDNA synthesis kit (Thermo). Splicing activity was determined by comparing fold-change abundance of mature, spliced form of FBXW5 and MBD4, or the unspliced pre-mRNA of cells between conditions by qPCR with SYBR Green supermix (Bio-Rad), in technical triplicate on a StepOne Real-Time PCR system (Applied Biosystems). ΔCt between splice targets and “House-keeping” gene PPIA normalized sample variation, and ΔΔCt reports the fold change difference between untreated (DMSO) and E7107 treated samples with 3 biological replicates in **Fig. S6B**.

**Xenograft mouse model and *in vivo* luminescence imaging**

1E+6 MM.1S-luc cells, stably expressing luciferase, were transplanted via tail vein injection into 12 NSG mice, individually. Tumor burden was assessed through weekly bioluminescent imaging in the UCSF preclinical therapeutic core on a Xenogen In Vivo Imaging System (IVIS), beginning 13 days after implantation, which is the same day as treatment initiation. Tumor implanted humanized mice were randomized and sorted into control arm and treatment arm, 6 mice/arm. Mice were treated for two weeks (five days on, two days off) with vehicle or 3 mg/kg E7107 as indicated. E7107 was formulated in vehicle (10% Ethanol, 5% Tween-80, QS with

bioRxiv preprint doi: https://doi.org/10.1101/508549; this version posted December 30, 2018. The copyright holder for this preprint (which was not certified by peer review) is the author/funder. All rights reserved. No reuse allowed without permission.

Saline) and administered by continuous subcutaneous infusion. Mice were kept and observed until survival endpoint; final timepoint was 41 days after start of dosing, or 54 days after MM.1S transplant.

**Patient bone marrow aspirate, CD138 labeling and flow cytometry analysis**

Isolated mononuclear cells from multiple myeloma patient bone marrow were adjusted to 2E+5 cells/well in a 96 well plate. Primary cells were stimulated with 50 ng/ml recombinant human IL-6 (ProsPec) for 17 hr before treatment with E7107 or DMSO for 24 hr. Cells were then stained with 10 µL Alexa-Fluor 647 mouse anti-human CD138 antibody (BD Pharmingen) or Alexa-Fluor 647 IgG κ isotype (BD Pharmingen) control and 2 µL SyTOX Green (Thermo) per 1 mL FACS buffer (D-PBS, 5% FBS). Resuspended cells are characterized with a CytoFLEX fluorescence cytometer (BD).

**Quantification and Statistical Analysis**

**Quantification of cell cytotoxicity**

Dose-response curves in **Fig. 6B-C, E, F** are plotted in GraphPad Prism 6 software.

**Quantification of bioluminescence imaging of *in vivo* mouse model**

Acquired luciferase intensities were quantified with Living Image Software (PerkinElmer) in units of radiance (photons/s/cm$^2$/sr), as shown in **Fig. 7B**. Kaplan-meier survival curves along with log-ranked test to determine significance in **Fig. 7C** were calculated in GraphPad Prism 6 software.

**Quantification of *ex vivo* CD138+ bone marrow plasma cells by flow cytometry**

Flow cytometry data was analyzed with FloJo v.8.8.6 to determine relative abundance of CD138+ cells, with respect to all cells counted. Fig. S7B shows an example dot plot of stained patient samples and geometric enclosure used to outline CD138+ cells in both DMSO (0 nM E7107) and 100 nM E7107 samples. Percent viability reported in Fig. 7D is normalized to amount in DMSO treated samples for each patient. Relative abundance of CD138- cells were counted by excluding CD138+ cells and then considering the relative abundance of live, non-SyTOX green stained cells with respect to all non-CD138+ cells.

**Analysis of Cancer dependency score (DepMap) for splicing proteins**

**Fig. 7E** displays a heatmap of the essentiality of 25 common essential splicing genes, which are evaluated for 26 cancer types from CRISPR-Cas9 knock-out screen from published dataset (AVANA 18Q4) comparing over 400 cancer cell lines. For each gene, each cancer type is ranked in terms of its dependence on the gene (1 = gene most essential to this cancer type).

bioRxiv preprint doi: https://doi.org/10.1101/508549; this version posted December 30, 2018. The copyright holder for this preprint (which was not certified by peer review) is the author/funder. All rights reserved. No reuse allowed without permission.

For example multiple myeloma ranks third of 26 cancer types for SF3B1 dependency in **Fig. S7C**. Dependency heatmaps in **Fig. 7E and S7D** are sorted based on the median ranking across the subset of genes.

**Analysis of CoMMpass dataset**

Progression-free survival (PFS) and overall survival (OS) data for newly-diagnosed MM patients enrolled in the CoMMpass study with genomic and transcriptomic data were used to plot survival curves with log-ranked test for significance in **Fig. S7G** in GraphPad Prism 6. Patients were either ranked according to SRSF1 expression or SF3B1 expression and the top and bottom quartiles of patients were compared.

**Statistical Analyses**

All data are presented as mean ± standard deviation, unless otherwise stated. Statistical significance in proteomics comparisons was determined by Student's T-test: One-sample T-test with null hypothesis that $\log_2$-transform of the normalized SILAC ratio = 0, or a two-sample T-test with null hypothesis that the difference in $\log_2$-transform of the intensities is equal to. A $p$ <0.05 is considered statistically significant and a $\log_2$ (ratio) > 1 is considered upregulated or enriched, and $\log_2$ (ratio) < -1 is considered downregulated or unenriched/excluded. For all Kaplan-Meier survival analysis, log-ranked test was used to determine statistical significance.

**Replication**

Timecourse phosphoproteomics were conducted with 2 technical replicates, while most single timepoint phospho- and global proteomics were conducted with 2 biological replicates, shown in **Fig. 2A, C, and D** and **Fig. S2A, C, and D**. MM.1S treated with 10 nM Cfz and MM.1S treated with 50 μM KH-CB19 proteomics were conducted with 3 biological replicates, shown in **Fig. 2B** and **Fig S2B, F**. Biological replicates come from independent experiments, carried out days or weeks apart. 3 biological replicates were used in the RNA-seq analysis. Except for the timecourse phosphoproteomics, all phospho-/ global proteomics and RNA-seq experiments were carried out with one technical replicate. All Cell-titer Glo measurements were performed in technical triplicate, except in quadruplicate as previously stated.

**Data and Software Availability**

**Data Resources**

The mass spectrometry proteomics data and MaxQuant analysis results have been deposited to the ProteomeXchange Consortium via the PRIDE (Vizcaíno et al., 2016) partner repository with the dataset identifier PXD012172. Datasets are private during review.

bioRxiv preprint doi: https://doi.org/10.1101/508549; this version posted December 30, 2018. The copyright holder for this preprint (which was not certified by peer review) is the author/funder. All rights reserved. No reuse allowed without permission.

Raw RNA-seq data, processed analysis files, and JuncBASE results may be downloaded from the Gene Expression Omnibus, GEO (https://www.ncbi.nlm.nih.gov/geo/) with the accession number: *pending review*.

**Additional Resources**

**Supplemental Table S1** lists oligo names and sequences used for SRFS1-lentiviral construction, qPCR splicing assay, as well as TruSeq indexed adapters for RNA-seq.

**Supplemental Table S2** lists SRSF1-lentiviral construct details. Although SRSF1-mCherry-$[FLAG]_3$ without NLS is not referred to in this manuscript, construct details are included.

**Supplemental Table S3** lists JuncBASE output summary statistics of total event ΔPSI distributions and subset significant event distributions for all conditions considered

**Supplemental Dataset 1** includes tabs listing phosphopeptide quantifications from timecourse study and output from Perseus (v. 1.6.2.2) comparative analysis (T-test p-value and $log_2$-difference) of phospho- and global proteomics from single timepoint studies, as well as output from Perseus analysis of AP-MS.

**Supplemental Dataset 2** includes tabs summarizing GO enrichment analysis for significant ($p$<0.05) alternative spliced genes identified by JuncBASE, for genes with upregulated phosphorylation and for genes enriched in SRSF1 AP-MS, with respect to mCherry control. The dataset also includes tabs summarizing KSEA kinase scores for all phosphopeptides quantified for MM.1S treated with 18 nM Cfz or 10 μM melphalan.

**Supplemental Dataset 3** includes table of variant alleles for the subset of splicing genes referenced in Seiler et al, 2018 from MM patient CoMMpass study with exome sequencing data.

**Materials**

| REAGENT or RESOURCE | SOURCE | IDENTIFIER |
|---|---|---|
| Antibodies | | |
| PERK | Cell Signaling Technology | Cat#5683P; RRID:AB_10841299 |
| BiP | Cell Signaling Technology | Cat#3183S; RRID:AB_10695864 |
| phospho-eIF2α | Cell Signaling Technology | Cat#3398P; RRID:AB_2096481 |
| eIF2α | Cell Signaling Technology | Cat#5324S; RRID:AB_10692650 |
| phospho-4EBP1 | Cell Signaling Technology | Cat#2855S; RRID:AB_560835 |
| 4EBP1 | Cell Signaling Technology | Cat#9644P; RRID:AB_2097841 |
| phospho-CHK1 | Cell Signaling Technology | Cat#2348P; RRID:AB_331212 |
| phospho-H2Ax | Cell Signaling Technology | Cat#9718P; RRID:AB_2118009 |
| anti-FLAG-M2 beads | Sigma-Aldrich | Cat#M8823; RRID:AB_2637089 |

bioRxiv preprint doi: https://doi.org/10.1101/508549; this version posted December 30, 2018. The copyright holder for this preprint (which was not certified by peer review) is the author/funder. All rights reserved. No reuse allowed without permission.

| | | |
|---|---|---|
| SF2/ASF (SRSF1), clone 96 | Santa Cruz BioTechnology | Cat#sc-33652; RRID:AB_628248 |
| SRp20 (SRSF3), G-8 | Santa Cruz BioTechnology | Cat#sc-398541 |
| SRp55 (SRSF6), 16H3 | Santa Cruz BioTechnology | Cat#sc-57954; RRID:AB_785899) |
| Caspase3 | Cell Signaling Technology | Cat#9664T; RRID:AB_2070042 |
| U2AF65 (U2AF2) | Abcam | Cat# ab37483; AB_883338 |
| SF3A1 | Abcam | Cat#ab128868 |
| SF3B1 (D7L5T) | Cell Signaling Technology | Cat#14434S |
| β-Actin-HRP (13E5) | Cell Signaling Technology | Cat#5125S; RRID:AB_1903890 |
| F(ab')2 Anti-Rabbit IgG(H+L), Mouse/Rat/Human ads-HRP | Southern Biotech | Cat#4052-05 |
| Anti-Mouse IgG(H+L), Human ads-HRP | Southern Biotech | Cat# 1031-05 |
| Alexa-Fluor 647 mouse IgG1, κ isotype control | BD Pharmingen | Cat# 557714; RRID:AB_396823 |
| Alexa-Fluor 647 mouse anti-human CD138 monoclonal antibody, clone MI15 | BD Pharmingen | 562097; RRID:AB_10895974 |
| **Bacterial and Virus Strains** | | |
| 5-alpha Competent *e. coli* | New England Biolabs | C2987H |
| **Biological Samples** | | |
| bone marrow aspirates from human MM patients | UCSF Hematologic Malignancy Tissue Bank | N/A |
| **Chemicals, Peptides, and Recombinant Proteins** | | |
| carfilzomib (PR-171) | Selleck Chemicals | S2853-50mg; CAS:868540-17-4 |
| melphalan | Sigma-Aldrich | M2011-100MG; CAS:148-82-3 |
| KH-CB19 (Clk-1 and -4) | Santa Cruz Biotechnology | sc-362756; CAS:1354037-26-5 |
| E7107 | H3 Biomedicine | CAS:630100-90-2 |
| Z-vad fmk | Selleck Chemical | S7023-5MG; CAS:187389-52-2 |
| Mini-Protean Any kD TGX stain-free gels | Bio-Rad | 456-8126 |
| Novex 15% TBE-Urea gel | Life Technologies | EC68852BOX |
| SYBR-safe stain | Life Technologies | S33102; CAS: 1030826-36-8 |
| SYBR-gold stain | Life Technologies | S-11494 |
| Ponceau-S | Fisher Bioreagent | BP10310; CAS:6226-79-5 |
| $FeCl_3$ | Sigma-Aldrich | F-7134; CAS:7705-08-0 |
| Ni-NTA agarose | Qiagen | 30210 |
| MicroSpin Columns, Peptide Protein C18 300Å | Nest Group Inc. | SEM SS18V.25 |
| SOLA C18 cartridge SPE | Thermo Fisher | 60109-001 |
| Bio-Spin Chromatography column | Bio-Rad | 7326008 |
| Spin-X concentrator | Corning Life Sciences | 8160 |
| glycogen, RNA grade | Thermo Scientific | R0551 |
| Calf intenstinal phosphatase (CIP) | NEB | M0290S |
| 100X Halt Protease and Phosphatase Inhibitor Cocktails | Pierce | 78442 |

bioRxiv preprint doi: https://doi.org/10.1101/508549; this version posted December 30, 2018. The copyright holder for this preprint (which was not certified by peer review) is the author/funder. All rights reserved. No reuse allowed without permission.

| | | |
|---|---|---|
| Acclaim PepMap RSLC C18, 2 µm, 100 Å, 75 µm i.d. × 15 cm, nanoViper | Thermo Scientific | 164534 |
| trifluoroacetic acid 99% (TFA) | Sigma Aldrich | T6508-10AMP; CAS: 76-05-1 |
| formic acid (FA) | Honeywell International | 94318-250ML-F; CAS: 64-18-6 |
| acetonitrile (ACN) CHROMASOLV Plus | Sigma-Aldrich | 34998-4L; CAS: 75-05-8 |
| Water (Optima LC/MS) | Fisher Scientific | W64 |
| Guanidine-hydrochloride (Gdn) | Chem Impex International | 00152-1KG; CAS: 50-01-1 |
| 2-chloroacetamide (2-CAA) | Sigma-Aldrich | 22790-250G-F; CAS: 79-07-2 |
| dithiothreitol (DTT) | Gold Biotechnology | DTT50; CAS: 27565-41-9 |
| tris(2-carboxyethyl)phosphine-hydrochloride (TCEP) | Pierce | 20491; CAS: 51805-45-9 |
| ProLong Gold Anti-fade reagent with DAPI | Cell Signaling Technologies | 8961S |
| *Bovine Serum Albumin (BSA), 99% min. Omnipur* | *Millipore Sigma* | *2930-100GM: CAS: 9048-46-8* |
| NuPage LDS Sample Buffer 4X | Thermo Scientific | NP0007 |
| 10X RIPA lysis buffer | EMD Millipore | 20-188 |
| ECL Western Blotting Substrate | Pierce | PI32106 |
| SuperSignal West Femto ECL Substrate | Pierce | PI34095 |
| Immobilon-FL-PVDF-Membrane, 0.45 µM pore size | EMD Millipore | IPFL00010 |
| Methanol ACS reagent >99.8% | Sigma-Aldrich | 179337-4L; CAS:67-56-1 |
| Methanol Chromasolv | Fisher Scientific | 6000964; CAS:67-56-1 |
| Isopropyl alcohol | Thermo Scientific | HC8001GAL; CAS:67-63-0 |
| 10X Tris/Glycine transfer buffer | Cell Signaling Technology | 12539S |
| 16% formaldehyde | Pierce Technologies | 28906 |
| 1X phosphate buffered saline (PBS) | UCSF Cell Culture Facility | CCFAL001 |
| Lenti-X concentrator | TakaraBio | 631231 |
| FuGene HD | Promega | E2311 |
| G418 Sulfate (Geneticin) | VWR | 970 3-058 |
| Pierce 660nm Protein Assay Reagent | Thermo Scientific | 22660 |
| SYTOX Green dead cell stain | Life Technologies | S34860 |
| Benzonase Nuclease | Sigma-Aldrich | E1014-5KU; CAS: 9025-65-4 |
| Aprotinin | Research Products International | A20550-0.001 |
| Phenylmethylsulfonyl fluoride (PMSF) | Research Products International | P20270-1.0; CAS: 329-98-6 |
| NP-40 alternative | EMD (Millipore) | 492016-100ML; CAS: 9016-45-9 |
| RPMI-1640 with 25 mM HEPES | UCSF cell culture facility; Gibco | CCFAE002; 22400105 |
| SILAC RPMI media | ThermoFisher | PI88421 |

bioRxiv preprint doi: https://doi.org/10.1101/508549; this version posted December 30, 2018. The copyright holder for this preprint (which was not certified by peer review) is the author/funder. All rights reserved. No reuse allowed without permission.

| | | |
|---|---|---|
| Opti-MEM I | Life Technologies | 31985-062 |
| Fetal Bovine Serum (FBS) | Atlanta Biologicals; | S11150 |
| Benchmark fetal bovine serum (FBS) | Gemini Bio-products | 100-106 |
| Dialyzed Fetal Bovine Serum | Thermo Fisher | PI88440 |
| 100X penicillin-streptomycin | UCSF Cell culture facility | CCFGK003 |
| IL-6 Human recombinant protein | ProSpec Bio | CYT-213 |
| #1.5 cover glass; borosilicate | Fisher Scientific | 12541B |
| EISCO Frosted Microscope Glass Slides | Fisher Scientific | S95933 |
| POLY-L-LYSINE 0.1% SOLUTION | Electron Microscopy Sciences | 19320-B; CAS: 25988-63-0 |
| Histopaque-1077 Hybri-Max | Sigma-Aldrich | H8889; CAS: |
| DPBS CMF (Dulbecco's Phosphate Buffered Saline, calcium-, magnesium-free) | UCSF cell culture facility | CCFAL003 |
| L-lysine monohydrochloride (Lys0) | Sigma-Aldrich | L8662-25G |
| L-arginine monohydrochloride (Arg0) | Sigma-Aldrich | A6969-25G |
| L-lysine:2HCl 13C6, 99%; 15N2 99% (Lys8) | Cambridge Isotope Laboratories | CNLM-291-H-1 |
| L-Arginine:HCL 13C6, 99%; 15N4 99% (Arg10) | Cambridge Isotope Laboratories | CNLM-539-H-1 |
| **Critical Commercial Assays** | | |
| Cell-titer glo | Promega | G7573 |
| Kapa (Roche) Hyper Prep RNAseq kit with RiboErase | Kapa | KK8560 |
| Kapa (Roche) Hyper Prep RNAseq Illumina kit | Kapa | KK8540 |
| Qiagen RNeasy purification kit | Qiagen | 74104 |
| Magnetic mRNA Isolation Kit | New England Biolabs | S1550S |
| QiaPrep Spin Miniprep Kit | Qiagen | 27104 |
| RNA Clean & Concentrator – 5 | Zymo Research | R1015 |
| RNA Clean & Concentrator – 25 | Zymo Research | R1017 |
| DNA Clean & Concentraor – 5 | Zymo Research | D4003 |
| DNA Clean & Concentraor – 25 | Zymo Research | D4005 |
| Pierce BCA Protein Assay Kit | Thermo Scientific | 23225 |
| Verso cDNA synthesis kit | Thermo Scientific | AB1453B |
| SsoAdvanced Universal SYBR Green Supermix | Bio-Rad | 1725272 |
| High Sensitivity DNA Kit (for Bioanalyzer 2100) | Agilent Technologies | 5067-4626 |
| **Deposited Data** | | |
| mass spectrometry raw data and MaxQuant analysis | PRIDE/Proteome eXchange | PXD012172 |
| RNA-seq raw data and processed analysis | Gene Expression Omnibus (GEO) | Pending |
| **Experimental Models: Cell Lines** | | |
| MM.1S | ATCC | CRL-2974 |
| AMO-1 | Dr. Cristoph Driessen | *gift* |
| AMO-1 Btz-resistant | Dr. Cristoph Driessen | *gift* |
| JJN3 mCherry | DSMZ repository | ACC 541 |
| INA6 | Dr. Renata Burger | *gift* |
| L363 | DSMZ repository | ACC 49 |

bioRxiv preprint doi: https://doi.org/10.1101/508549; this version posted December 30, 2018. The copyright holder for this preprint (which was not certified by peer review) is the author/funder. All rights reserved. No reuse allowed without permission.

| | | |
|---|---|---|
| RPMI8266 (8226?) | DSMZ repository | ACC 402 |
| KMS34 | JCRB Cell Bank | JCRB1195 |
| MM.1S mCherry F-Luc | McMillin et al, *Nature Medicine*, 2010 | UCSF Hematologic Malignancies Tissue Bank |
| Lenti-X 293T | Takara Bio | 632180 |
| **Experimental Models: Organisms/Strains** | | |
| NOD.Cg-*Prkdc*$^{scid}$ *Il2rg*$^{tm1Wjl}$/SzJ (NSG) mice | Jackson Laboratory | 005557 |
| **Oligonucleotides** | | |
| cloning primers (see Table S1) | Sigma-Aldrich | N/A |
| qPCR primers (see Table S1) | Sigma-Aldrich | N/A |
| gBlocks Gene Fragments (125-500 bp) (see Table S1) | IDT | N/A |
| RNA-seq Illumina TruSeq adaptors (see Table S1) | Sigma-Aldrich | N/A |
| **Recombinant DNA** | | |
| pLV-416G-fLuc/mCherry | McMillin et al, *Nature Medicine*, 2010 | UCSF Hematologic Malignancies Tissue Bank |
| pSpCas9(BB)-2A-GFP (PX458) | Ran et al. *Nature Protocols*, 2013 | Addgene Plasmid #48138 |
| Human ORFeome v8.1 | Yang et al. *Nature Methods*, 2011 | Center for Cancer Systems Biology |
| pCMV-dR8.91 | | Addgene Plasmid Plasmid #2221 |
| pMD2-G | pMD2.G was a gift from Didier Trono | Addgene Plasmid Plasmid #12259 |
| **Software and Algorithms** | | |
| Juncbase v1.2-beta | Brooks et al. *Genome Research*, 2011 | http://compbio.berkeley.edu/proj/juncbase/Home.html |
| KSEA v1.0 | Wiredja et al *Bioinformatics,* 2017 | https://casecpb.shinyapps.io/ksea/ |
| PERSEUS v1.6.2.2 | Tyanova et al. *Nature Methods*, 2016 | https://maxquant.org/perseus/ |
| MAXQUANT v1.6.0.16 | Tyanova et al. *Nature Protocols*, 2016 | https://maxquant.org/ |
| HISAT v2.1.0 | Kim et al. *Nature Methods*, 2015 | https://ccb.jhu.edu/software/hisat2/index.shtml |
| HTSeq v0.7.2 | Anders et al. *Bioinformatics* 2014 | https://htseq.readthedocs.io/en/release_0.10.0/overview.html |
| SamTools v0.1.19/v1.3.1 | Li et al. *Bioinformatics* 2009 | http://www.htslib.org/ |
| DESeq2 | Love et al. *Genome Biology,* 2014 | https://bioconductor.org/packages/release/bioc/html/DESeq2.html |
| Enrichr | Chen et al. *Bioinformatics* 2013 | http://amp.pharm.mssm.edu/Enrichr/) |
| STRING v 10.5 | Szklarczyk et al. *Nucl. Acids Res.* 2017 | http://string-db.org/ |
| SynergyFinder | | https://synergyfinder.fimm.fi/ |
| ImageJ v.1.48 | Rasband, 1997-2018 | https://imagej.nih.gov/ij |

bioRxiv preprint doi: https://doi.org/10.1101/508549; this version posted December 30, 2018. The copyright holder for this preprint (which was not certified by peer review) is the author/funder. All rights reserved. No reuse allowed without permission.

| | | |
|---|---|---|
| Living Image Software | Perkin Elmer | http://www.perkinelmer.com/category/in-vivo-imaging-software |
| FloJo v8.8.6 | FlowJo | https://www.flowjo.com/ |
| GraphPad Prism 6 v6.07 | GraphPad | www.graphpad.com |
| R Studio v1.0.153 | | https://www.rstudio.com/ |
| R v3.5.1 | | https://www.r-project.org/ |
| **Other** | | |

**Supplemental Table S1. Oligo sequences for cloning, qPCR, and RNA-seq cDNA library.** Oligo ID for CLONING.

**Supplemental Table S2 Genetic constructs.** Description of SRSF1 constructs.

**Supplemental Table S3 JuncBASE statistics.** Distribution of ΔPSI calculated in R. Statistics for individual event types and all event types are listed for each comparative condition.

**Supplemental Dataset 1: proteomics lists** .

**Supplemental Dataset 2: enrichment analysis.**

**Supplemental Dataset 3: splicing-genes and VAF**